FINITE ELEMENT CHARACTERIZATION OF SOFT TISSUE VISCOELASTIC PARAMETERS IN ACOUSTIC RADIATION FORCE IMAGING WITHIN THE REGION OF EXCITATION

by

XIAODONG ZHAO

A dissertation submitted to the

Graduate School-New Brunswick

Rutgers, The State University of New Jersey

In partial fulfillment of the requirements

For the degree of

Doctor of Philosophy

Graduate Program in Mechanical and Aerospace Engineering

Written under the direction of

Assimina A. Pelegri

And approved by

_____

_____

_____

_____

New Brunswick, New Jersey

October, 2015

ABSTRACT OF THE DISSERTATION

Finite Element Characterization of Soft Tissue Viscoelastic Parameters in Acoustic Radiation Force Imaging within the Region of Excitation

By XIAODONG ZHAO

Dissertation Director: Assimina A. Pelegri

Biomechanical imaging techniques based on acoustic radiation force (ARF) have been developed to characterize the viscoelasticity of soft tissue by measuring the motion induced with ARF noninvasively. The unknown stress distribution in the region of excitation (ROE) limits an accurate inverse characterization of soft tissue viscoelasticity. Thus, many assumptions have been made for both qualitative and quantitative ARF imaging within the ROE.

In this thesis, the finite element method is applied to study the dynamic behavior of soft tissue in ARF imaging within the ROE to investigate the assumptions that are made in these imaging methods and decide what factors affect the accuracy of these assumptions. To this end, the effects of global boundary conditions and local heterogeneity are investigated, and simplified quantitative inversion model is evaluated for their limitations in describing soft tissue dynamic behavior.

In order to improve quantitative estimation within the ROE, an inverse finite element (FE) characterization procedure based on a Bayesian formulation is presented, which takes full advantage of the prior information of the imaging system that are discarded in the simplified inversion models. The Bayesian approach formulates the known model parameters of the FE models as probability distributions, and aims to estimate a reasonable quantification of the probability distributions of soft tissue mechanical properties rather than best-fit values from an optimization procedure, which are not a practical or a comprehensive description of the estimation in the presence of measurement noise and model parameter uncertainty. To make the Bayesian approach computationally feasible, the Gaussian Process metamodeling method is applied as a statistical approximation of the complex FE model. A comprehensive numerical study in ARF induced creep imaging shows that the Bayesian approach with FE model improves the estimation results even in the presence of large uncertainty levels of the model parameters and provides a potential to improve the ROE-response-based imaging methods where the unknown stress limits an accurate inverse FE characterization.

Acknowledgements

First and foremost, I would like to express my heartfelt thanks to my advisor, Prof. Assimina A. Pelegri, for her invaluable suggestions and constantly generous support. Her encouragement and insight inspiration made this thesis possible. I would like to thank Dr. Alberto Cuitino and Dr. George Weng from Rutgers, The State University of New Jersey, and Dr. Bruce LaMattina from University of North Carolina at Charlotte for serving as my committee members, reviewing my thesis as well as giving helpful guidance.

I would like to express my gratitude to Dr. Baoxiang Shan, who helped me start the thesis research in this interesting field and provided me thoughtful guidance.

I also thank Dr. Yi Pan, Dr. Wensong Yang, Daniel Sullivan, Max Tenorio and Stephen Recchia for providing many helpful suggestions and technical assistance in my research.

I am also very grateful for the help of all members in our group: Colin Cui, Nico Cuitino, Abhimanyu Kamat, Chao Li, Michelle Lee and Mengdi Xing. They have been of great help and good friends.

Most importantly, I would like to extend my deepest gratitude to my wife and my parents for their love and encouragement. None of this would have been possible without their support.

Dedication

To my dear wife, Ning.

To my beloved parents, Mr. Yongqiang Zhao and Mrs. Yuhua Guo.

Table of Contents

List of Tables

List of Figures

Chapter 1: Introduction

1.1 Inverse Problem in Soft Tissue Viscoelasticity

Biomechanical imaging techniques have demonstrated great promise for soft tissue characterization and detection of tumors. These noninvasive imaging techniques are developed based on the fact that the mechanical properties of biological soft tissue are dependent on the pathological state of the tissue. [1–5] The general approach applies mechanical excitations to soft tissue, and then measures the induced responses of the tissue as metrics to reconstruct its mechanical properties. In cases where inclusions are considered, biomechanical imaging techniques can be used to estimate the elasticity and viscosity contrasts of the inclusion relative to the background tissue. [6–8] These imaging modalities successfully provide good results in tissue characterization and cancer detection. [3,4,9] Ophir et al. proposed the elastography method, which applies a static mechanical compressive loading on the tissue surface and measures the induced strain by a set of ultrasound A-lines. [2] For surface excitation, there are other methods that apply surface vibrations on tissues to generate dynamic vibrational displacement or shear wave inside them. [7,10,11] Based on these external excitation techniques, many global inverse methods have been proposed to reconstruct soft tissue mechanical properties. [11–14] However, global inverse methods are limited by high computational cost and non-unique solutions. These methods necessitate accurate information of the global boundary conditions, which can be quite complex and unattainable in practice [15–17]. In addition, the surface excitation methods become challenging when they are used to image deep

organs, as the induced surface motion cannot effectively penetrate into deep regions due to attenuation or the physical barrier. [16,18,19]

In order to promote stimulus effectiveness, internal excitation methods, which are based on generating a highly localized acoustic radiation force (ARF) to internally excite a targeted region in the soft tissue using focused ultrasound transducers, have been developed. [1,20–23] Compared to the global inverse scheme for modulus reconstruction, the localized ARF methods assume the excited soft tissues are in infinite and homogenous media, and no accurate description of the global model's complex boundary or local heterogeneity is required. However, simplifying assumptions made about infinite and homogenous media limit the accurate description of the soft tissue's viscoelasticity or its contrast. In addition, due to the unknown stress distribution in the region of excitation (ROE), an accurate finite element (FE) analysis of the inverse problem is challenging in ARF imaging.

1.2 Research Goals

This thesis has three goals.

First, the dynamic behavior of soft tissue within the ROE is studied in acoustic radiation force imaging. The effects of global boundary conditions and local heterogeneity are investigated. Simplified inversion model is evaluated for its limitations in describing soft tissue dynamic behaviors.

Second, an inverse FE procedure based on Bayesian approach is developed. The response of soft tissue to a step ARF is used to reconstruct the time constant which is a viscoelastic metric of soft tissue. Bayesian approach with FE model (BAFEM) is applied

to form a statistical inverse problem. The known model parameters of the FE models are represented as probability distributions, and the posterior distributions of soft tissue time constant are estimated.

Third, different sources of uncertainty are studied to evaluate the inverse procedure based on the BAFEM. This study demonstrates the effectiveness of the proposed method in the presence of uncertain model parameters.

1.3 Outline

Chapter 2 reviews the general theory of acoustic radiation force and the current research methods undertaken in acoustic radiation force imaging. Particularly, ARF imaging methods in the region of excitation that are most related to this thesis are discussed in detail.

In Chapter 3, the dynamic behavior of soft tissue in the region of excitation (ROE) is studied with FE models. The effects of global boundary conditions and local heterogeneity are investigated under different configurations. For a quantitative simplified model, its performance is evaluated for both homogeneous and heterogeneous cases.

Chapter 4 demonstrates the formulation of the inverse FE procedure based on the Bayesian approach. The general Bayesian estimation of this problem is first introduced. To make the Bayesian approach computationally feasible, the Gaussian Process metamodeling method is applied as a statistical approximation of the complex FE model. The posterior distribution of the time constant of viscoelastic soft tissue is formulated with measurement noise and uncertainty model parameters in the end of this chapter.

In Chapter 5, the Bayesian approach with FE model that developed in Chapter 4 is applied to estimate the posterior distribution of the time constant. Different sources of uncertainty are considered in the inverse procedure, and their effects on the inverse estimation are quantified.

Chapter 6 provides a summary on the major findings and contributions of this thesis. It also includes suggestions on future research on this topic.

Chapter 2: Review of Acoustic Radiation Force Imaging

This chapter first introduces the general theory of acoustic radiation force. Then a review of the state of the art research undertaken on acoustic radiation force imaging is delivered. Particularly, quantitative imaging methods in the region of excitation that are most related to this thesis are discussed in detail, which demonstrates the significance of the problem this thesis solved.

2.1 Acoustic Radiation Force Imaging Theory

Acoustic radiation force (ARF) is a spatial-varying body force. The magnitude of the acoustic radiation force at a specific location is described by

$$f_o = \frac{2\alpha I}{c} \tag{2.1}$$

where f_o is the body force magnitude, α is the tissue's absorption coefficient, I is the intensity of the radiation force and c is the speed of sound in the tissue. [8,16,23] ARF can be generated by ultrasound transducer arrays or a high intensity focus ultrasound (HIFU) transducer. The schematic of biomechanical imaging with ARF generated by HIFU transducer is shown in Fig. 2.1. The diagnostic ultrasound transducer mounted in the center opening of the HIFU transducer is used to monitor the motion of the tissue in the focal zone. In a finite element analysis, the motion of the tissue is directly estimated from the FE simulation.

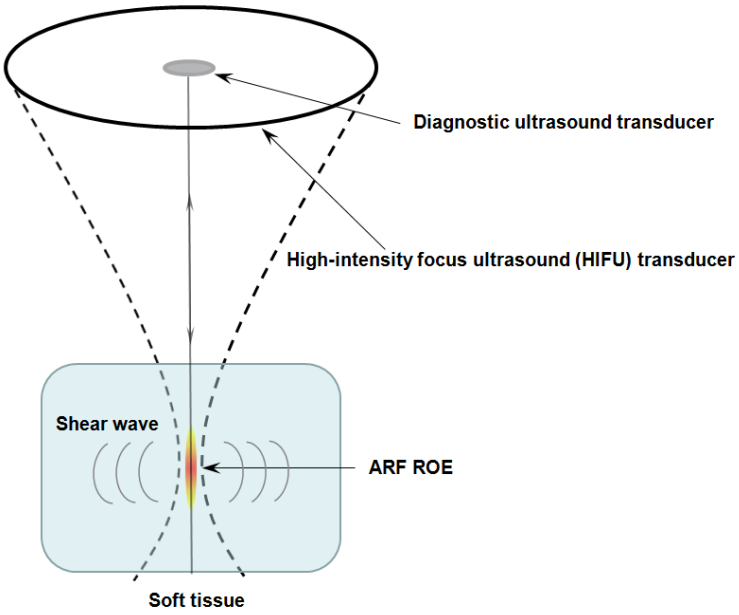

Figure 2.1. Schematic of biomechanical imaging with acoustic radiation force (ARF) generated by HIFU transducer. ARF is a spatial-varying body force as shown in the focal zone that is the region of excitation (ROE). The diagnostic ultrasound transducer mounted in the center opening of the HIFU transducer is used to monitor the motion of the tissue in ROE.

The analytical model for the displacement field induced by ARF is derived from the solution for a point load in an infinite isotropic homogeneous solid. Here, the point force is assumed to be applied at the origin along the *z*-axis. Then, the displacement field in the *z* direction is given by [24]

$$u_z = \frac{P(1+v)}{8\pi E(1-v)R}\left(\frac{z^2}{R^2} + (3-4v)\right) \tag{2.2}$$

where u_z is the displacement component in the *z* direction, P is the magnitude of the applied point force, v is Poisson's Ratio, E is Young's modulus, z is the axial distance with respect to the origin in the *z* direction, and R is the distance from the origin. The

ARF body force field can be decomposed into infinitesimal volume elements which approximate a series of point forces applied in the *z* direction. The displacement field induced by the ARF body force is obtained by superimposing the displacement generated from each point force. In ARF creep imaging, the displacement along the *z*-axis, i.e., the axis of symmetry of the body force field, is interested. Then, the displacement for any location on the *z*-axis is given by convolving the solution in Equation (2.2) with the spatial-varying body force field

$$u_z(z) = \frac{(1+v)}{8\pi E(1-v)} \int_{-\infty}^{\infty} \int_{0}^{2\pi} \int_{0}^{\infty} \left(\frac{(z-z_*)^2}{\left(\sqrt{(z-z_*)^2 + r^2}\right)^3} + \frac{3-4v}{\sqrt{(z-z_*)^2 + r^2}} \right) f(r, z_*)\, r dr d\theta dz_* \tag{2.3}$$

with *z* denoting the axial distance with respect to the origin in the *z* direction, *r* the radial distance from *z*-axis, and *f(r,z)* the body force density. It should be mentioned that Equation (2.3) is derived for an ARF body force with distribution *f(r,z)* in an infinite isotropic homogeneous medium.

2.2 Acoustic Radiation Force Imaging Methods

ARF imaging techniques use focused ultrasound transducers to generate a highly localized ARF to excite the region of interest inside the soft tissue. The mechanical properties (or their contrasts) of soft tissue can be reconstructed by measuring either the shear wave propagation away from the region of excitation (ROE) or the responses

within the ROE. [25–29] Many imaging techniques have been proposed based on different ARF excitations and measurement metrics.

2.2.1 Shear Wave Imaging

Shear wave imaging methods measure the shear wave propagation away from the ROE. They can estimate the soft tissue elasticity or viscoelasticity quantitatively, and have been studied by many research groups. These methods have been developed based on the Navier's equation described by [24,30]

$$\rho \frac{\partial^2 \boldsymbol{u}}{\partial t^2} = (\lambda + \mu)\nabla(\nabla \cdot \boldsymbol{u}) + \mu \nabla^2 \boldsymbol{u} + \rho \boldsymbol{b} \tag{2.4}$$

where ρ is the density, $\boldsymbol{u}$ is the displacement that depends on both space and time, and $\boldsymbol{b}$ is the body force. Lam é first parameter λ and shear modulus μ can be expressed in terms of Young's modulus E and Poisson's ratio ν as

$$\lambda = \frac{E\nu}{(1+\nu)(1-2\nu)}, \quad \mu = \frac{E}{2(1+\nu)} \tag{2.5}$$

In ARF imaging, the measured shear wave propagation is outside the ROE, where there is no ARF body force. Thus, the last term in the right hand side of Equation (2.4) can be eliminated. Then, the Helmholtz wave equation for shear wave propagation can be derived based on Equation (2.4): [20,31,32]

$$\rho \frac{\partial^2 u}{\partial t^2} = \mu \nabla^2 u \tag{2.6}$$

where ρ is the density, μ is the shear modulus, and u is the transverse displacement. Theoretically, for a near-incompressible (Poisson's ratio $v \cong 0.5$), isotropic, linear elastic solid, the speed of the shear wave can be described by [24]

$$c_s = \sqrt{\frac{E}{2(1+v)\rho}} \cong \sqrt{\frac{\mu}{\rho}} \tag{2.7}$$

where c_s is the shear wave speed.

It was first proposed by Sarvazyan et al. that ARF could induce shear waves remotely in soft tissue by focused ultrasound transducers, and the propagation of the induced shear waves could be monitored to estimate the elasticity of the tissue. [20] The basic theory of shear wave elasticity imaging (SWEI) with ARF was derived based on two ways of shear wave generation: periodic and pulsing ultrasonic modulation. Optical detection and magnetic resonance imaging method were applied to detect the induced shear waves in the experimental studies. These proof-of-concept experiments demonstrated the feasibility of SWEI with ARF.

ARF impulse induced shear waves have been applied in both *in vivo* and *ex vivo* experiments to image soft tissue shear modulus. [33–37] Direct inversion of the Helmholtz equation (Equation (2.6)) was first developed. However, the second order differentiation of displacement data is sensitive to noise, and the displacement data obtained with ultrasound generally have low signal-to-noise ratio (SNR). [35] Then, methods to estimate the shear wave speed were developed based on Equation (2.7), where the shear wave speed is estimated by measuring the time to peak displacement (TTP) at the lateral locations. [34,36,37]

Shear wave dispersion ultrasound vibrometry (SDUV) has been proposed to measure both tissue elasticity and viscosity. The theoretical basis for this method is described by [38–41]

$$c_s(\omega) = \sqrt{\frac{2(\mu^2 + (\omega\eta)^2)}{\rho(\mu + \sqrt{\mu^2 + (\omega\eta)^2})}} \tag{2.8}$$

where c_s is the shear wave propagation speed, ρ is the density, ω is the frequency of the shear wave, μ is the shear elasticity and η is the shear viscosity of the medium. Harmonic shear waves are produced with amplitude modulated ultrasound push beams. Different frequencies of the push beam generates shear wave with different ω, then the resulting shear wave speeds are different. The elasticity and viscosity of soft tissue can be solved by fitting Equation (2.8) with several excitation frequencies and the corresponding measured shear wave speeds.

There are other shear wave imaging methods developed with different ways of shear wave generation and measurement metrics. Supersonic shear imaging (SSI) applies a group of ARF excitations along the beam axis, which moves at a supersonic speed and generates a near plane shear wavefront that is monitored and used to imaging soft tissue elasticity. [31] Spatially modulated ultrasound radiation force (SMURF) uses two spatially separated ARF excitations and measures the displacement at a specified location to estimate the shear wave speed in the medium. [42]

2.2.2 Imaging within the Region of Excitation

As is discussed in last section, shear wave imaging methods have enjoyed great popularity, because they can image the soft tissue mechanical property quantitatively. A potential drawback to the shear wave imaging methods is that they measure the tissue responses outside the region of excitation where the displacement of tissue is much smaller and is sensitive to jitter due to the low SNR of the measurement, which can deteriorate in the presence of heterogeneity due to shear wave reflection. [25,26,43] Sometimes, the spatial resolution can be lower than a qualitative imaging method. [37] Alternatively, many ARF imaging methods based on the ROE measurements have been developed, which present their unique advantages: 1) displacement within the ROE is largest, and less radiation force is needed to excite the tissue which can reduce possible heating and damage due to ARF; 2) it is easier to measure the responses within the ROE than the shear wave propagation for experimental implementation. [20,26,43]

Acoustic radiation force impulse (ARFI) imaging applied a short acoustic radiation force impulse (the duration of which is generally less than 1ms) to excite the soft tissue. The resulting transient responses within the ROE are used to estimate the stiffness contrast. [22] These transient responses include the peak displacement, displacement at a given time, time of recovery from peak displacement, and time-to-peak displacement. [44,45] Many clinical applications of ARFI imaging have been develop for qualitative imaging of soft tissue. [46–49] Alternatively, harmonic motion imaging (HMI) employs a harmonic ARF and results in measurable dynamic responses, which are related to the local distribution of the tissue's mechanical properties. The measured amplitude of the induced harmonic displacement is considered to be inversely

proportional to the local tissue stiffness [5,16,23]. Consequently, the dynamic displacement amplitude is used as an indication of the underlying tissue stiffness. HMI elastograms exhibit good stiffness contrast and are used for monitoring soft tissue stiffness changes in thermal ablation. [50,51]

Both ARFI imaging and HMI are qualitative methods due to the unknown stress distribution in the ROE. The magnitude of the ARF is decided by the intensity of the acoustic radiation and the tissue attenuation as described in Equation (2.1). However, the acoustic radiation intensity can be changed when it travels through the media due to reflection and attenuation, which makes an accurate estimation of the intensity at a given special location challenging. In addition, the tissue attenuation value varies from patient to patient and is non-uniform. [26,27,52] Therefore, an accurate estimation of the ARF within the ROE is impossible, which makes that most of the ROE-based methods can only provide qualitative estimation. However, as is discussed in the beginning of this section, the advantages of imaging with ROE measurements make it desirable to develop quantitative imaging methods within the ROE.

Guzina et al. proposed a model-based quantitative viscoelastic characterization of thin tissues with ROE responses to a harmonic acoustic radiation force excitation. [25,53] In this method, the model local boundaries and ARF distribution were considered, and the inverse problem was solved analytically based on the frequency dependent responses of the thin tissues. However, this analytical method only validates for tissues with specific geometry and boundary conditions, i.e., thin tissues with under-damped dynamic responses.

A more general way to do quantitative imaging within the ROE is based on the temporal characteristics of the dynamic responses. Region of Excitation Time-to-Peak (ROE TTP) method has been developed to quantify tissue shear modulus within the ROE by measuring the time required for the displacement to reach its maximum under an impulsive excitation the duration of which is less than 1ms. [43,54] Since there is no analytical relationship between TTP and shear modulus for arbitrary ARF configuration. They proposed to use an empirical look-up table to build the relationship between TTP values and shear moduli. This method is developed to estimate only shear elasticity.

To estimate viscoelastic properties of soft tissue, the ARF induced creep imaging methods have been developed with step ARF excitation, and repeated ARF pulses with a high duty cycle are used to mimic the step forcing function. [21,36,55–57] This method was first proposed by Walker et al., and aims to quantitatively estimate a "force free" parameter, time constant, which is the ratio of shear viscosity to shear elasticity for a Voigt viscoelastic material. The time constant is called a "force free" parameter due to the fact that it is independent of the ARF magnitude, and it is assumed that it's decided by only the temporal creep displacement responses within the ROE. In order to estimate the absolute value of shear elasticity and viscosity, the ARF induced creep imaging needs to combine with other elasticity estimation methods. For example, Mauldin et al. applied shear wave elasticity imaging to estimate the tissue elasticity and ARF induced creep imaging to estimate the time constant. Then both the shear elasticity and viscosity can be estimated quantitatively. Without modeling the soft tissue and ARF, the time constant can be estimated with only the temporal creep response. This method did not consider the

interactions between tissue elements and the three-dimensional distribution of the ARF, which modeled the imaging system as a single degree-of-freedom (SDF) model. [29]

2.3 Summary

Acoustic radiation force imaging within the ROE offers both opportunities and challenges. It has advantages over shear wave imaging as is discussed in last section, while the unknown stress distribution within the ROE limits its quantitative imaging ability. In this thesis, the study will focus on the ARF imaging within the ROE.

Both the qualitative and quantitative imaging methods within the ROE are based on a series of assumptions: 1) the localized responses within the ROE are assumed to be independent of global boundary conditions; 2) the ROE is assumed to be in an homogeneous medium; and 3) single degree-of-freedom model is applied to describe the dynamic behavior of soft tissue that is actually a three-dimensional system. Sometimes, these assumptions may lead to large estimation error. It is necessary to investigate all these assumptions and decide what factors will affect the accuracy of these assumptions. What's more important, a more systematic and efficient procedure should be developed to implement quantitative imaging within the ROE in ARF imaging.

Chapter 3: Dynamic Behavior of Soft Tissue in Acoustic Radiation Force Imaging

A finite element method is employed to study the dynamic behavior of soft tissue within the ROE. The purpose of this study is to investigate these assumptions that are made in ARF imaging within the ROE and decide what factors will affect the accuracy of these assumptions. For the qualitative imaging, harmonic motion imaging (HMI) is investigated to study the effects of global boundary conditions on the localized ARF induced responses. In a heterogeneous medium, the contrast transfer efficiency of HMI is studied to justify the homogeneous assumption. For the quantitative imaging, the simplified single degree-of-freedom (SDF) model is evaluated for both homogeneous and heterogeneous cases.

3.1 Global Boundary Effects

The ARF generated by focused ultrasound is highly localized, and the response of the induced tissue is assumed to be only related to the local distribution of the mechanical properties, i.e., independent of global boundary conditions. However, simplifying assumptions made about the global boundary conditions limit the quantitative accuracy of the tissue's mechanical properties. In particular, when the dimensions of the soft tissue are comparable to the focal region size, similarly to characterization of skin tissue or skin lesions, the boundary effects can dominate the responses of the target tissue. [53] In this section, HMI is investigated to study the effects of global boundary conditions on the localized ARF induced responses. In HMI, the measured amplitude of the induced

harmonic displacement is inversely proportional to the local tissue stiffness. [23,58] Consequently, the dynamic displacement amplitude is used as an indication of the underlying tissue stiffness. Different boundary conditions and viscoelastic properties are applied to the FE model and the corresponding displacement amplitudes are studied. The effect of the model's global dimensions is also considered relative to its independence with respect to HMI excitation.

3.1.1 Model Formulation

The FE method has been widely used for the simulation of soft tissue dynamic behavior in ARF imaging. [14,45,50,59–62] The FE method has been applied to solve the governing partial differential equations (PDEs) of a system based on a weak form of the original PDEs, where the balance of linear momentum for a dynamic system can be express as [24,63]

$$\int_{\Omega} \sigma_{ij} \bar{\varepsilon}_{ij} d\Omega = \int_{\Omega} (b_i - \rho \ddot{u}_i) \bar{u}_i d\Omega + \int_{\Gamma} t_i \, \bar{u}_i d\Gamma \tag{3.1}$$

where σ_{ij} is the component of stress tensor, t_i is the component of the traction vector, Γ is the boundary of domain Ω, $\bar{u}_i$ is the component of virtual displacement, and $\bar{\varepsilon}_{ij}$ is the component of virtual strain.

In this study, the soft tissue in the FE model is assumed to be an isotropic, homogenous, linear viscoelastic, and near-incompressible medium. The objective is to investigate the effects of global boundary conditions on soft tissue HMI. Thus, the whole model is homogenous, and no hard inclusions representing tumors are included. The main components of the human breast are fat and glandular tissues, whose Young's moduli (E)

are in the range of 7.5-66 kPa. [64] For a near-incompressible medium, the Poisson's ratio of the model is set to 0.499. [6,45,65,66] As HMI applies dynamic excitation, the viscosity of soft tissues should be considered for the time-dependent responses in the FE model. For low frequency excitations (generally less than 100 Hz in HMI), the Kelvin-Voigt viscoelastic model is effective in modeling the time-dependent responses of soft tissues or tissue mimicking phantoms. [21,56,58,67,68] The general equation of motion for the FE discretization system is described by

$$\boldsymbol{M}\ddot{\boldsymbol{u}}(t) + \boldsymbol{D}\dot{\boldsymbol{u}}(t) + \boldsymbol{K}\boldsymbol{u}(t) = \boldsymbol{F}(t) \tag{3.2}$$

where $\boldsymbol{u}(t)$ is the global nodal displacement vector, $\boldsymbol{F}(t)$ is the global force vector, $\boldsymbol{M}$, $\boldsymbol{D}$ and $\boldsymbol{K}$ are the global mass, damping, and stiffness matrices, respectively. [63] For a Kelvin-Voigt viscoelastic model,

$$\boldsymbol{D} = \beta \boldsymbol{K} \tag{3.3}$$

where β is the viscous coefficient.

The effects of global boundary conditions in breast tissue characterization are investigated using an FE model. The dimensions of the FE model are 60 mm × 48 mm × 32 mm (width × depth × height). The mesh size is 4 mm and the 8-node linear brick C3D8 element is used with full integration over the volume of each element. The model is built with ABAQUS and is illustrated in Fig. 3.1. The bottom boundary of the model lies in the XY-plane when Z = 0, and is subjected to different constraint conditions. Human ribs are considered as the rigid structural support to breast tissue. [64] In our model, ribs are modeled as the encastre boundary, and the gaps between ribs are modeled

as the free part of the bottom boundary. The width of each rib is 12 mm, which is in the range of rib width of a normal adult. [69] The red shaded area in Fig. 3.1 is the encastre boundary on the bottom of the model.

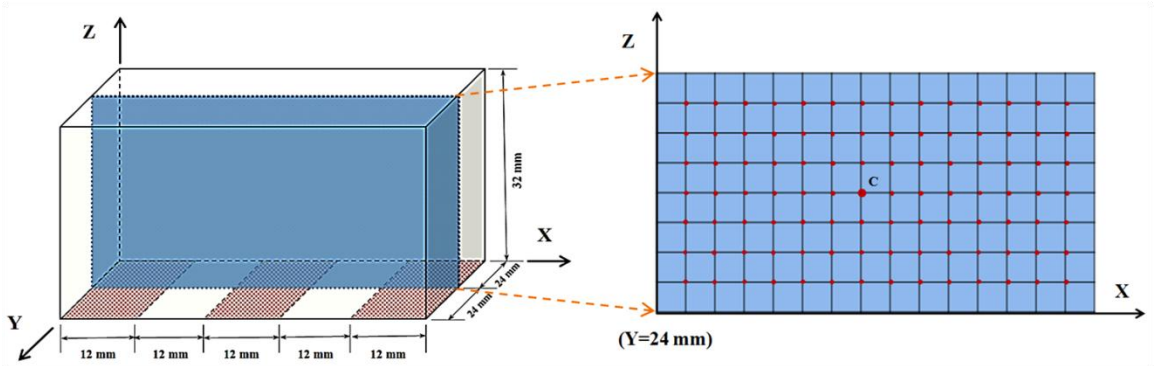

Figure 3.1. The rib-like bottom boundary (RBB) and the cross-section at Y = 24 mm. The red shaded area is the encastre boundary on the bottom of the model. A raster-scan technique is applied to the interior nodes of the cross-section. C is a node in the center area of the model.

A raster-scan technique is applied for the XZ cross section at *Y* = 24 mm as illustrated in Fig. 3.1. During the raster-scan process in HMI, the same harmonic force is applied at discretized locations inside the soft tissue. The displacement amplitude of each focal point is estimated based on the dynamic displacements measured by the diagnostic ultrasound transducer. Here, a harmonic force is sequentially applied at the interior nodes of the plane. When the force is applied on a node, the nodal displacement amplitude of this node is computed. This procedure is followed for every node until all the displacement data of the interior nodes are obtained.

The Explicit Dynamic Analysis (EDA) procedure is generally used for dynamic FE simulation. However, the EDA needs to update the equation of motion for every small

time increment, and a large number of increments (more than 10,000 for this problem) should be performed to acquire the displacement amplitudes indirectly. In order to improve the computational efficiency, Iorga et al. proposed a state-space model to analyze the dynamic responses of soft tissues in HMI. [59] The model order reduction techniques used in that study simplified the soft tissue model, but the procedure to formulate the state-space model is still complex. Hou et al. used the quasi-static deformation induced by the maximum HMI radiation force to approximate the dynamic displacement amplitude. [50] This approximation highly reduced the computational time and exhibited good accuracy for the pure elastic medium. However, for viscoelastic medium, the dynamic displacement amplitude of soft tissues is related to not only the HMI radiation force amplitude but also to its frequency, in which case the quasi-static deformation and the dynamic displacement amplitude can be quite different.

The Direct-solution Steady-state Dynamic Analysis (DSDA) is used to compute the dynamic response of soft tissues. DSDA is a linear perturbation procedure in ABAQUS, and is used for steady-state dynamic response analysis of a system to harmonic excitation as is formulated in Equation (3.4). [70]

$$\begin{bmatrix} \boldsymbol{K}-\Omega^2\boldsymbol{M} & -\Omega\boldsymbol{D} \\ -\Omega\boldsymbol{D} & -\boldsymbol{K}+\Omega^2\boldsymbol{M} \end{bmatrix} \begin{bmatrix} \mathrm{Re}(\boldsymbol{u}) \\ \mathrm{Im}(\boldsymbol{u}) \end{bmatrix} = \begin{bmatrix} \mathrm{Re}(\boldsymbol{F}) \\ -\mathrm{Im}(\boldsymbol{F}) \end{bmatrix} \tag{3.4}$$

where Ω is the excitation frequency, and other quantities are the same definition as in Equation (3.2) ($\boldsymbol{u}$ and $\boldsymbol{F}$ have complex components here).

This method can directly provide the steady-state nodal displacement amplitudes of the model to different excitation frequencies and it takes about 5% of the

computational time of EDA. The EDA procedure illustrated that the dynamic response of the viscoelastic soft tissue in HMI quickly converges to its steady state. Thus, the steady state response of the tissue is detected as the displacement amplitude, and DSDA is suitable for this study.

3.1.2 Model Validation

The finite element (FE) model and the analytical procedure are validated by comparing the simulation results between DSDA and EDA. The simulation parameters used are from literature reported experimental and simulation data on soft tissues. [58,59,71] The Young's modulus of the model E is 20 kPa, and the viscous coefficient considered is $\beta = 0.0001$s. The amplitude of the harmonic force is 0.0022 N with frequencies of excitation f = 50 Hz and 75 Hz, respectively. The force is applied in the Z-direction at node C, which is a node in the center area of the model as is shown in Fig. 3.1. EDA simulation results indicate that the transient response of the system will decay quickly for both f = 50 Hz and 75 Hz and their responses reach steady state in the first two periods, see Fig. 3.2. This confirms that DSDA procedure is suitable for this study. The estimated displacement amplitudes for f = 50 Hz and 75Hz are 25.23 μm and 30.86 μm, respectively. For the same configuration with DSDA, the computed displacement amplitudes for f = 50 Hz and 75 Hz are 25.25 μm and 30.59 μm, respectively, indicating good agreement between the two analytical procedures.

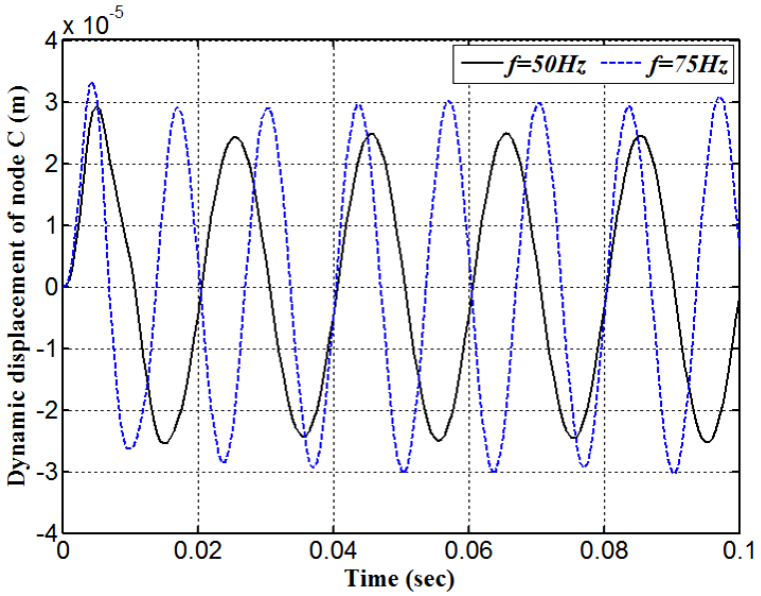

Figure 3.2. Dynamic response of node C simulated with Explicit Dynamic Analysis (EDA). The frequencies of the applied harmonic force are f = 50 Hz (—) and 75 Hz (--), respectively. The viscous efficient β is 0.0001s.

The FE analytical results were also validated using experimental data of gelatin phantoms performed by Maleke et al. (2005) for different kinds of materials with E=20, 30, 40, 50 and 60 kPa, respectively. Shan et al. calculated the values of the amplitude of the harmonic force and the viscous coefficients used in the experiments. [16,58] The calculated displacement amplitudes by DSDA for these five kinds of materials are all in the range of the estimated displacement amplitude from experiments as illustrated in Table 3.1.

Table 3.1. Comparison between simulation results of DSDA and experimental data on gelatine phantoms [71]

Young's modulus (kPa)	Estimated displacement amplitude from experiments (μm)	Estimated phase shift from experiments (°)	Calculated displacement amplitude by DSDA (μm)	Calculated phase shift by DSDA (°)
20	10.69±0.43	62	10.97	67
30	10.21±0.63	50	10.17	55
40	9.62±1.41	44	8.58	48
50	6.97±0.30	44	6.85	47
60	5.41±1.78	36	6.51	39

Harmonic force frequency f = 50 Hz, amplitude F = 0.0022 N. [16,58]

3.1.3 Effects of Global Boundary

In order to investigate the effects of global boundary conditions on the dynamic responses of soft tissues in HMI, different boundary conditions and viscoelastic properties are applied to the model, and the corresponding raster-scan displacement amplitudes are studied. The boundary conditions used in our model are a rib-like bottom boundary (RBB) and a completely fixed bottom boundary (CFBB) of which the bottom border of the model is totally constrained. Fig. 3.3 illustrates the displacement amplitudes in a raster-scan simulation on the cross-section at Y = 24 mm portrayed in a colourmap. Displacement amplitudes between nodes are computed by linear interpolation. The frequency of the harmonic force, f = 50 Hz and 75 Hz are applied to the model respectively. Two values of Young's modulus are investigated, namely E = 20 kPa and 60 kPa. As seen, a pure elastic case ($\beta = 0$) of HMI is depicted in Fig. 3.3. Generally, for

nodes near the unconstrained boundary, the displacement amplitudes have large values; for nodes near the fixed boundary, the displacement amplitudes have small values. It is also noted that the displacement amplitude distribution patterns vary considerably for different Young's moduli and frequencies of the applied harmonic force. This can be explained by the presence of system resonance of the FE model, and it has been observed that there are several resonant frequencies near 50 Hz and 75 Hz for soft tissue models with simulation parameters in the same range. [58,59] In addition, both changes in Young's modulus and excitation location result in a shift of the resonance frequency. [66] For this pure elastic case, the resonance cannot be damped by viscosity; thus the displacement amplitude has high spatial variance and model dependence, and it is sensitive to excitation frequencies.

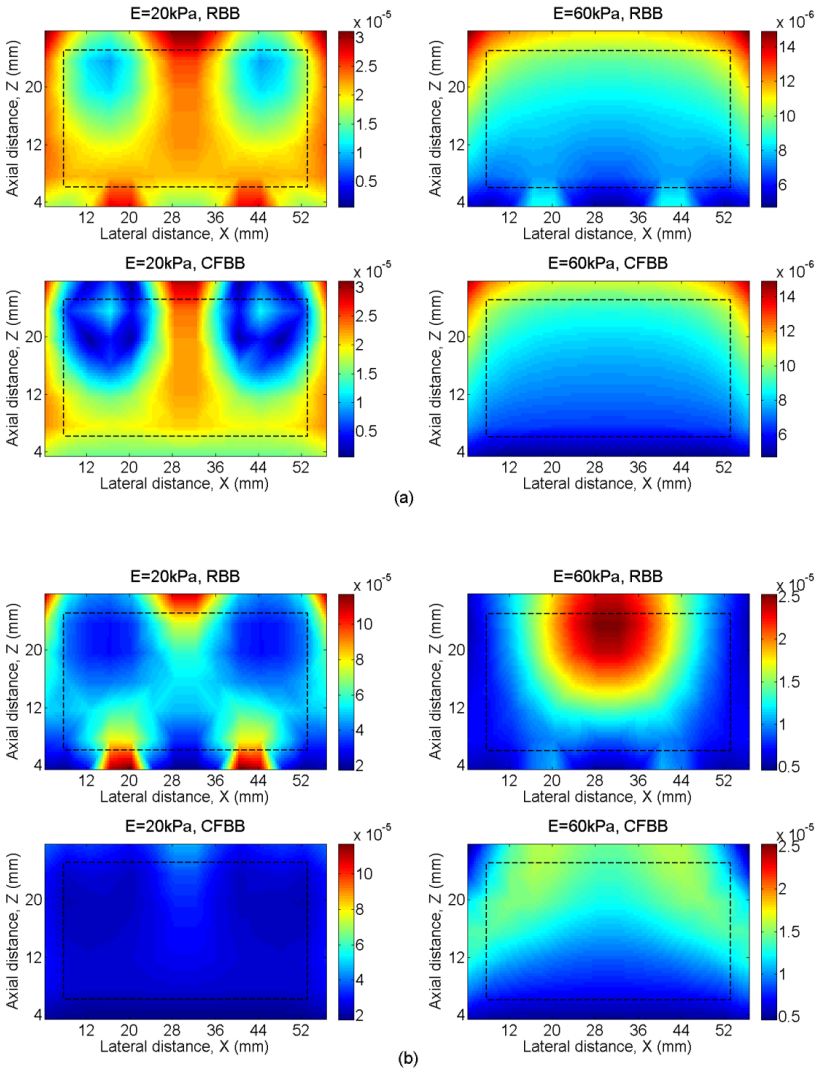

Figure 3.3. Mapping of displacement amplitudes (m) in a raster-scan simulation on the **c**ross-section at Y = 24 mm with viscous coefficient β = 0, i.e. the pure elastic case. Two kinds of bottom boundary conditions, a rib-like bottom boundary (RBB) and a completely fixed bottom boundary (CFBB) are investigated for Young's modulus E = 20 kPa and E = 60 kPa, respectively. The frequency of the harmonic force: (a) f = 50 Hz and (b) f = 75 Hz.

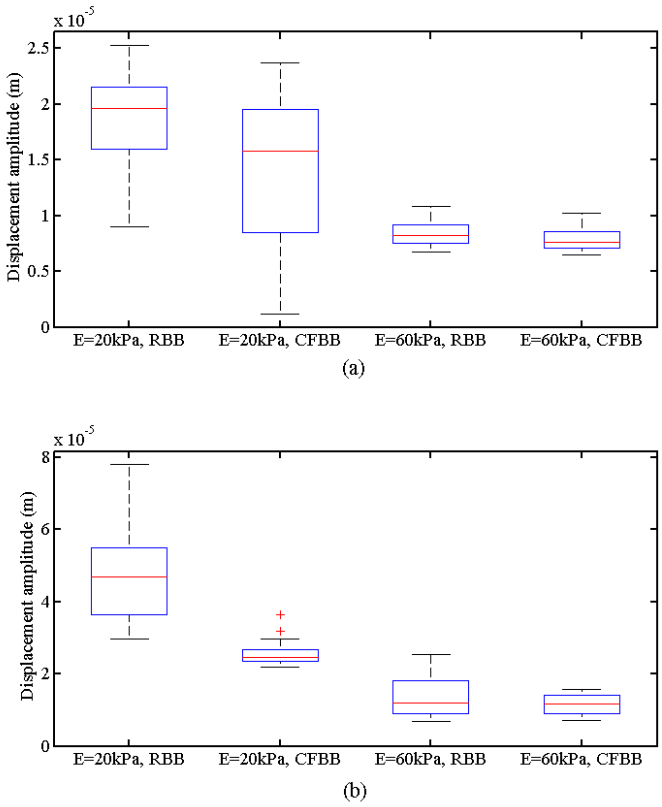

Figure 3.4. Distribution of the displacement amplitude data after discarding the nodes nearest to the boundary for simulation with viscous coefficient $\beta = 0$. Only the regions inside the dashed boxed in Fig. 3.3 are summarized here. This boxplot illustrates the effect of global boundary conditions on the dynamic responses of FE model of soft tissues in a pure elastic case. The frequency of the harmonic force: (a) f = 50 Hz and (b) f = 75 Hz.

In order to investigate the effect of global boundary condition on the interior nodes, the nodes nearest to the boundary are first discarded, and then the displacement amplitude data of the remaining nodes are analyzed. To illustrate that, the interior region is marked as the region inside the dashed box in Fig. 3.3. The distance from the surface of the model to the edge of the dashed box is 6 mm, and the dimension of the dashed box is 48 mm $\times$ 20 mm. A statistical analysis is performed for the interior region with Boxplot in Fig. 3.4. The top and bottom edges of the box are the 25th and 75th percentiles of the

amplitude data, the line near the middle of the box is the 50th percentile or the median. The length of the box is the interquartile range (IQR). The highest datum of the whisker represents the largest value that is within 1.5×IQR of the 75th percentiles, the lowest datum of the whisker represents the smallest value that is within 1.5×IQR of the 25th percentiles, and values not included between the whiskers are plotted as outliers with plus signs. [72] The boxplot can accurately describe the displacement amplitude data distribution. For each case, the displacement amplitudes of the interior nodes are not uniform and vary in a wide range, which means that these displacement amplitudes are related to the global locations of the excited nodes. Comparing the cases that have the same Young's modulus but different boundary conditions, it can be deducted that boundary conditions affect not only the response of nodes near the boundary, but also the response of the whole model.

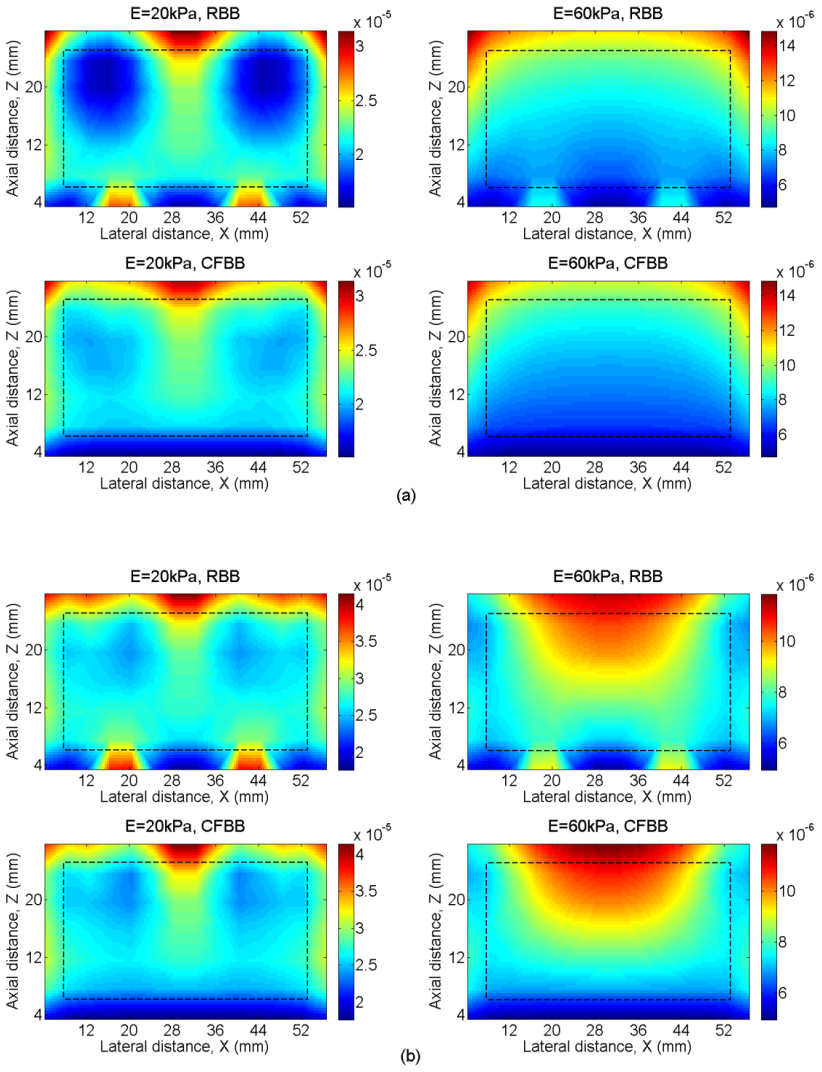

Figure 3.5. Mapping of displacement amplitudes (m) in a raster-scan simulation on the **c**ross-section at Y = 24 mm with viscous coefficient $\beta = 0.0001$s. Two kinds of bottom boundary conditions, RBB and CFBB, are investigated for Young's modulus E = 20 kPa and E = 60 kPa, respectively. The frequency of the harmonic force: (a) f = 50 Hz and (b) f = 75 Hz.

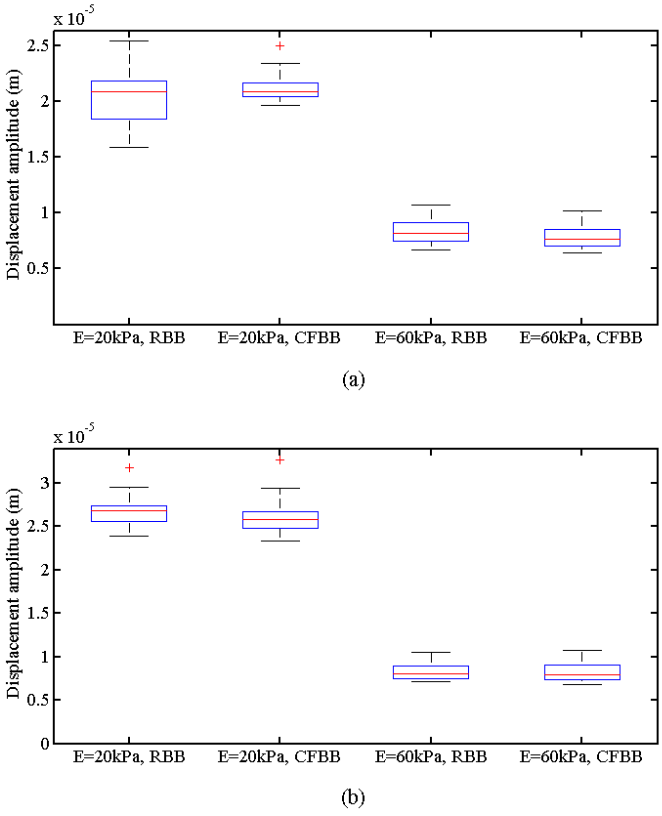

Figure 3.6. Distribution of the displacement amplitude data after discarding the nodes nearest to the boundary for simulation with viscous coefficient $\beta = 0.0001$s. Only the regions inside the dashed boxed in Fig. 3.5 are summarized here. The frequency of the harmonic force: (a) f = 50 Hz and (b) f = 75 Hz.

The responses of models with low viscosity are considered next. The viscous coefficient is $\beta = 0.0001$s. After adding the viscosity, the two boundary conditions, RBB and CFBB, give similar results for displacement amplitudes of the interior nodes, as depicted in Figs. 3.5 and 3.6. In addition, it is noted that the two excitation frequencies also give similar displacement amplitude distribution patterns, signifying that the effect of resonance has been attenuated by viscosity. However, the displacement amplitudes still vary a lot at different locations of the model, for example, the case of f = 75 Hz and E

= 60 kPa in which the displacement amplitudes decrease gradually from the free top surface to the fixed (or partly fixed) bottom boundary.

Subsequently, the viscous coefficient of the soft tissue is increased to $\beta = 0.001$s. As depicted in Fig. 3.7 and similarly to the case of viscous coefficient $\beta = 0.0001$s, displacement amplitudes of the interior nodes for both boundary conditions are nearly identical. Meanwhile, displacement amplitudes do not significantly change at different locations of the interior region. A statistical analysis is performed for the interior region with boxplot, Fig. 3.8. It is observed that the higher excitation frequency, f = 75 Hz, results in more uniform displacement amplitude data than f = 50 Hz does, which may be attributed to the fact that a higher frequency motion is damped more for the same viscosity and the effect of resonance related to the global boundary and location can be better attenuated for f = 75 Hz. For both frequencies, the displacement amplitude data vary in a small range for the interior region for the two Young's moduli and two kinds of boundary conditions. To some extent, in HMI, the dynamic responses of this region can be considered independent of position or global boundary conditions, and then subjected to localized analysis procedure without considering the possible complex global boundary conditions when analyzing the interior region.

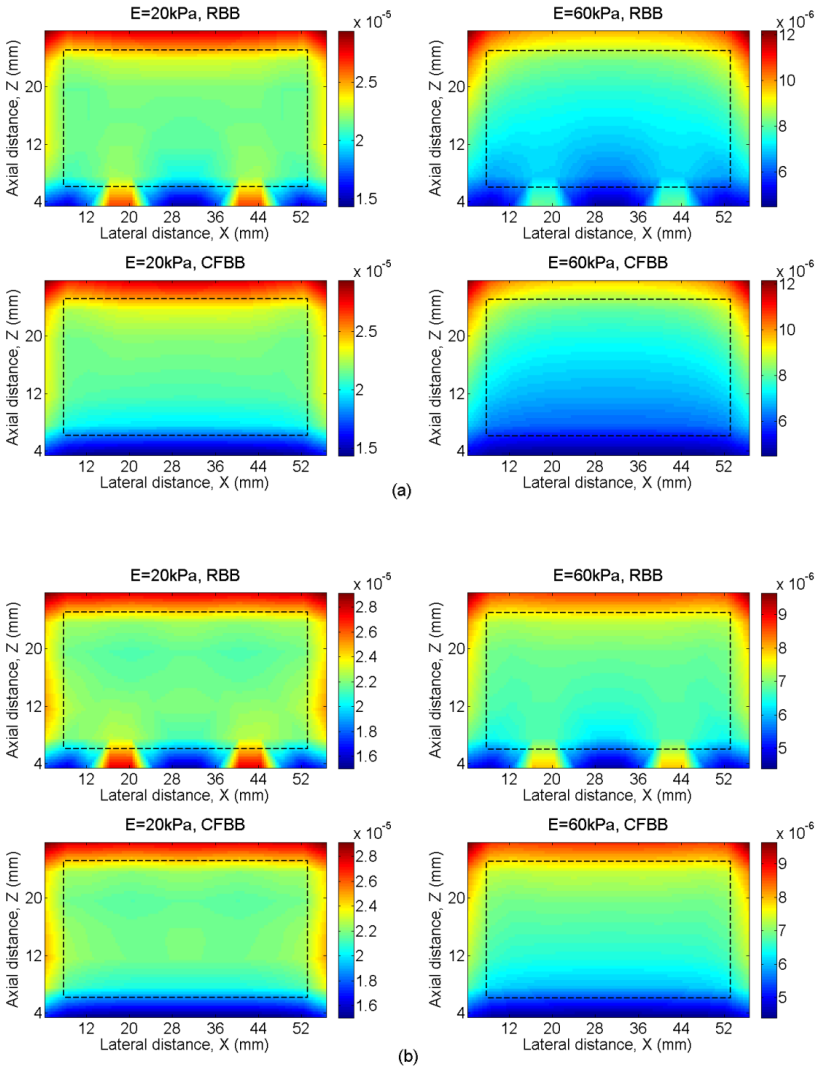

Figure 3.7. Mapping of displacement amplitudes (m) in a raster-scan simulation on the cross-section at Y = 24 mm with viscous coefficient $\beta = 0.001$s. Two kinds of bottom boundary conditions, RBB and CFBB, are investigated for Young's modulus E = 20 kPa and E = 60 kPa, respectively. The frequency of the harmonic force: (a) f = 50 Hz and (b) f = 75 Hz.

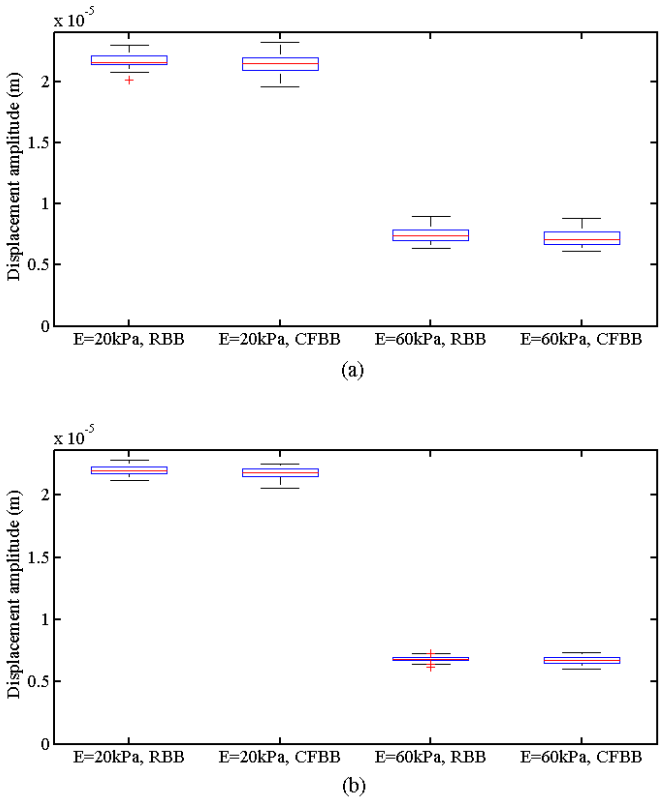

Figure 3.8. Distribution of the displacement amplitude data after discarding the nodes nearest to the boundary for simulation with viscous coefficient $\beta = 0.001$s. Only the regions inside the dashed boxes in Fig. 3.7 are summarized here. This boxplot shows the good independence of global boundary conditions of the dynamic responses of soft tissues in HMI when the viscous coefficients of the tissues are relatively high. The frequency of the harmonic force: (a) f = 50 Hz and (b) f = 75 Hz.

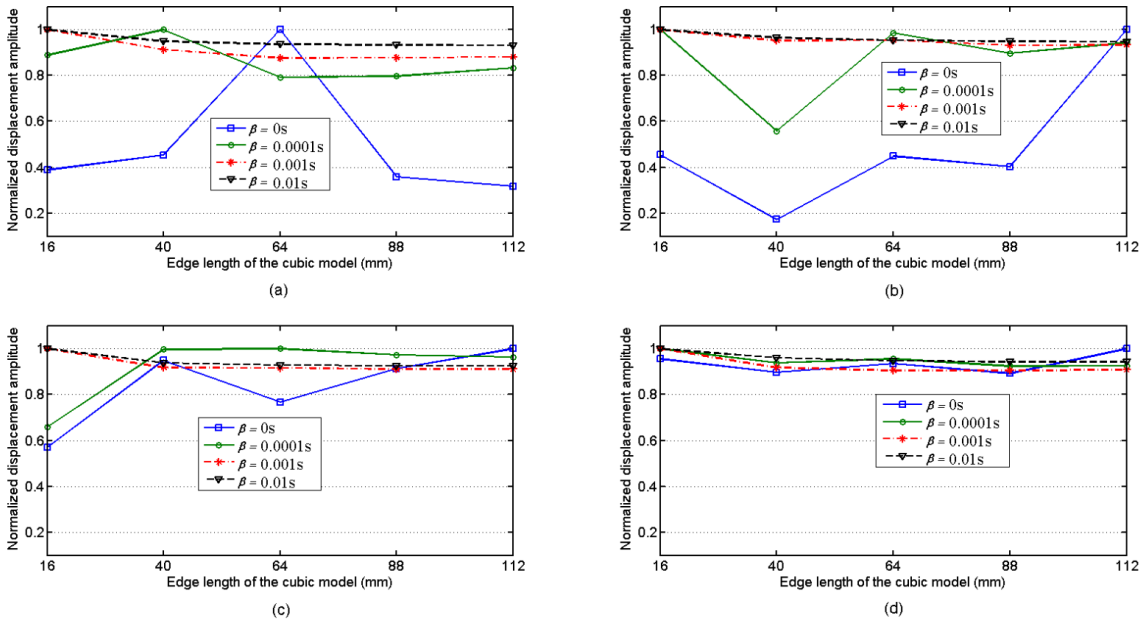

Figure 3.9. Displacement amplitudes of central node for cubic models with different dimensions and viscous coefficients. (a) E = 20 kPa and f = 50 Hz; (b) E = 60 kPa and f = 50 Hz; (c) E = 20 kPa and f = 75 Hz; (d) E = 60 kPa and f = 75 Hz.

Our results illustrate that the effects of global boundary conditions tend to vanish in the interior region of a model with high viscous coefficient in HMI analysis. Under the same excitation force, the dynamic responses of the interior regions should be approximately the same for different homogenous soft tissue models with the same viscoelasticity. In order to verify the above analysis, five cubic soft tissue models with different dimensions are studied. The edge lengths of the five cubic models are 16 mm, 40 mm, 64 mm, 88 mm, and 112 mm, respectively. The same excitation force is applied to the central node of each model. The viscous coefficients $\beta = 0$, 0.0001s, 0.001s and 0.01s are investigated. For each viscous coefficient, the displacement amplitudes of the central nodes are obtained for all five models, and then normalized by the maximum of the five displacement amplitudes. The results are plotted in Fig. 3.9. For $\beta = 0$, the pure

elastic case, the displacement amplitudes of the central nodes vary notably for models with different dimensions. For $\beta = 0.0001$s, the data only vary in a small range. For $\beta = 0.001$s and $\beta = 0.01$s, all five models give approximately the same displacement amplitude for each case, indicating independence of the dynamic responses of the central nodes from the dimension of the models. In particular, for the 16 mm × 16 mm × 16 mm cubic model, the dynamic responses of its central node are incommensurable with the other larger models for all four viscous coefficient values. That means the localized dynamic responses of soft tissues are not independent of the global boundary conditions as the dimension of the model becomes small. When the dimensions of soft tissue become comparable to the focal region size, the global boundary effects may even dominate the responses of the target tissue.

3.1.4 Summary

In HMI, a qualitative imaging within the ROE, the effects of global boundary conditions on the localized ARF induced responses are studied with FE method. The FE model simulated two different boundary conditions, rib-like bottom boundary and completely fixed bottom boundary, and three different viscous coefficients $\beta = 0$, 0.0001s, and 0.001s. In particular, for regions near the boundary, the dynamic responses of soft tissues are highly dependent on the boundary conditions. In the case of low viscous or pure elastic model, boundary conditions affect not only the responses of region near the boundary, but also the responses of the whole model. In the case of model with high viscous coefficient, HMI provides consistent displacement amplitude data for interior region, which can be considered independent of position or global boundary conditions,

and thus justifiably subjected to localized analysis. Study on the effects of global dimensions confirms that the dynamic responses of the interior region are independent of the dimensions of the model in the case of high viscous coefficient.

3.2 Contrast Transfer Efficiency

In HMI, localized analysis does not require an accurate description of the complex boundary of the global model, which highly simplifies the estimation of tissue stiffness. In homogenous media, the measured amplitude of the induced harmonic displacement and the local tissue stiffness are shown to be approximately in inverse proportion. However, in heterogeneous media, the response of the focal area can be affected by the local heterogeneity and the inverse proportion relation between displacement amplitude and tissue stiffness becomes invalid. In this case, the observed stiffness contrast is defined as the inverse of inclusion-to-background displacement amplitude contrast. Then, this contrast is compared with the true stiffness contrast, which yields the contrast-transfer efficiency (CTE). Ponnekanti et al. and Kallel et al. used CTE to investigate the limitations of elasticity contrast visualization in static external excitation case. [73,74] Both their finite element simulations and analytical derivation results illustrated that elastograms are less efficient in depicting the elastic contrast of soft inclusion embedded in hard background than that of hard inclusion embedded in soft background. Maleke et al. showed that HMI is a reliable stiffness-mapping technique for tumor detection based on the CTE analysis of HMI for elastic materials. [61] However, soft tissues are viscoelastic materials. The viscosity of soft tissues needs to be taken into consideration in

the CTE analysis of HMI. In addition, a wide range of inclusion to background stiffness contrast should be studied to show a more general contrast-transfer performance of HMI.

In this study, a finite element FE model is built, and the direct-solution steady-state dynamic analysis (DSDA) is used to compute the dynamic responses of soft tissues in the finite element simulation as is discussed in last section. Then, the CTE of HMI is investigated for different inclusion to background contrast ratios. The effects of excitation frequency and material viscosity on CTE are also studied in HMI.

3.2.1 Heterogeneous Finite Element Model

A 3D FE model was developed using ABAQUS and is illustrated in Fig. 3.10. The dimensions of the original model of the soft tissue are 48mm× 48mm × 48mm (width × length × height). The bottom boundary is fixed in all directions. There is a 4mm× 4mm × 4mm cubic inclusion in the center of the model. As the applied harmonic force is along the z-direction, symmetry about the x=0 and y=0 planes can be used to reduce the dimensions of the model. The 3D FE model employed the 8-node linear brick C3D8 element with full integration over the volume of each element. The FE model has totally 12,600 elements with the minimum mesh size 0.4mm. The region near the inclusion has higher-density mesh to ensure computational accuracy. A mesh convergence study was also performed to make sure the mesh of the model is fine enough. The harmonic force used in this study is a body force applied along the z-direction. The focal volume of the body force is 1mm× 1mm × 2mm (width × length × height). The magnitude of the body force does not affect the final computed contrast in this study; because linear viscoelastic

material properties are assigned to the model and all the displacement amplitudes are proportional to the body force magnitude.

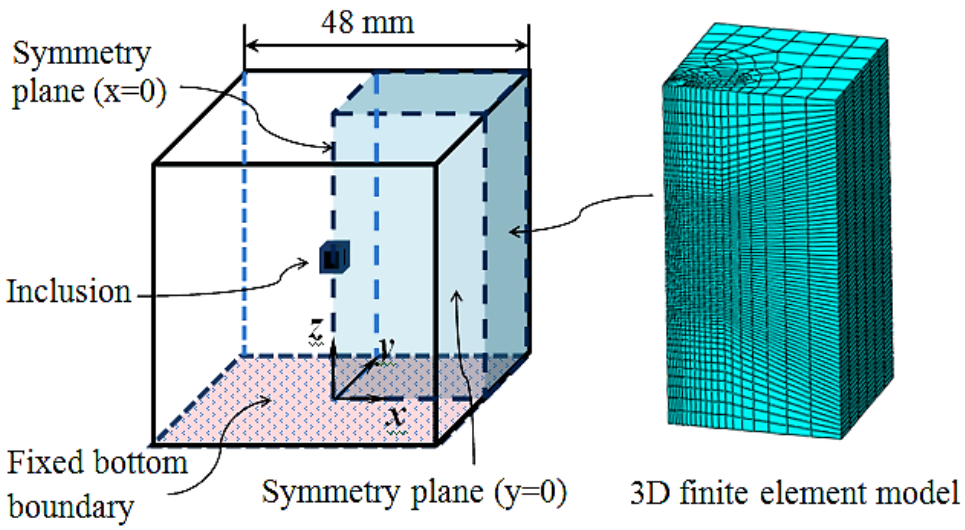

Figure 3.10. 3D soft tissue model and 3D finite element model. The dimensions of the soft tissue model are 48mm × 48mm × 48mm. The bottom boundary is fixed in all directions. There is a 4mm × 4mm × 4mm cubic inclusion in the center of the model. Symmetry about the x=0 and y=0 planes is used to reduce the dimension the finite element model. The dimension of the finite element model is 24mm × 24mm × 48mm.

3.2.2 Contrast-transfer Efficiency

The contrast-transfer efficiency (CTE) of HMI is defined as the ratio of the observed stiffness contrast to the true stiffness contrast. The observed stiffness contrast C_o is the inverse of inclusion-to-background displacement amplitude contrast. This contrast is obtained by averaging the displacement amplitude data inside the inclusion and in the background separately, calculating the ratio of the two averaged data (Equation (3.5)), and computing the inverse of this ratio. [61]

$$C_o = \frac{\overline{D}_{Background}}{\overline{D}_{Inclusion}} \tag{3.5}$$

The true stiffness contrast is the inclusion-to-background elastic contrast. Seven inclusion-to-background elastic contrasts were studied: 1:30, 1:10, 1:3, 1:1, 3:1, 10:1, and 30:1, from soft inclusion in hard background to hard inclusion in soft background. Then, the CTE in a logarithmic decibel scale is described as [61,73]

$$CTE(\text{dB}) = C_o(\text{dB}) - C_t(\text{dB}) \tag{3.6}$$

$$C_t = \frac{\mu_{inclusion}}{\mu_{background}} \tag{3.7}$$

where C_o is the observed stiffness contrast and C_t is the true stiffness contrast. The ideal performance of a biomechanical imaging method in terms of CTE is when the observed elasticity contrast equals the true elasticity contrast, i.e., $CTE(dB) = 0$.

3.2.3 Contrast-transfer Efficiency for Model with Inclusion

The DSDA procedure is first validated by the general explicit dynamic analysis. Young's moduli of both the background and inclusion are set to E=9kPa. The viscous coefficient is set to β=0.001s. The body force is applied at the center of the inclusion. The DSDA procedure directly computes the steady-state displacement amplitude of the focal point for three different excitation frequencies: 25Hz, 50Hz and 100Hz. The results are D_{25}=3.30μm, D_{50}=3.13μm and D_{100}=2.71μm. The explicit dynamic analysis results for the same setting are illustrated in Fig. 3.11. The corresponding displacement amplitudes

are D_{25}=3.27μm, D_{50}=3.11μm and D_{100}=2.68μm, indicating good agreement between the two analytical procedures. It also shows that the dynamic response of the viscoelastic soft tissue converges to its steady state quickly.

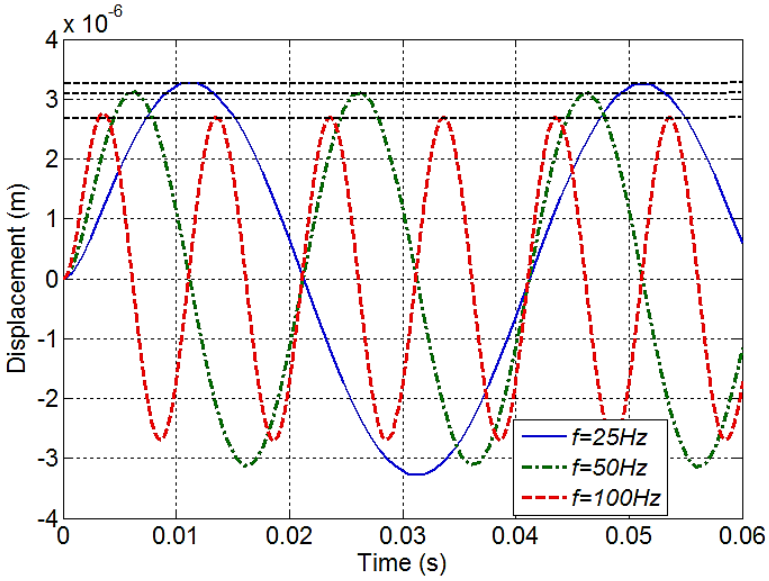

Figure 3.11. Dynamic responses of the focal point simulated with explicit dynamic analysis. The background and inclusion are assigned the same mechanical properties: E=9kPa and β=0.001s. The three dashed straight lines indicate the displacement amplitudes for f=25Hz, 50Hz and 100Hz are D_{25}=3.27μm, D_{50}=3.11μm and D_{100}=2.68μm, respectively.

In order to investigate the CTE of HMI for viscoelastic material, seven inclusion-to-background elastic contrasts (true stiffness contrast) were studied: 1:30 (-29.6dB), 1:10(-20dB), 1:3(-9.6dB), 1:1 (0dB), 3:1(9.6dB), 10:1(20dB), and 30:1 (29.6dB). Two kinds of Young's moduli of the background are studied: $E_{background}$=3kPa and 9kPa. For each case, four different viscous coefficients are applied to the background: $\beta_{\text{background}}$=0.0002s, 0.0005s, 0.001s and 0.005s. After the viscoelastic properties of the background are assigned, the Young's modulus of the inclusion changes to obtain

different inclusion-to-background elastic contrasts, but the viscosity of the inclusion is assumed to be the same as the background. In addition, harmonic forces with three different frequencies are used as the excitation.

The simulation results are shown in Figs. 3.12 and 3.13. Two relations are plotted: observed stiffness contrast versus true stiffness contrast, and contrast-transfer efficiency versus true stiffness contrast. They are also compared with the ideal case in which the observed stiffness contrast equals the true stiffness contrast and $CTE(dB)$=0. For all cases, the CTE decreases as $|C_t(dB)|$ increases. For the low viscosity background, the CTE performance is quite good for $|C_t(dB)|<10dB$. As the viscosity of the background increases, the CTE generally decreases.

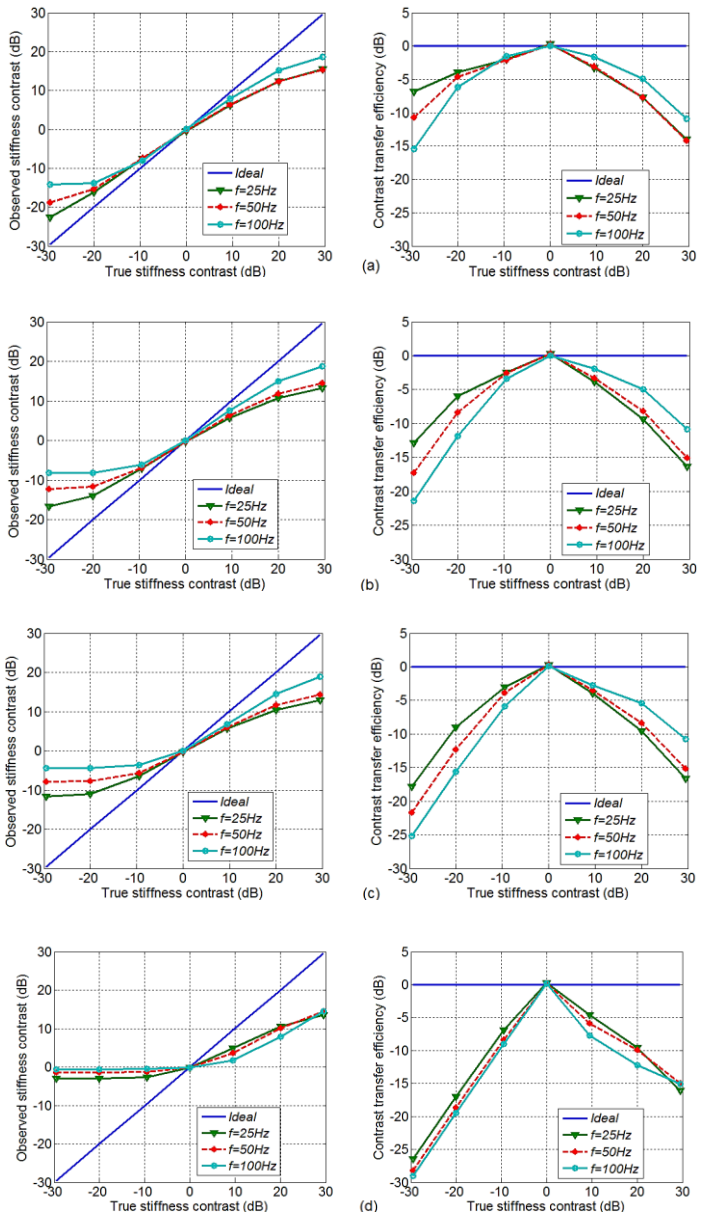

Figure 3.12. Observed stiffness contrast $C_o(dB)$ versus true stiffness contrast $C_t(dB)$ (Left), and contrast-transfer efficiency $CTE(dB)$ versus true stiffness contrast $C_t(dB)$ (Right) for $E_{background}$=3kPa. The results are compared with the ideal relation that the observed stiffness contrast equals the true stiffness contrast and CTE (dB) =0. Four different viscous coefficients are studied: (a) $\beta_{background}$=0.0002s, (b) $\beta_{background}$=0.0005s, (c) $\beta_{background}$=0.001s and (d) $\beta_{background}$=0.005s.

For hard inclusion in soft background ($C_t(dB)>0$), the harmonic force frequency f=100Hz gives the best CTE performance except for $\beta_{background}$=0.005s. For f=25Hz and 50Hz, CTE does not change much as the viscosity of the background increases. In this case, the hard inclusion has the same viscosity as the soft background, which means the hard inclusion has smaller viscous coefficient $\beta_{inclusion}=\eta/\mu$ and elasticity of the tissue dominates the dynamic response of the tissue. As is shown in Table 3.2, for example, $\beta_{inclusion}$=0.00017s for $\beta_{background}$=0.005s when C_t=30:1 ($C_t(dB)=29.6dB$). Then the observed stiffness contrast is not affected much in the cases of small viscous coefficients. However, a higher frequency motion (f=100Hz) is damped more in the high viscosity case ($\beta_{background}$=0.005s), which may dominate the dynamic response of the tissue and lead to low observed stiffness contrast.

Table 3.2. Viscoelastic properties of the inclusion for different inclusion-to-background elastic contrasts (C_t) when $E_{background}$=3kPa and $\beta_{background}$=0.005s ($\eta_{background}$=5.0Pa s).

C_t (dB)	$E_{inclusion}$ (kPa)	$\eta_{inclusion}$ (Pa s)	$\beta_{inclusion}$ (s)
-29.6	0.1	5.0	0.15
-20	0.3	5.0	0.05
-9.6	1.0	5.0	0.015
0	3.0	5.0	0.005
9.6	9.0	5.0	0.0017
20	30	5.0	0.0005
29.6	90	5.0	0.00017

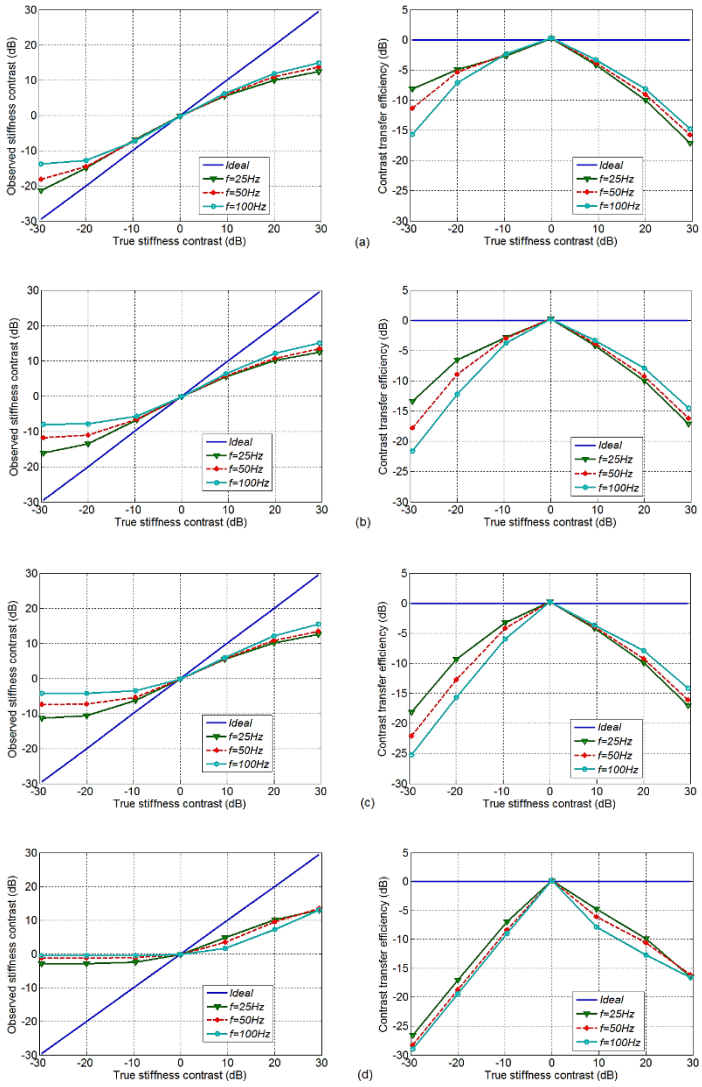

Figure 3.13. Observed stiffness contrast $C_o(dB)$ versus true stiffness contrast $C_t(dB)$ (Left), and contrast-transfer efficiency $CTE(dB)$ versus true stiffness contrast $C_t(dB)$ (Right) for $E_{background}$=9kPa. The results are compared with the ideal relation that the observed stiffness contrast equals the true stiffness contrast and CTE (dB) =0. Four different viscous coefficients are studied: (a) $\beta_{background}$=0.0002s, (b) $\beta_{background}$=0.0005s, (c) $\beta_{background}$=0.001s and (d) $\beta_{background}$=0.005s.

For soft inclusion in hard background ($C_t(dB)<0$), the CTE performance is highly related to the viscosity of the tissue and CTE declines as the viscosity increases. Here, f=100Hz always gives the worst CTE performance, even for $\beta_{background}$=0.0002s, the CTE performance gets quite poor for $C_t(dB)<-20dB$. The CTE performance of f=25Hz and 50Hz also gets very poor for $C_t(dB)<-20dB$ as the viscosity increases. When $\beta_{background}$=0.005s, all three harmonic force frequencies give very low CTE for $C_t(dB)<0$ and the observed stiffness contrast $|C_o(dB)|$ becomes very small. In this case, the soft inclusion has the same viscosity as the hard background, which leads to a much higher viscous coefficient of the inclusion. Similar to the hard inclusion in soft background case, as is shown in Table 3.2, for example, $\beta_{inclusion}$=0.15s for $\beta_{background}$ =0.005s when C_t=1:30 $(C_t(dB)=-29.6dB)$. Then, the viscosity dominates the dynamic response of the inclusion especially for the higher frequency harmonic force, which results in the poor CTE performance for the soft inclusion in hard background case.

Two kinds of Young's moduli of the background ($E_{background}$=3kPa and 9kPa) give similar CTE performance. That means CTE of HMI is not sensitive to the elasticity of background but the inclusion-to-background elastic contrast and the viscosity of the tissue.

3.2.4 Summary

In summary, the contrast-transfer efficiency of HMI decreases as $|C_t(dB)|$ increases. The CTE generally decreases as the viscosity of the tissue increases. A higher excitation frequency is more affected by the viscosity and the corresponding CTE declines faster as the viscosity of the tissue increases. The CTE of soft inclusion in hard background are

more sensitive to the viscosity of tissue than that of hard inclusion in soft background. As the viscosity increases, HMI becomes less efficient in depicting the stiffness contrast of soft inclusion in hard background than that of hard inclusion in soft background. It is also observed that CTE of HMI is not sensitive to the elasticity of background tissue.

3.3 Evaluation of the Simplified Quantitative Model

In Section 3.1 and 3.2, the effects of global boundary conditions and heterogeneity on the localized ARF induced responses are investigated for a qualitative imaging method within the ROE, i.e., HMI. For the quantitative imaging within the ROE, the simplified quantitative model should also be justified.

The ARF induced creep imaging methods have been developed for quantitative imaging the time constant within the ROE. In these methods, a single degree-of-freedom (SDF) model based on the relation of creep strain due to a step stress is used to model the relation between the creep displacement and the step ARF. The SDF assumption can highly simplify the analytical model of the soft tissue viscoelastic characterization. The physical basis for this assumption is that the ARF generated by focused ultrasound is highly localized, and the response of the induced tissue is assumed to be only related to the local distribution of the mechanical properties. At the same time, it should be noted that the SDF assumption actually implies a homogeneous assumption in the analysis of each response. However, these approximations become challenging when considering the three dimensional (3D) nature of the original problem and in the presence of heterogeneity.

The limitations on the SDF model can be overcome by using finite element (FE) method, which is capable of modeling complicated geometries, material heterogeneities, complex mechanical models, and boundary conditions of biological soft tissue. [16] Thus, the dynamic behavior of viscoelastic soft tissue can be simulated with FE modeling without the SDF and homogeneous assumptions. Different soft tissue viscoelasticity, ARF configurations and model heterogeneity can be effectively modeled and parametrically studied by employing FE.

The purpose of this study is to investigate the fundamental limitation of the commonly used SDF and homogeneous assumptions in ARF induced creep imaging. Computational experiments were performed by FE simulations. For homogeneous model, the SDF assumption was evaluated quantitatively by analyzing the inverse problem with this assumption. For heterogeneous model, a qualitative analysis was performed by comparing the dynamic responses of the homogeneous model with that of the heterogeneous model, which demonstrated the limitations of the SDF and homogeneous assumptions in the presence of model heterogeneity.

3.3.1 Creep Response of Viscoelastic Soft Tissue to Step ARF

The soft tissue in this study is assumed to be an isotropic, linear viscoelastic, and near-incompressible medium. The complex shear modulus of viscoelastic material is described by [67]

$$G = G' + iG'' \tag{3.8}$$

where G' is the shear storage modulus, G'' is the shear loss modulus, and i is the imaginary unit. For a Voigt model, the shear storage and loss moduli of Equation (3.8) become

$$G' = \mu, \quad G'' = \eta\omega \tag{3.9}$$

in which case μ is the shear modulus, ω is the angular frequency, and η is the shear viscosity.

The complex shear modulus formulation in Equations (3.8) and (3.9) is in the frequency domain, while the dynamic simulation of soft tissue to a step force is a problem in the time domain, for which the viscoelasticity of soft tissue can be modeled by Prony series expansion. Then, for linear viscoelastic material, the relaxation modulus is described by [24,75]

$$G(t) = G_\infty + \sum_{i=1}^{N} G_i e^{-t/\tau_i} \tag{3.10}$$

where $G(t)$ is the time-dependent relaxation modulus, G_∞ is the long-term modulus, and G_i and τ_i are moduli and relaxation times of the Maxwell elements, respectively. The Voigt model has instantaneous stress relaxation under a step strain test; therefore, it does not have a well-defined relaxation function with a Prony series expansion. [24] The standard linear solid model that combines a spring and Maxwell model in parallel is used to approximate the Voigt model by setting N=1 and $G_1 \gg G_\infty$ in Equation (3.10). Then, in the FE model, the viscoelastic property described by the Prony series can be calculated by

$$G(t) = G_\infty + G_1 e^{-t/\tau_1} \tag{3.11}$$

$$\tau_1 = \eta/G_1\,, \qquad G_\infty = \mu, \qquad G_1 = kG_\infty\ (k \gg 1) \tag{3.12}$$

where *k* is a constant and is set to 100 in this study for consideration of both accuracy and computational efficiency.

In ARF creep imaging, the creep response of viscoelastic soft tissue has been studied with the relation [21,36,55,57]

$$u(t) = A\left(1 - e^{-t/\tau}\right),\ \ \tau = \frac{\eta}{\mu} \tag{3.13}$$

where $u(t)$ is the creep displacement of the focal point, *A* is the steady state displacement decided by the configuration of the ARF and shear modulus (μ), and τ is the time constant that describes the ratio of shear viscosity to shear elasticity of the material. Based on Equation (3.13), the time constant, τ, can be estimated by fitting to the time-dependent creep displacement, which in practice is measured by the diagnostic ultrasound transducer. In Equation (3.13), the relation between the creep displacement and the step ARF is based on the model of creep strain due to a step stress. Strictly speaking, this relation is only accurate for system without mass, in which case the stress is proportional to the applied force and the creep strain is proportional to the creep displacement. Thus, Equation (3.13) is actually an approximation based on the fact that the ARF is highly localized. In this study, the errors associated with this approximation will be evaluated.

The above SDF model did not consider the inertia effects, which are important in a dynamic analysis. In ARF creep imaging, there is another SDF model built with the

mass considered. Viola and Walker modified the model by adding an inertial component in series with the Voigt model, and solved for the time-dependent displacement induced by a step ARF [55]

$$u(t) = A(1 - \frac{\xi + \sqrt{\xi^2 - 1}}{2\sqrt{\xi^2 - 1}} e^{-(\xi - \sqrt{\xi^2 - 1})\omega_o \cdot t} + \frac{\xi - \sqrt{\xi^2 - 1}}{2\sqrt{\xi^2 - 1}} e^{-(\xi + \sqrt{\xi^2 - 1})\omega_o \cdot t}) \quad (3.14)$$

$$\tau = \frac{2\xi}{\omega_o} \quad (3.15)$$

with ξ the damping ratio, ω_o the natural frequency, and τ the time constant that defines the ratio of shear viscosity to shear elasticity of the material. Based on Equation (3.14), ξ and ω_o can be estimated by fitting to the time-dependent creep displacement. The time constant τ can be given by Equation (3.15). However, in this study, it is shown that this model does not improve the estimation accuracy in the inverse problem due to the fundamental limitations of the SDF assumption.

3.3.2 Finite Element Model

As described in Chapter 2, ARF is a spatial-varying body force. For quantitative imaging, the ARF model should represent its spatial distributions. The focal zone of ARF is a Gaussian-shaped beam, and simplified models have been used to model the ARF distribution, such as 3D Gaussian function, superposition of a series of disks with varying force magnitudes and radii, and ellipsoid of rotation. [37,76] These models are simplified patterns of the actual ARF distribution, but they can well capture the main properties of

the spatial-varying body force. [77] Here, the step ARF is described by a 3D Gaussian function as [37,78]

$$f(r,z;t) = f_o H(t) e^{-(\frac{r^2}{2\sigma_r{}^2}+\frac{z^2}{2\sigma_z{}^2})} \tag{3.16}$$

where r and z are the radial and axial positions relative to the center (r=0 and z=0) of the focal zone, respectively, t is time from the beginning of the excitation, $f(r, z; t)$ is the time-varying body force density; f_o is the spatial peak density of the body force, $H(t)$ is the Heaviside step function representing a unit step, and σ_r and σ_z are parameters that decide the dimension of the body force. In practice, the distribution of the body force is decided by the frequency of the transducer, the speed of sound in the tissue, the attenuation of the media, and the F-number of the transducer. The F-number of an ultrasound transducer, F_{number}, is given by

$$F_{number} = \frac{F}{D} \tag{3.17}$$

where F is the focal length and D is the diameter of the aperture. [45] Given that other factors are fixed, the lateral beam width (-6dB) of the focal zone is proportional to F_{number}, and the axial length (-6dB) is proportional to the square of F_{number} . [52] In our study, the body force field for a 3.25MHz focused transducer with F=50mm, D=60mm, and inner diameter d_{in}=22.6mm (Sonic Concepts, Bothell, WA) is modeled. The F-number is equal to 0.83. The normalized distribution of the acoustic radiation force intensity for the 3.25MHz focused transducer and the 3D Gaussian function are shown in

Fig. 3.14. The -6dB beam width of the focal zone is about 0.6mm and the -6dB axial length of the focal zone is about 3.2mm.

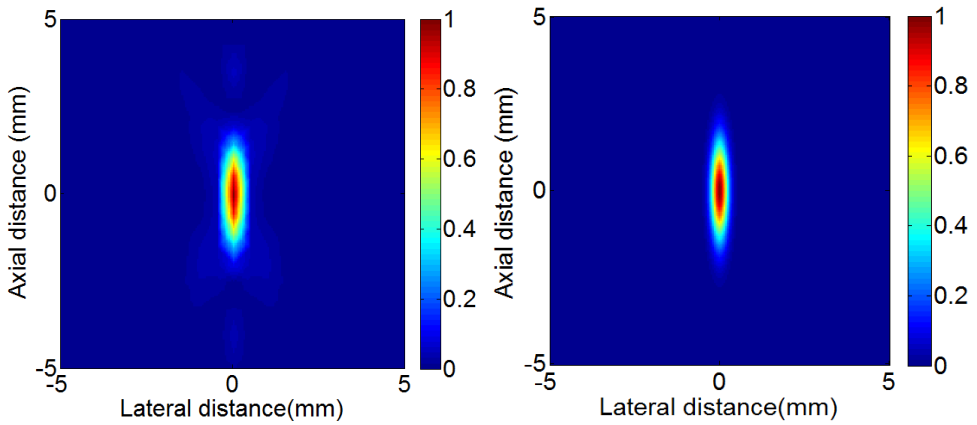

Figure 3.14. Normalized distribution of the acoustic radiation force intensity for (a) 3.25MHz focused transducer (Sonic Concepts, Bothell, WA) and (b) 3D Gaussian function.

The SDF model was studied for different ARF configurations in the simulation. First, ARFs with the same relative distribution but different magnitude, $0.5f_o$, f_o, and $2f_o$, are assigned as the body force magnitude as is described in Equation (3.16). Then, for ARFs with the same magnitude, the relative distribution can be changed by modeling transducers with different F-numbers. Here, three F-numbers are studied: 1.5, 0.83, and 0.5, of which the first one has a larger focal zone and the third one has a smaller focal zone compared to the one discussed above (F_{number} = 0.83).

In this study, axisymmetric FE models are developed to simulate the viscoelastic soft tissue. Diagrams of the axisymmetric models are shown in Fig. 3.15 (a). The dimensions of the modeled geometry are 24mm in radius and 48mm in height. For each

case studied in this study, the ARF is always applied along the axial direction (z direction). The origin of the coordinate system of this model is located at the center of the symmetry axis, i.e., center of geometry of this axisymmetric model. The distribution of the ARF is given by Equation (3.16), and the ARF focuses at the origin. As shown in Fig. 3.15 (a), the bottom boundary of the FE model is fixed in all directions; other surfaces of the model are not constrained.

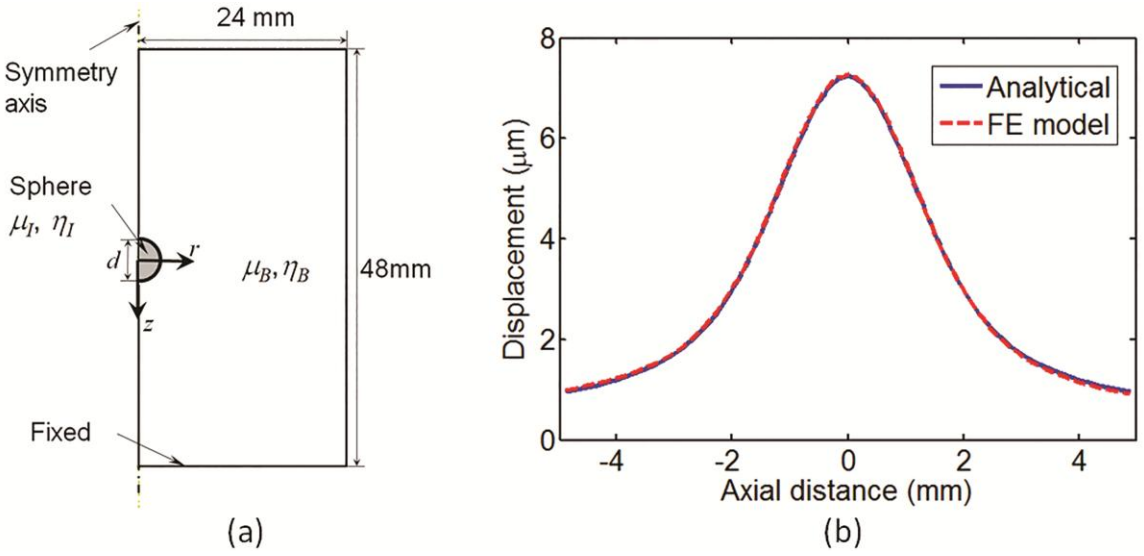

Figure 3.15. Model diagram and validation: (a) Diagram of the axisymmetric model with a spherical inclusion in the center of the model; and (b) Axial displacement induced by ARF for the homogeneous case with μ=3kPa. The horizontal axis in (b) is the axial distance from the focal center.

The axisymmetric model allows for a highly refined mesh for the focal zone without increasing too much the computational time. The model consists of 5366 nodes and 5275 elements. The mesh for the region near the focal zone is refined with a minimum mesh size of 0.05mm, which ensures that the lateral variation of the ARF can be captured by the FE model due to the small radial dimension (-6dB) of the ARF, which is in the order of 0.5mm. The FE simulations were implemented with ABAQUS implicit dynamic analysis. The time-dependent creep displacements of the ARF focal center are obtained from the FE simulations, and then used for the analysis. In order to evaluate the effectiveness of SDF models in describing soft tissue as well as explore the limitations of SDF models, a homogenous case and a heterogeneous one are simulated. Their specific attributes are discussed hereafter.

In order to ensure the accuracy of the FE model, the FE simulation results were first compared to the analytical solution presented in Equation (2.3) for the homogeneous case with μ=3kPa. The computed axial displacements induced by the ARF described in Fig. 3.14 (b) are shown in Fig. 3.15 (b). The results show good agreement between the FE simulation and analytical solution. It should be noted that in the negative axial distance region, the displacement from the FE simulation is slightly greater than that from the analytical solution, while it is opposite in the positive axial distance region. The reason for this behavior is that the analytical solution is developed based on an infinite model assumption, but our FE model has boundaries, and the negative axial distance region is near the top free surface while the positive axial distance region is near the constrained bottom boundary. Accurate analytical solutions for the dynamic responses of viscoelastic soft tissue to ARF cannot be easily solved, especially for models with finite geometry and heterogeneity. [45] Equations (3.13) and (3.14) are only approximate solutions based on SDF and homogeneous assumptions, which is not capable of modeling the 3D configuration of the dynamic system and shear wave reflections due to heterogeneity, while they can be modeled with the FE method.

3.3.3 Evaluation of the Simplified Model in Homogeneous Case

In order to investigate the associated errors in soft tissue characterization with the SDF assumption, homogeneous models with different mechanical properties and ARF configurations are first studied. Four shear moduli (μ=1kPa, 3kPa, 9kPa and 27kPa) and three time constants (τ = 0.0003s, 0.0009s and 0.0027s) are studied with the FE model. The shear moduli chosen are within the range of reported mechanical properties of the

normal or tumorous human soft tissues. [6,79] The time constants used are on the same order as reported values for soft tissues or phantoms. [21,28,38,40,56]

The SDF assumption was evaluated quantitatively by analyzing the inverse problem with the SDF model. The data from the computational experiments are generated from the FE simulation. Since the purpose of this study is to investigate the fundamental limitation of the SDF and homogeneous assumptions in ARF creep imaging, these data do not contain noise as in practical measurements in order to control variables in the analysis. The results in this study should be considered as the best theoretically achievable ones.

The time constant, τ, is reconstructed by fitting Equation (3.13) or (3.14) with the FE simulated creep displacements. This is an optimization problem described by

$$\min_{\boldsymbol{p}} \pi(\boldsymbol{p}), \qquad \pi(\boldsymbol{p}) = \frac{1}{2}\sum_{i=1}^{N}\left|u_i^{exp}(t_i) - u_i(t_i\,;\,\boldsymbol{p})\right|^2 \tag{3.18}$$

where $\pi(\boldsymbol{p})$ is the objective function, $\boldsymbol{p}$ is the vector of parameters for optimization ($\boldsymbol{p}$=[A τ] for Equation (3.13) and $\boldsymbol{p}$=[A ξ ω_o] for Equation (3.14), N is the number of the sampled data, $u_i^{exp}(t_i)$ is displacement from FE simulation at time t_i, and $u_i(t_i\,;\,\boldsymbol{p})$ is the calculated displacement from Equation (3.13) or (3.14) with the current parameter $\boldsymbol{p}$. In this study, the optimization problem is solved with the Nelder-Mead simplex optimization algorithm. [80] As it was discussed, the reconstructions based on Equation (3.13) or (3.14) will result in estimation errors. The relative estimation error (REE) of τ is defined by

$$REE = \frac{|\hat{\tau} - \tau|}{\tau} \times 100\% \tag{3.19}$$

with τ denoting the true time constant assigned to the FE model in the simulation, and $\hat{\tau}$ the time constant reconstructed by solving the optimization problem.

For homogeneous models with different mechanical properties, the creep displacement for each case is shown in Figs. 3.16 (a), (b), and (c). In order to show the temporal behavior of the response, the displacements are normalized in Figs. 3.16 (d), (e), and (f). Responses for material with the same time constant, τ, are plotted in each figure as they are expected to have the same temporal behavior according to the SDF model described by Equation (3.13). In Figs. 3.16 (a), (b), and (c), even though the viscosity (or time constant) is different, the near steady state displacement is almost identical for the same elasticity and is inversely proportional to the elasticity of the tissue. That observation confirms that the steady state displacement is a good metric to image the elasticity relation between homogeneous models if the same ARF is applied in the focal zone. [21,36,55,56] The normalized displacements shown in Figs. 3.16 (d), (e), and (f) represent the temporal response behavior of soft tissue to step ARF. For the same time constant, based on the SDF model of Equation (3.13), the temporal behavior is expected to be identical for different shear moduli. However, the viscoelastic constitutive model actually describes the relation between stress and strain, not between the applied force and displacement. Equation (3.13) is derived from the SDF model, in which the stress is proportional to the applied force and the creep strain is proportional to the creep displacement. [56] This is not the case for a 3D model with the inertia effects considered.

It is noticed that the response curve deviates from the SDF case for the same time constant as the shear modulus of the model decreases. In addition, as the time constant increases, all the response curves converge to the SDF case.

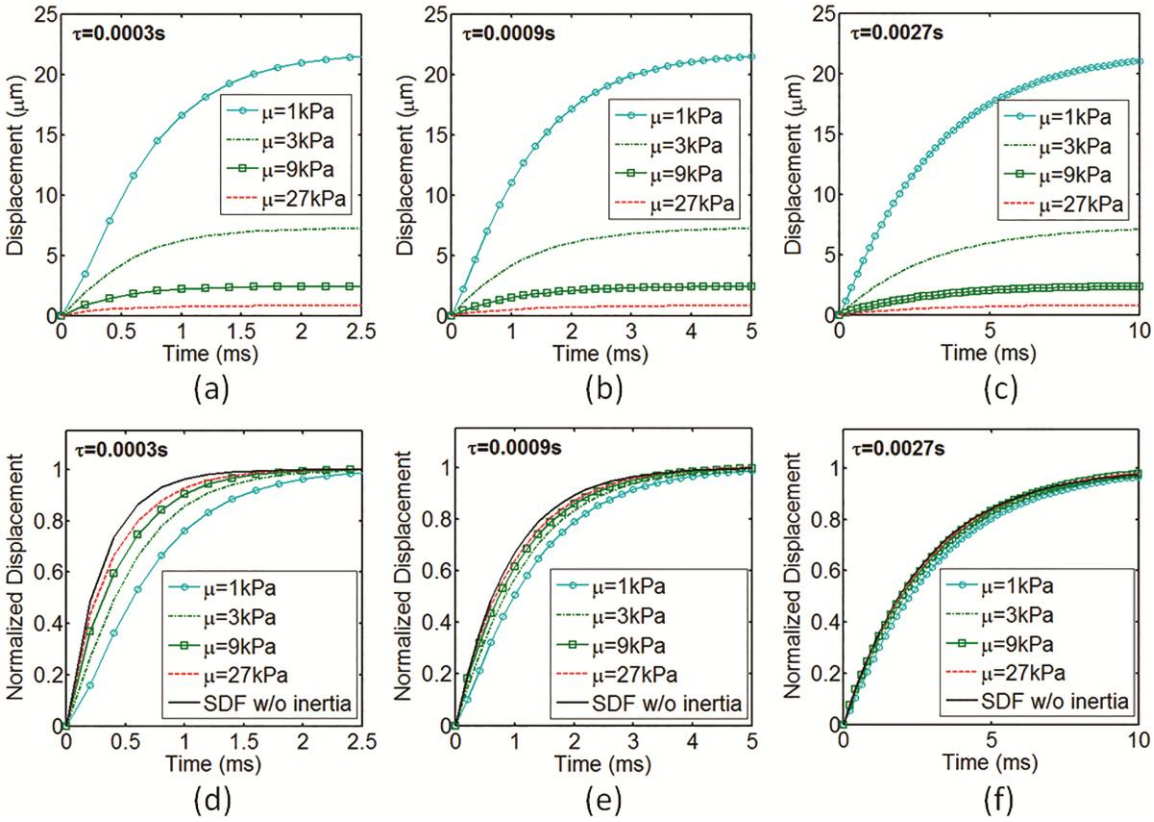

Figure 3.16. Creep displacement responses to step ARF for soft tissue with different viscoelasticity. Three time constants are studied: (a) τ=0.0003s, (b) τ=0.0009s, and (c) τ=0.0027s. The corresponding normalized creep displacement responses are shown in (d) τ=0.0003s, (e) τ=0.0009s, and (f) τ=0.0027s.

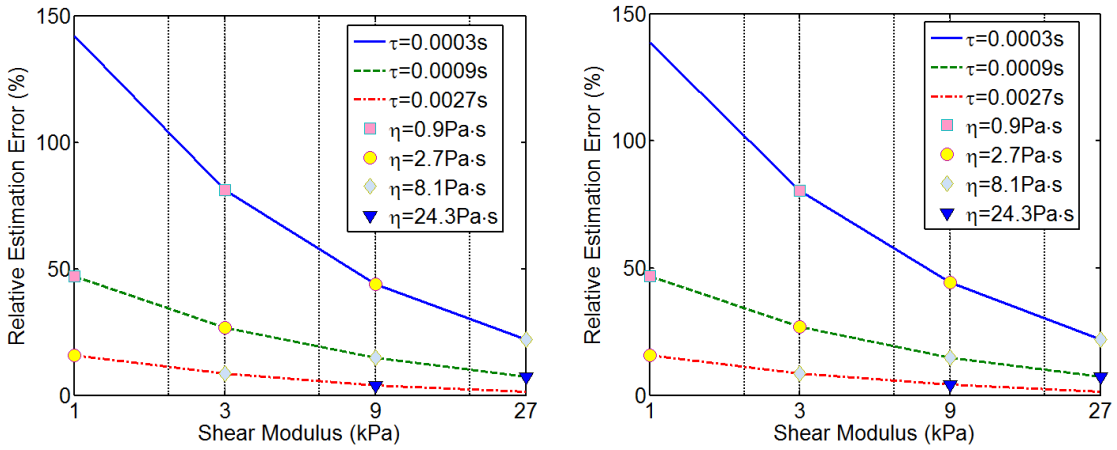

Figure 3.17. Relative estimation error (REE) of τ by fitting the SDF models with the simulated creep displacement responses of the FE model. Each marker represents cases with the same shear viscosity. (a) is for the SDF model described by Equation (3.13) without considering the inertial effect; and (b) is for SDF model described by Equation (3.14) with the inertial component included.

The above mentioned trends can also be observed in Fig. 3.17 (a)**,** which plots the relative estimation error (REE) with this SDF model. In this figure, the horizontal axis is a logarithmic scale. Each marker represents cases with the same shear viscosity. The REE can be quite large for models with low time constant and elasticity, e.g., 142% for $\mu = 1kPa$ and $\tau = 0.0003s$. It should be indicated that even the REE decreases as the elasticity increases for the same time constant, REE increases as the elasticity increases for the same viscosity, as shown by the markers in Fig. 3.17 (a). In a Voigt model for the same time constant, the viscosity is proportional to the elasticity. This means that for the same time constant, the REE decrease is due to the increased viscosity, not elasticity. These results indicate that the SDF model tends to have better approximation for tissue with high viscosity and low elasticity, in which cases the SDF model may still be

preferred in qualitative imaging for its simplicity. Figure 3.17 (b) illustrates the REE with the SDF model that included the inertial component. It should be noted that adding the inertial component into the SDF model does not significantly improve the estimation accuracy, because for a 3D dynamic system, not only the focal region but also the surrounding tissue is induced to motion by the ARF, and the complex system inertia cannot be accurately counted by a SDF dynamic system, which is the fundamental limitation of the SDF approach.

In order to ensure the REE is not resulted from the optimization process, the objective function $\pi(\boldsymbol{p})$ is evaluated near the true value of $\boldsymbol{p}$ that is assigned to the FE model. For one of the cases in Fig. 3.18 that the creep displacement data were generated from the homogenous FE model with μ=3kPa and τ=0.0009s, the contour of the objective function $\pi(\boldsymbol{p})$ is plotted near the true value τ=0.0009s as shown in Fig. 3.18. In particular, Fig. 3.18 (a) is the case that the creep displacement data are fitted with the SDF model without the inertial component. For Fig. 3.18 (b), the SDF model with the inertial component is used in the objective function $\pi(\boldsymbol{p})$. In this case, $\boldsymbol{p}$=[A ξ ω_o], and only the contour near the true value τ=0.0009s is interested. Based on Equation (3.15) and assuming that A is known (equal to the steady state displacement), the contour of $\pi(\boldsymbol{p})$ with respect to ω_o and τ can be obtained in Fig. 3.18 (b). The two τ that make $\pi(\boldsymbol{p})$ reach the minimum in Fig. 3.18 are the same as the ones used to calculated the REE in Fig. 3.17. This result suggests that the REE is resulted not from the optimization process, but from the fundamental limitation of the SDF models.

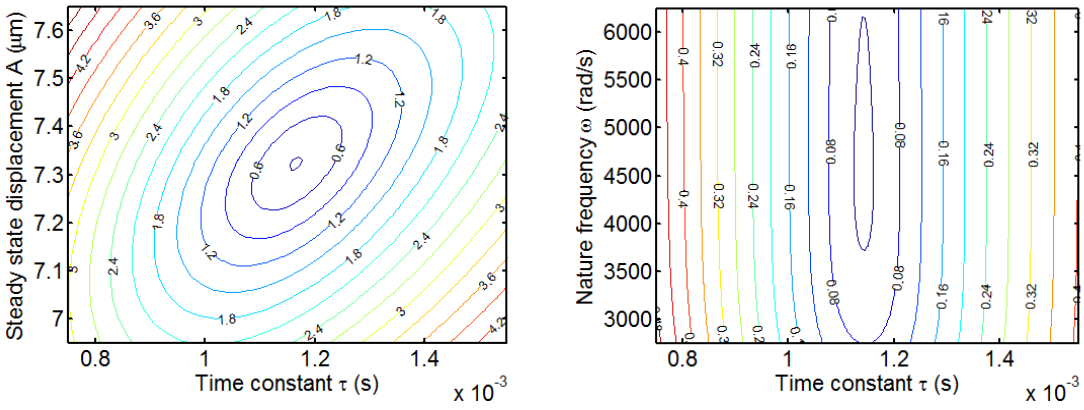

(a) (b)

Figure 3.18. Contour of the objective function $\pi(\boldsymbol{p})$ near the true value $\tau = 0.0009$s. The creep displacement data were generated from the homogeneous FE model with μ =3kPa, and τ =0.0009s. The models used for fitting the creep displacement data are described by (a) Equation (3.13) and (b) Equation (3.14).

The creep displacement responses for different ARF configurations are shown in Figs. 3.19 (a) and (b). Specifically, Fig. 3.19 (a) depicts the responses for ARFs with different magnitude, but the same distribution with F_{number} =0.83; and Fig. 3.19 (b) illustrates the responses for ARFs with different distribution, but the same magnitude f_o for the body force described in Equation (3.16). The corresponding normalized creep displacement responses are shown in Figs. 3.19 (c) and (d). The steady state response is affected by both the magnitude and distribution of the body force. However, the temporal response of soft tissue is not affected by the body force magnitude, as shown in Fig. 3.19 (c). The results confirm the findings that the time constant is a "force-free" parameter in the analysis with the SDF model. Figure 3.19 (d) demonstrates that the induced responses by a smaller focal zone are closer to the output of the SDF model. The time constant τ was then reconstructed with the SDF model described by Equation (3.13), and the REEs

for ARF corresponding to F_{number} =1.5, 0.83, and 0.5 are 68%, 27%, and 12%, respectively. The results suggest that decreasing the focal zone can reduce the inertia effects on the dynamic responses of soft tissue, which means that when using the SDF model in ARF creep imaging, a smaller focal zone is desired to reduce the REE. This is similar to other imaging methods, e.g., ARFI and HMI, in which smaller focal zones result in better image contrast. [61,81]

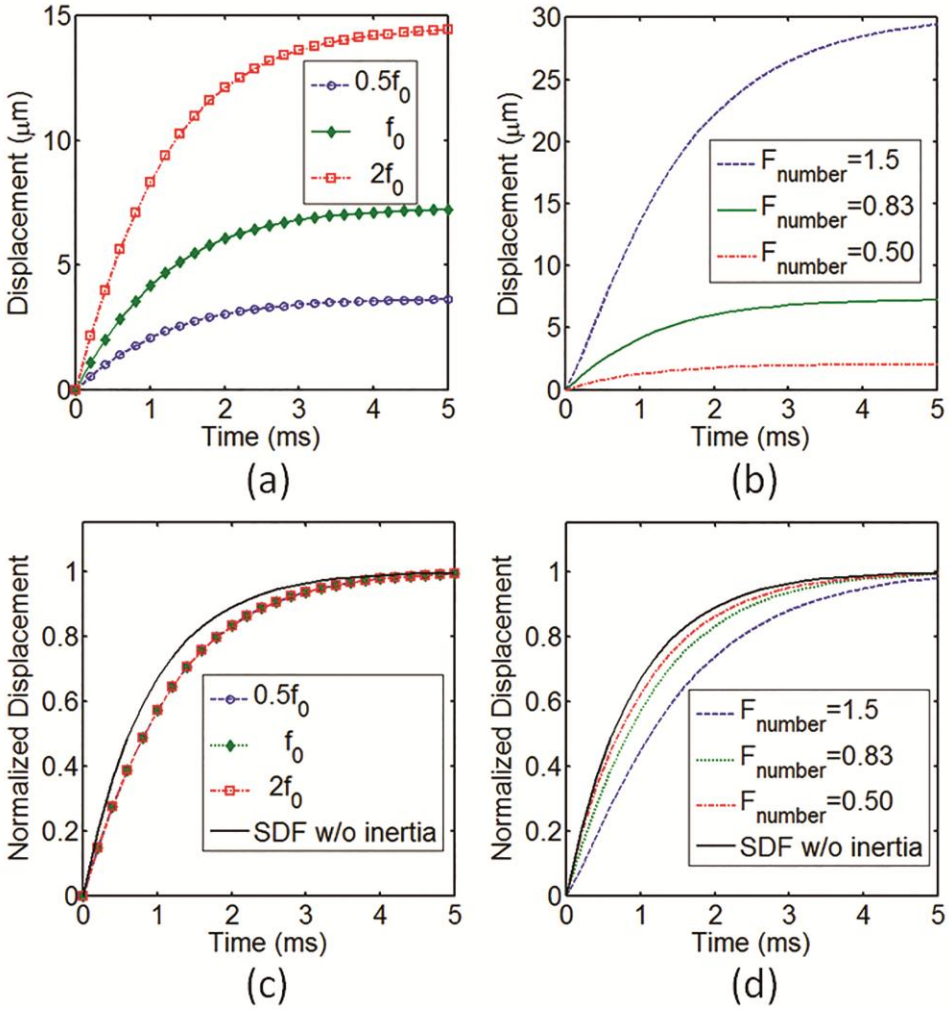

Figure 3.19. Creep displacement responses with different ARF configurations: (a) ARFs with different magnitude, but the same distribution, i.e., F_{number} =0.83; and (b) ARFs with different distribution, but the same magnitude, i.e., f_o. The corresponding normalized creep displacement responses are shown in (c) and (d). The model is homogeneous, and the viscoelastic parameters are μ =3kPa, and τ =0.0009s.

3.3.4 Evaluation of the Simplified Model in Heterogeneous Case

In order to demonstrate the limitations of the SDF and homogeneous assumptions in the presence of tissue heterogeneity, a qualitative analysis is performed by comparing the

temporal and steady state responses of the homogeneous model to that of the heterogeneous model. In this study, spherical inclusions are located in the center of the model, as illustrated in Fig. 3.15 (a). There are two cases considered: spheres with diameters of 3mm and 6mm. Both the background and inclusion are assigned with the same time constant. Three background and inclusion shear modulus combinations, (μ_B, μ_I), are studied, namely, (*3kPa*, *3kPa*), (*0.3kPa*, *3kPa*), and (*30kPa*, *3kPa*).

Under the homogeneous assumption, the steady state displacement, *A*, is inversely proportional to the underlying tissue elasticity (or shear modulus). In the heterogeneous media, the observed elasticity contrast, can be described by

$$C_o = \frac{A_{background}}{A_{inclusion}} \tag{3.20}$$

where C_o is the observed elasticity contrast of the inclusion to background, $A_{background}$ is the steady state displacement of the background, and $A_{inclusion}$ is the steady state displacement inside the inclusion. Here, $A_{inclusion}$ is measured at the center of the inclusion, where the response is least affected by the heterogeneity. For regions near the boundary of the inclusion and background, the response can be more severely affected by heterogeneity, which results in a further reduced elasticity contrast. The ideal performance of a biomechanical imaging method is that the observed elasticity contrast equals the true elasticity contrast.

To qualitatively illustrate the effect of heterogeneity and the fundamental limitation of the homogeneous assumption in modeling the dynamic behavior of soft tissue to step ARF, the creep displacement responses at the origin of the heterogeneous

models (center of the spherical inclusion) are shown in Fig. 3.20. The ARF is considered as a highly localized force in most ARF based imaging methods and the dynamic response is considered to be only related to the underlying local mechanical properties, which is equivalent to a homogeneous assumption of the imaged tissue. However, the results indicate that the local heterogeneity greatly affects the dynamic response of the focal zone. For inclusion with the same shear modulus, ($\mu_I = 3kPa$), the responses vary as the background's moduli change. In addition, the steady state displacements can no longer reflect the true elasticity contrast of the inclusion to the background as shown in Table 3.3. As the dimension of the inclusion increases from 3mm to 6mm in diameter the observed elasticity contrast gets closer to the true elasticity contrast.

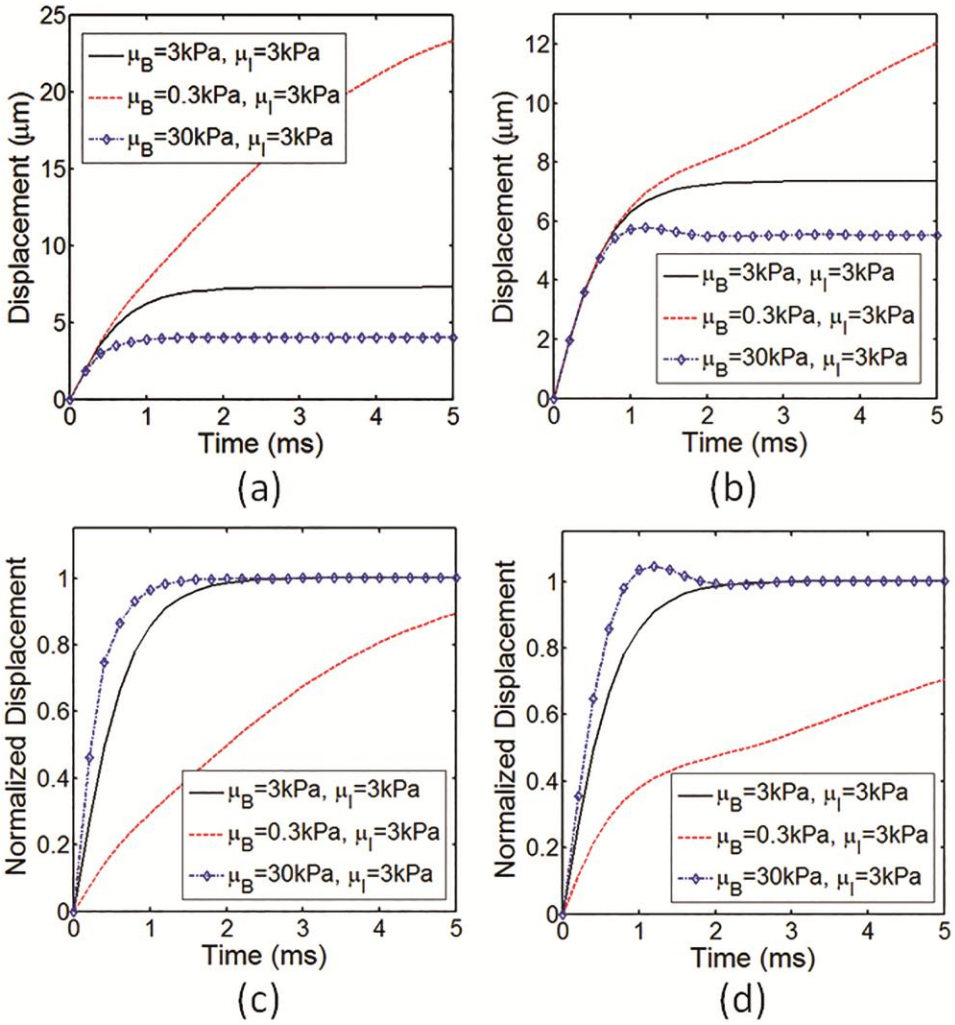

Figure 3.20. Creep displacement responses at the origin of the heterogeneous models with different inclusion sizes: (a) Sphere with diameter 3mm; and (b) Sphere with diameter 6mm. The corresponding normalized creep displacement responses are shown in (c) and (d). The solid black line is the homogeneous case. τ=0.0003s for both background and inclusion.

Table 3.3. Observed elasticity contrast for heterogeneous models

μ_I (kPa)	μ_B (kPa)	True elasticity contrast	Observed elasticity contrast	
			3mm-diameter inclusion	6mm-diameter inclusion
3	0.3	10	2.9	4.2
3	3	1.0	1.0	1.0
3	30	0.10	0.18	0.13

The ARF induced displacement is the integration of the normal strain in the axial direction. Figures 3.21 explain the reduced contrast for heterogeneous media by demonstrating the effects of heterogeneity on the axial normal strain field with the case of the 3mm-diameter spherical inclusion. The dashed line shows the profile of the inclusion. Even though the inclusions have the same shear modulus, it is shown that the strain fields are quite different for the three cases due to the differences in heterogeneity. Figure 3.21 (a) is the case for a homogeneous medium. For Fig. 3.21 (b), when the inclusion is in a soft background, the resulting displacement of the focal zone relates primarily to the strain of the background, and it reflects not only the elasticity of the inclusion but also of the background, or the heterogeneous structure of the local area. For an inclusion in a hard background, as shown in Fig. 3.21 (c), the strain field is constrained by the hard background, which results in a reduced displacement compared to the homogeneous case.

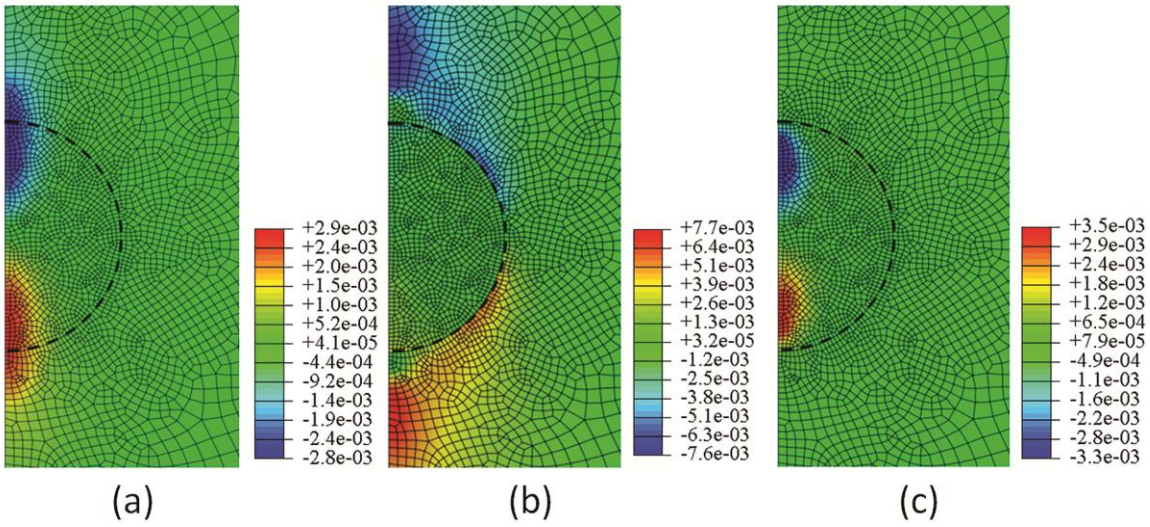

Figure 3.21. Axial normal strain field near the region of the 3mm-diameter spherical inclusion after a 10ms step ARF excitation. The dimension of the region is h=6mm (axial length) and r=3mm (radial length). The time constant is 0.0009s and the shear moduli are: (a) μ_B=3kPa, and μ_I=3kPa; (b) μ_B=0.3kPa, and μ_I=3kPa; and (c) μ_B=30kPa, and μ_I=3kPa.

The temporal responses of soft tissue to step ARF are even more complex in the presence of heterogeneity. For each figure of the normalized displacements in Fig. 3.20, the background and inclusion are assumed to have the same time constant, and ideally the responses are expected to be identical according to the SDF assumption. However, for hard inclusions in soft background, the system tends to have larger time constants, i.e., the response needs more time to reach the steady state. At the beginning, before the shear wave reaches the background, the creep displacement results from the strain inside the inclusion. When the shear wave reaches the soft background, the creep will continue in the background and the induced strain is still relatively large because the background is much softer than the inclusion, similar to the case in Fig. 3.21 (b). On the contrary, for a

soft inclusion in hard background the motion inside the inclusion is constrained and the induced strain in the background is relatively small, thus the system tends to have a smaller time constant, i.e., the displacement rises faster to its maximum value than in the homogeneous case. In that case, the shear wave reflection in the boundary leads to an overshoot in some of the responses as shown in Fig. 3.20.

Even though the SDF model has its fundamental limitations, it's still preferable in many cases involving high viscous soft tissues because it is simple and minimizes the number of parameters in the optimization, which leads to sub-optimal, but stable and robust estimation. In addition, this estimation can be improved by reducing the focal zone size. In the cases of soft tissues with low viscosity, performance of the SDF models is quite poor, and inverse procedure based on FE methods may be introduced. Even though lots of the prior information for the FE modeling (local heterogeneity profile, ARF distribution, etc.) cannot be accurately obtained, proper integration of this prior information and its uncertainty could help to improve estimation accuracy, or to enhance the observed contrast, comparing to the SDF models that do not utilize any of that prior information. Considering heterogeneity, if the inclusion region is large, the responses in the early stage are not affected by the local heterogeneity as shown in Fig. 3.20 (b), in which case the early responses may still be used under the homogeneous assumption.

3.3.5 Summary

Finite element models are developed to study the dynamic behavior of viscoelastic soft tissue subjected to step ARF. Based on the FE simulations, the fundamental limitations of the commonly used SDF and homogeneous assumptions are studied for ARF induced

creep imaging. The results suggest that the SDF model tends to have good approximation for tissue with high viscosity and low elasticity. Especially, for the low viscosity case, the estimation results based on the SDF model can be quite poor. In addition, accounting for the inertial component into the SDF model cannot effectively improve the estimation accuracy, but reducing the size of the focal zone can result in better estimation. For heterogeneous models, both the temporal and steady state responses of the focal region are highly affected by the local heterogeneity, rendering the SDF and homogeneous simplification ineffective.

3.4 Discussions

In this chapter, the finite element method is applied to investigate the dynamic behavior of viscoelastic soft tissue in ARF imaging within the ROE. It is shown that, in HMI (a qualitative imaging method), the dynamic responses within the ROE can be affected by both the global boundary conditions and local heterogeneity. For a simplified quantitative model in ARF induced creep imaging, the relative estimation error can be quite large for certain material and ARF configurations.

In order to obtain better quantitative estimation with ROE responses, all the assumptions need to be justified and FE analysis procedure considering the 3D configuration of the dynamic system may be necessary for the inverse characterization. However, as is discussed in previous section, the information that is needed to build the FE model cannot be accurately obtained in ARF imaging. Though the ARF distribution can be calculated using Field II or FOCUS ultrasound simulation package based on the properties of the medium, geometry, and center frequency of the transducer, [82,83] the

quality of the estimation is affected by the inaccurate or non-uniform attenuation coefficient as is shown in Equation (2.1). [8] In addition, reflection and nonlinear propagation of ultrasound also make the simulated ARF field inaccurate. In order to estimate the time constant in ARF induced creep imaging, the elasticity of the material should be known to build the FE model, while it's challenging to estimate the elasticity accurately in practice.

Considering the SDF model used in ARF induced creep imaging, all the uncertain information that is discussed above is discarded, and the inverse estimation is implemented based merely on the temporal responses, which leads to large estimation errors in certain cases. A possible way to improve the inverse problem is to integrate the uncertain information with the FE model. The remainder of this thesis will demonstrate an inverse finite element analysis procedure based on a Bayesian approach, which takes full advantage of the prior information of model parameters that are discarded in the SDF models.

Chapter 4: Bayesian Approach with Finite Element Model

This chapter demonstrates the inverse FE analysis procedure based on a Bayesian approach in ARF induced creep imaging. First, an introduction on the proposed method is presented. Then, the general Bayesian estimation of this problem is demonstrated. The Gaussian Process metamodeling method is then introduced as a statistical approximation of the complex FE model to make the Bayesian approach computationally feasible. In the end of this chapter, the posterior distribution of the time constant in ARF induced creep imaging is formulated with measurement noise and uncertainty model parameters.

4.1 Introduction

As is discussed in Chapter 3, simplified quantitative model has its limitations that can be surmounted by using finite element (FE) methods, which are capable of modeling complicated geometries, material behaviors, heterogeneities, and boundary conditions of soft tissues. However, most of the parameters for an FE model cannot be accurately obtained in ARF induced creep imaging. When an FE model is built to estimate the time constant by fitting the measured temporal creep displacements, one needs to configure the model with known ARF loading, boundary conditions, and elasticity of the soft tissue, the estimation of which all are subjected to considerable uncertainty. This thesis aims to integrate these uncertain parameters with the FE model to improve its estimation performance, which takes full advantage of the prior information of model parameters that are discarded in the SDF models. The proposed method is formulated based on a Bayesian approach, which has been widely used for biomedical image processing

problems. [84–87] In a Bayesian formulation, the known model parameters of the FE models are represented as probability distributions and the final characterization results are the posterior distributions of soft tissue mechanical properties rather than best-fit values from an optimization procedure, which are not a practical or a comprehensive description of the estimation in the presence of parameter uncertainty.

A straightforward solution for the above-mentioned statistical inverse problem is the Monte Carlo (MC) method, but the computationally demanding FE simulations renders the direct implementation of the MC method infeasible since it requires thousands of FE model runs. Metamodeling techniques have been developed to handle the expensive model simulations by approximating the model output. [88–90] One popular approach is the Gaussian process (GP) metamodeling, which has been developed to obtain a statistical approximation of a complex model output by using the concept of Bayesian approach, which has the advantage of providing not only the predicted value but also the prediction uncertainty. [89,91,92] In addition, this method does not need a prescribed assumption of nonlinearity on the model in contract to a polynomial regression which needs to set the degree of the polynomial. A posterior distribution of the output for a new input can be inferred by conditioning on the data of a small number complex model runs, here, FE simulations of the soft tissue models. However, in this study, the purpose is to estimate the unknown parameter of the FE model, while the GP metamodel only computes the output of model. Kennedy and O'Hagan proposed a modular Bayesian approach to incorporate GP metamodel with Bayesian estimation to calibrate model parameters. [89] They considered different sources of uncertainty, including the additional code uncertainty due to a limited number of complex model runs. Even though

the proposed method can be used for parameter calibration, the objective of their method is to make a better prediction of the true physical process output rather than the true calibration parameter. They increased the flexibility of the calibration process to better fit the experiment data by adding a discrepancy function and making some of the known parameters unknown, and used them as calibration parameters. [89] In this way, the predictive power of the fitted model is improved, but it may reduce the identifiability of the calibration parameter in conjunction with the discrepancy function and other parameters. [93,94]

This chapter explores the integration of the Bayesian approach with the FE model to solve a statistical inverse problem in ARF induced creep imaging of the viscoelasticity metric, time constant.

4.2 Bayesian Estimation

As is discussed in Chapter 3, in ARF induced creep imaging, ARF pulses with a high duty cycle have been used to mimic the step forcing function. Single degree-of-freedom (SDF) (or discrete model in [36]) simplified models have been developed to describe the induced temporal responses. Assuming a Voigt viscoelastic model yields the relation

$$U(t) = U_{ss}\left(1 - e^{-t/\tau}\right) = U_{ss}u(t)\,, \quad \tau = \frac{\eta}{\mu} \tag{4.1}$$

where $U(t)$ is the creep displacement of the focal point at time t, U_{ss} is the steady state displacement, $u(t)$ is the normalized (by U_{ss}) displacement, μ is the shear modulus, η is the shear viscosity, and τ is the time constant (or retardation time) that describes the ratio of shear viscosity to shear modulus of the material. For a time series $\boldsymbol{t} = [t_1, \ldots t_n]^T$, the

experimental creep displacements $\boldsymbol{Y} = [Y(t_1), \dots Y(t_n)]^T \; within \; the \; ROE$ are measured. In order to fit the temporal responses, the data are normalized by the averaged steady state responses, which yields $\boldsymbol{y} = [y(t_1), \dots y(t_n)]^T$. Each measurement is a noisy version of the true tissue motion. Suppose a model for this dynamic system, yields

$$y(t_i) = u(t_i, \tau_\theta) + \varepsilon_i \qquad with \; \varepsilon_i \sim N\left(0, {\lambda_i}^2\right), \qquad i = 1, \dots, n. \tag{4.2}$$

where $y(t_i)$ is the noisy measurement at time t_i, $u(t_i, \tau_\theta)$ is model response at time t_i with time constant τ_θ, and the displacement jitter, ε_i, is assumed to follow a normal distribution with standard deviation λ_i. Using the model in Equation (4.1), the time constant τ can be estimated by fitting the measured displacement with least square method (LSM). Since both $U(t)$ and U_{ss} are proportional to the magnitude of ARF, the estimated τ is considered as a "force-free" parameter, i.e., it is independent of the ARF magnitude which is generally unknown. [55] However, it depends on the three dimensional (3D) distribution of ARF. The inverse problem with the SDF model is solved merely based on the measured responses. Factors that also determine the temporal responses, such as boundary conditions, elasticity and distribution of ARF, are not considered in the SDF model. [29]

In ARF induced creep imaging, without considering the model parameter uncertainty, that is, both elasticity and ARF distribution are accurately known, the only source of uncertainty is from the measurement noise. Based on Equation (4.2) and Bayesian estimation, the posterior distribution of τ can be given by [95]

$$p(\tau_\theta|\boldsymbol{y}) \propto \int L(\boldsymbol{y}|\tau_\theta, \boldsymbol{\lambda}) p(\tau_\theta) p(\boldsymbol{\lambda})\, d\boldsymbol{\lambda} \tag{4.3}$$

where $p(\tau_\theta|\boldsymbol{y})$ is the posterior probability density of τ at τ_θ, $L(y|\tau_\theta, \boldsymbol{\lambda})$ is the likelihood of obtaining the whole observation for given τ_θ and jitter $\boldsymbol{\lambda}$, $p(\tau_\theta)$ and $p(\boldsymbol{\lambda})$ are the priors. Both τ_θ and $\boldsymbol{\lambda}$ are assumed to have normal priors in this study, and it's straightforward to change to other distribution. As it was mentioned, each λ_i is proportional to the measured displacement and has a base constant value of 1% steady state displacement.

In order to get the posterior distribution of τ, a sampling based method can be implemented based on Equation (4.3) with Markov Chain Monte Carlo (MCMC) method. However, this would require thousands of FE model simulations, which renders it computationally infeasible. The use of a GP metamodel makes the calculation possible.

4.3 Gaussian Process Metamodeling

Gaussian process (GP) metamodel has been developed for inference of the uncertainty distribution of complex computer model outputs based on a limited number of model runs. It provides not only the predicted value but also the prediction uncertainty. Gaussian process assumes that a finite set of the model outputs $\boldsymbol{u} = [u(\boldsymbol{x}_1), \dots u(\boldsymbol{x}_m)]^T$ for input $\boldsymbol{X} = [\boldsymbol{x}_1, \dots \boldsymbol{x}_m]^T$ follows a multivariate Gaussian distribution, [96–98] and it can be described by a mean function $m(\boldsymbol{x})$ and a covariance function $k(\boldsymbol{x}, \boldsymbol{x}')$ with a common choice of form [98–100]

$$m(\boldsymbol{x}) = \boldsymbol{h}(\boldsymbol{x})^T \boldsymbol{\beta} \tag{4.4}$$

$$k(\boldsymbol{x}, \boldsymbol{x}') = \sigma^2 \exp\left(-\frac{1}{2} \sum_{i=1}^{d} \frac{(x_i - x_i')^2}{\omega_i^2} \right) + \sigma_\epsilon^2 \delta(\boldsymbol{x}, \boldsymbol{x}') \tag{4.5}$$

where $\boldsymbol{h}(\boldsymbol{x})$ is a vector of known functions over $\boldsymbol{x}$, and $\boldsymbol{\beta}$ is the coefficient vector. Here, the GP metamodel is mainly used for interpolation of unknown output in which case the prediction results are not significantly affected by the form of the mean function. Thus, a zero mean function is selected for simplicity, i.e., $m(\boldsymbol{x}) = 0$. In Equation (4.5), d is the dimension of input $\boldsymbol{x}$, $\boldsymbol{\omega} = [\omega_{1,\dots}\omega_d]$ is the length scale vector defined for each dimension, and $\delta(\boldsymbol{x}, \boldsymbol{x}')$ is the Kronecker delta function. The elements of set $\{\sigma, \boldsymbol{\omega}, \sigma_\epsilon\}$ are called hyperparameters of the GP, and their determination will be discussed in next section. In the last term, σ_ε has a small value to account for numerical fluctuations and stabilize matrix computations of the covariance matrix. [100] Each element of the covariance matrix $\boldsymbol{C}$ (an $m \times m\ matrix$) of the multivariate Gaussian can be calculated with Equation (4.5). Then, the GP definition gives

$$\boldsymbol{u}|\sigma, \boldsymbol{\omega}, \sigma_\epsilon \sim N(\boldsymbol{0}_m, \boldsymbol{C}) \qquad with\ \boldsymbol{C}_{ij} = k(\boldsymbol{x}_i, \boldsymbol{x}_j) \tag{4.6}$$

$$\boldsymbol{C} = \begin{bmatrix} k(\boldsymbol{x}_1, \boldsymbol{x}_1) & k(\boldsymbol{x}_1, \boldsymbol{x}_2) & \dots & k(\boldsymbol{x}_1, \boldsymbol{x}_m) \\ k(\boldsymbol{x}_2, \boldsymbol{x}_1) & k(\boldsymbol{x}_2, \boldsymbol{x}_2) & \dots & k(\boldsymbol{x}_2, \boldsymbol{x}_m) \\ & & \dots & \\ k(\boldsymbol{x}_m, \boldsymbol{x}_1) & k(\boldsymbol{x}_m, \boldsymbol{x}_2) & \dots & k(\boldsymbol{x}_m, \boldsymbol{x}_m) \end{bmatrix} \tag{4.7}$$

To make a Bayesian inference of the posterior distribution for a new input $\boldsymbol{x}_*$, it should be calculated based on the known output $\boldsymbol{u}$ and hyperparameters**,** which yields the mean and variance of the new output $u(\boldsymbol{x}_*)$ [97,99,100]

$$E[u(\boldsymbol{x}_*)|\boldsymbol{u}, \sigma, \boldsymbol{\omega}, \sigma_\epsilon] = \boldsymbol{C}_*^T \boldsymbol{C}^{-1} \boldsymbol{u} \tag{4.8}$$

$$Var[u(\boldsymbol{x}_*)|\boldsymbol{u}, \sigma, \boldsymbol{\omega}, \sigma_\epsilon] = \boldsymbol{C}_{**} - \boldsymbol{C}_*^T \boldsymbol{C}^{-1} \boldsymbol{C}_* \tag{4.9}$$

$$\boldsymbol{C}_* = [\, k(\boldsymbol{x}_*, \boldsymbol{x}_1) \quad k(\boldsymbol{x}_*, \boldsymbol{x}_2) \ \ldots \quad k(\boldsymbol{x}_*, \boldsymbol{x}_m)] \tag{4.10}$$

$$\boldsymbol{C}_{**} = k(\boldsymbol{x}_*, \boldsymbol{x}_*) \tag{4.11}$$

where $\boldsymbol{C}_*$ is the element-wise covariance between $\boldsymbol{x}_*$ and $\boldsymbol{X}$, and $\boldsymbol{C}_{**}$ is the covariance of $\boldsymbol{x}_*$ with itself. Then, the GP metamodel can be combined with Bayesian estimation to improve computational efficiency.

4.4 Bayesian Estimation with Gaussian Process Metamodeling

GP metamodel provides not only a prediction mean of the inferred output but also the variance of the inference which results from the code uncertainty due to a limited number of complex model runs. Then, in Bayesian model parameter estimation; there are three sources of uncertainty to be accounted in the analysis: measurement noise, code uncertainty, and model parameter uncertainty.

At this point, there are two sets of data: the noisy measurement $\boldsymbol{y}$ (SFE model output plus noise) and the model output $\boldsymbol{u}$ (CFE model output). Considering the problem

in Section 4.2, it can be augmented that the input of $y(t)$ to $\boldsymbol{x}$ by adding τ_θ at each input, and thus expressing the input as $\boldsymbol{x} = (t, \tau_\theta)$. Then $\boldsymbol{u}$ and $\boldsymbol{y}$ have the same input domain, and the GP definition gives

$$\begin{pmatrix}\boldsymbol{u}\\ \boldsymbol{y}\end{pmatrix} | \sigma, \boldsymbol{\omega}, \sigma_\epsilon, \tau_\theta \sim N(\mathbf{0}_{m+n}, \boldsymbol{V}(\tau_\theta)) \tag{4.12}$$

where

$$\boldsymbol{V}(\tau_\theta, \boldsymbol{\lambda}) = \begin{bmatrix} \boldsymbol{C}_{uu} & \boldsymbol{C}_{uy}(\tau_\theta) \\ \boldsymbol{C}_{uy}(\tau_\theta)^T & \boldsymbol{C}_{yy}(\tau_\theta) + \boldsymbol{\lambda} I_n \end{bmatrix} \tag{4.13}$$

where $\boldsymbol{C}_{uu}$ is covariance for $\boldsymbol{u}$, $\boldsymbol{C}_{yy}(\tau_\theta)$ is covariance for $\boldsymbol{y}$, and $\boldsymbol{C}_{uy}(\tau_\theta)$ is covariance between $\boldsymbol{u}$ and $\boldsymbol{y}$, which are all calculated with Equation (4.5). [89] For a multivariate normal distribution given in Equation (4.14), the density at arbitrary $\boldsymbol{X}$ can be calculated with Equation (4.15), which are [95]

$$\boldsymbol{X} \sim N(\boldsymbol{\mu}, \boldsymbol{V}) \tag{4.14}$$

$$p(\boldsymbol{X}) = (2\pi)^{-k/2} |\boldsymbol{V}|^{-1/2} \exp\left[-\frac{1}{2}(\boldsymbol{X} - \boldsymbol{\mu})^T \boldsymbol{V}^{-1} (\boldsymbol{X} - \boldsymbol{\mu})\right] \tag{4.15}$$

where *k* is the dimension of $\boldsymbol{X}$. Then, according to Bayes' theorem described in Equation (4.3), the posterior distribution of the parameters is proportional to the likelihood times their priors, which yields

$$p(\tau_\theta, \sigma, \boldsymbol{\omega}, \sigma_\epsilon, \boldsymbol{\lambda}|\boldsymbol{y}, \boldsymbol{u})$$
$$\propto |\boldsymbol{V}(\tau_\theta, \boldsymbol{\lambda})|^{-1/2} exp\,[-\frac{1}{2}\begin{pmatrix}\boldsymbol{u}\\ \boldsymbol{y}\end{pmatrix}^T \boldsymbol{V}(\tau_\theta, \boldsymbol{\lambda})^{-1}\begin{pmatrix}\boldsymbol{u}\\ \boldsymbol{y}\end{pmatrix}] p(\tau_\theta) p(\boldsymbol{\lambda}) p(\sigma, \boldsymbol{\omega}, \sigma_\epsilon) \tag{4.16}$$

In order to get the posterior distribution for the model parameter, i.e., $p(\tau_\theta|\boldsymbol{y}, \boldsymbol{u})$ with a full Bayesian analysis, it needs to marginalize out the hyperparameters $\{\sigma, \boldsymbol{\omega}, \sigma_\epsilon\}$ and the measurement noise, $\boldsymbol{\lambda}$. However, this formulation is computationally expensive and it is not easy to choose appropriate priors for these parameters. Following the idea of modular Bayesian approach, [89] plausible point estimates for the hyperparameters to replace the probability distribution in Equation (4.16) can be calculated. This approximation has been shown to provide similar results as the full integration. In addition, for similar reasons, the modular Bayesian approach proposes to derive the hyperparameters with only the model output $\boldsymbol{u}$ instead of $(\boldsymbol{u}^T, \boldsymbol{y}^T)^T$ which involves integration over the prior distribution of τ_θ. Then, the hyperparameters are calculated by maximizing the log marginal likelihood for data $\boldsymbol{u}$, which is

$$\log p(\boldsymbol{u}|\sigma, \boldsymbol{\omega}, \sigma_\epsilon) = -\frac{1}{2}\log|\boldsymbol{C}| - \frac{1}{2}\boldsymbol{u}^T\boldsymbol{C}^{-1}\boldsymbol{u} - \frac{m}{2}\log 2\pi \tag{4.17}$$

The covariance matrix $\boldsymbol{C}$ is defined by Equations (4.5) and (4.7), and is dependent on the hyperparameters $\{\sigma, \boldsymbol{\omega}, \sigma_\epsilon\}$. The partial derivatives of the above log marginal likelihood can be evaluated by

$$\frac{\partial}{\partial\sigma}\log p(\boldsymbol{u}|\sigma, \boldsymbol{\omega}, \sigma_\epsilon) = \frac{1}{2} tr((\boldsymbol{C}^{-1}\boldsymbol{u}\boldsymbol{u}^T\boldsymbol{C}^{-T} - \boldsymbol{C}^{-1})\frac{\partial \boldsymbol{C}}{\partial\sigma}) \tag{4.18}$$

$$\frac{\partial}{\partial \boldsymbol{\omega}} \log p(\boldsymbol{u}|\sigma, \boldsymbol{\omega}, \sigma_\epsilon) = \frac{1}{2} tr((\boldsymbol{C}^{-1}\boldsymbol{u}\boldsymbol{u}^T\boldsymbol{C}^{-T} - \boldsymbol{C}^{-1})\frac{\partial \boldsymbol{C}}{\partial \boldsymbol{\omega}}) \tag{4.19}$$

$$\frac{\partial}{\partial \sigma_\epsilon} \log p(\boldsymbol{u}|\sigma, \boldsymbol{\omega}, \sigma_\epsilon) = \frac{1}{2} tr((\boldsymbol{C}^{-1}\boldsymbol{u}\boldsymbol{u}^T\boldsymbol{C}^{-T} - \boldsymbol{C}^{-1})\frac{\partial \boldsymbol{C}}{\partial \sigma_\epsilon}) \tag{4.20}$$

Then the hyperparameters can be solved with conjugate gradients optimization routine based on Equations (18)-(20). This process is also called the training of GP metamodel, i.e., the hyperparameters in Equations (4.4) and (4.5) are determined in the light of the data. [99]

Another source of uncertainty is the model parameter uncertainty. In modular Bayesian approach, it is proposed to consider these parameters unknown, which will increase the flexibility of the model and make better fitting and prediction. However, if we want to utilize the model parameter information that is discarded in the SDF model estimation, these parameters over theirs prior distributions should be marginalized out. Now, the input $\boldsymbol{x}$ is augmented to $(t, \tau_\theta, \boldsymbol{\varphi})$, where $\boldsymbol{\varphi}$ is the vector of model parameters. Then, posterior distribution of τ_θ is obtained

$$p(\tau_\theta|\boldsymbol{y}, \boldsymbol{u})$$
$$\propto \iint |\boldsymbol{V}(\tau_\theta, \boldsymbol{\lambda}, \boldsymbol{\varphi})|^{-1/2} exp\left[-\frac{1}{2}\begin{pmatrix}\boldsymbol{u}\\ \boldsymbol{y}\end{pmatrix}^T \boldsymbol{V}(\tau_\theta, \boldsymbol{\lambda}, \boldsymbol{\varphi})^{-1}\begin{pmatrix}\boldsymbol{u}\\ \boldsymbol{y}\end{pmatrix}\right] p(\tau_\theta)p(\boldsymbol{\varphi})p(\boldsymbol{\lambda})d\boldsymbol{\lambda}d\boldsymbol{\varphi} \tag{4.21}$$

Summary for the development of Equation (4.21) is illustrated in Fig. 4.2.

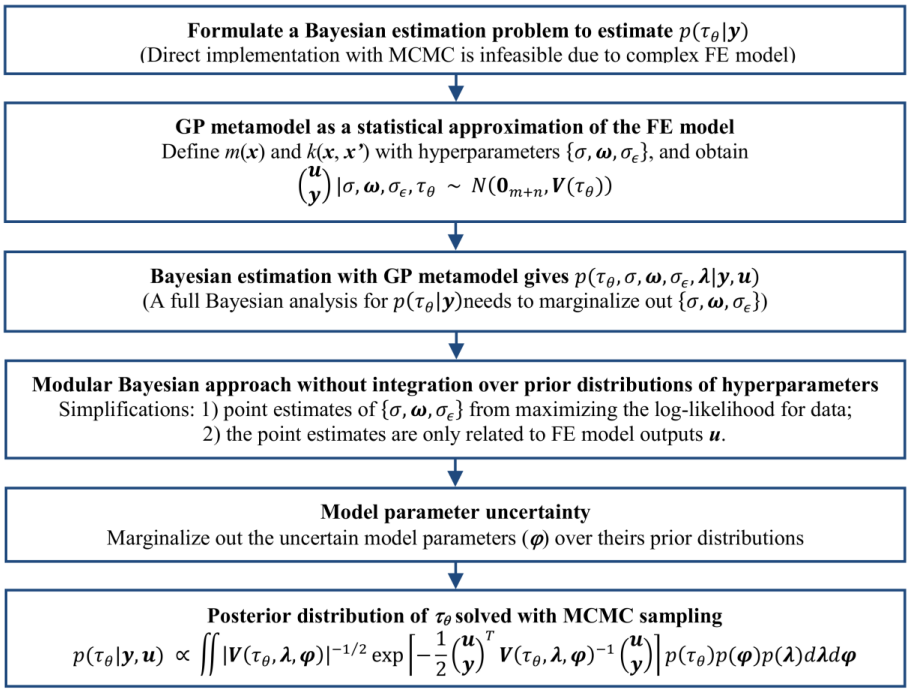

Figure 4.2. Flowchart of Bayesian estimation with GP metamodel.

Equation (4.21) can only provide a relative value for the probability density of τ_θ. In order to get the absolute value, a constant coefficient P_o should be solved by plugging the right hand side of Equation (4.21) into Equation (4.22).

$$\int p(\tau_\theta|\boldsymbol{y},\boldsymbol{u})\, d\,\tau_\theta = 1 \tag{4.22}$$

However, it is intractable to solve this integral analytically. To obtain the posterior distribution that is defined by Equation (4.21), a Markov Chain Monte Carlo (MCMC) method is generally used in such a Bayesian inference problem as a sampling based numerical approximation. [97,101,102] In this study, MCMC sampling with Metropolis–Hastings algorithm is implemented to calculate the posterior distribution of τ_θ. [102,103] The key idea for the MCMC method is to build a Markov chain that converges to the proposed stationary distribution. To this end, Metropolis–Hastings algorithm generates a random walk by accepting the proposed new state ${\tau_\theta}^{t+1}$ with probability [103–105]

$$\min\left(1,\frac{p({\tau_\theta}^{t+1}|\boldsymbol{y},\boldsymbol{u})}{p({\tau_\theta}^{t}|\boldsymbol{y},\boldsymbol{u})}\frac{Q({\tau_\theta}^{t}|{\tau_\theta}^{t+1})}{Q({\tau_\theta}^{t+1}|{\tau_\theta}^{t})}\right) \tag{4.23}$$

where $Q({\tau_\theta}^{t}|{\tau_\theta}^{t+1})$ is the proposal distribution that generates the new state ${\tau_\theta}^{t+1}$ based on current state ${\tau_\theta}^{t}$. Q is required to be symmetric, i.e. $Q({\tau_\theta}^{t}|{\tau_\theta}^{t+1}) = Q({\tau_\theta}^{t+1}|{\tau_\theta}^{t})$. A Gaussian distribution satisfied this requirement and is a popular choice, [103,104] then Q can be formulated as

$$Q(y|x) = \frac{1}{\sigma\sqrt{2\pi}}e^{-\frac{(x-y)^2}{2\sigma^2}} \tag{4.24}$$

Then Equation (4.23) can be simplified as

$$\min\left(1, \frac{p(\tau_\theta{}^{t+1}|\boldsymbol{y}, \boldsymbol{u})}{p(\tau_\theta{}^{t}|\boldsymbol{y}, \boldsymbol{u})}\right) \tag{4.25}$$

Equation (4.24) shows that the algorithm tends to visit the point that is close to current state. If the new state results in a higher probability density, then it will be accepted as the current state in next iteration. If the new state produces a small probability density, it still can be accepted with probability provided by Equation (4.25).

A typical MCMC sampling with Metropolis–Hastings algorithm for this study is shown in Fig. 4.1. After a "burn-in" period from the start value 0.1 ms, the algorithm converges to the expected distribution around the true value 0.5 ms. The data points in the "burn-in" period cannot be included in the final sample set that will be used to infer the posterior distribution of the time constant.

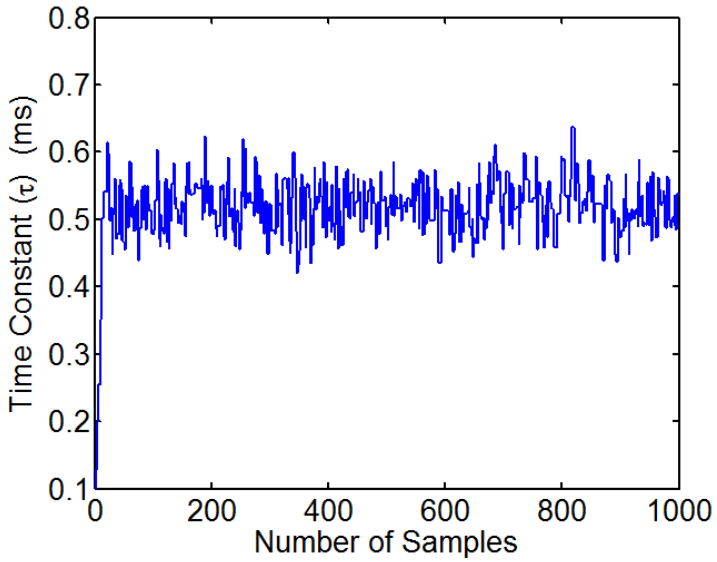

Figure 4.1. A typical MCMC sampling with Metropolis–Hastings algorithm. Start value τ = 0.1 ms and true value τ = 0.5 ms.

Chapter 5: Bayesian Estimation of Soft Tissue Viscoelasticity

The Bayesian approach with the FE model (BAFEM) to estimate a posterior distribution of time constant in ARF induced creep imaging has been developed in Chapter 4. To solve a this statistical inverse problem in ARF induced creep imaging, different sources of uncertainty in the estimation, including displacement jitter from the measurement, boundary condition, elasticity uncertainty and ARF distribution uncertainty are considered. This chapter investigates the effect of the above sources of uncertainty individually, as well as their combined effect. The cases with soft tissue local heterogeneity are studied with simplified heterogeneous models. Numerical simulation results of the BAFEM are compared with the SDF model estimations. This chapter demonstrates the potential of BAFEM as a new perspective to solve a statistical inverse problem in ARF imaging and provide more accurate and comprehensive estimation of soft tissue viscoelasticity.

5.1 Finite Element Modeling and Implementation

5.1.1 Finite Element Model

The soft tissue is modeled as an isotropic, linear viscoelastic and near-incompressible solid with Poisson's ratio $v = 0.499$. Axisymmetric FE models are built to reduce the computational cost. There are two types of FE models built in this study: synthetic FE (SFE) model and characterization FE (CFE) model, as illustrated in the diagram of Fig. 5.1 (a).

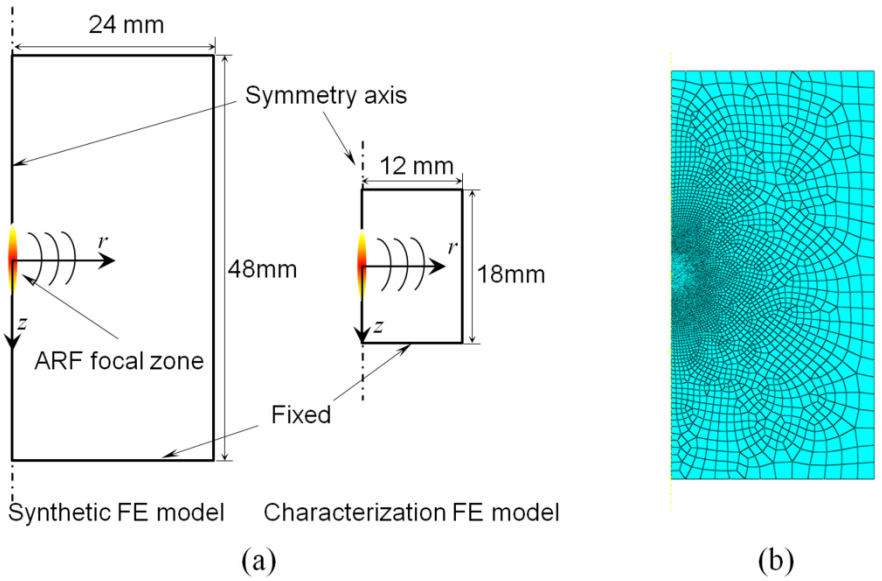

Figure 5.1. (a) Diagrams of Synthetic FE (SFE) model and Characterization FE (CFE) model; (b) FE mesh of SFE model. The SFE model generates numerical experiments data which is in practice measured by ultrasonic tracking methods. The CFE model is the model used in the inverse computation.

The SFE model is developed to generate synthetic displacement data. In practice, many groups have developed ultrasonic tracking methods to measure the displacement of soft tissue induced by ARF. [25,26,106,107] Numerical models have been commonly used to justify the performance of biomechanical inverse algorithms as summarized in [108], because the estimated parameters are able to be compared with the true value, i.e., the value assigned to the numerical models, which is generally unknown in experiments. In addition, it is easy to make a comprehensive parametric analysis with the numerical model. As shown in Fig. 5.1 (b), the SFE model consists of 5,275 elements (5,139 four-node bilinear axisymmetric quadrilateral elements and 136 three-node linear axisymmetric triangular elements) with hybrid formulation that handles the near-incompressible material behavior. The SFE model has been previously validated with the

analytical model solution for the steady state response. [29] In the analysis, it is assumed that the SFE model is the "true model", and performance of the inverse algorithm is evaluated by comparing its estimation with parameter of the SFE model. In ARF imaging, the tissue displacement measured by ultrasonic tracking is subject to jitter and underestimation. [107,109,110] ARF displacement jitter tends to increase with the displacement magnitude, while the percentage of displacement underestimation does not change much with the displacement amplitude. [109] Equation (4.1) shows τ is only related to the relative displacement with respect to the steady state displacement, which means the effect of displacement underestimation is not significant on the estimation of τ; therefore, only jitter for measurement noise is considered, and a simple linear relation between jitter and displacement is assumed.

The CFE model is used in the inverse computation to fit the synthetic data. One advantage of ARF imaging is that the global boundary conditions have little effect on the responses of ROE for a viscoelastic soft tissue. [111] Subsequently, it is easy to build the CFE model pertaining solely to the local boundary conditions. Here, since homogeneity is assumed, it's necessary to assure that the boundary of the CFE model has negligible effect on the responses of ROE, while the dimensions are kept as small as possible to reduce computational cost. The qualified dimensions of the CFE model are mainly decided by a rough estimation of the soft tissue viscoelasticity that determines the shear wave speed and attenuation, [40] and the time interval of interest during which the reflected shear wave should not significantly affect the responses of ROE. The CFE model has only 900 elements, which ensures both the computational efficiency and negligible uncertainty due to the global boundary conditions.

Acoustic radiation force is a 3D spatial-varying body force that is related to the absorption coefficient of the medium, the temporal averaged intensity of the location and the speed of sound in the medium as is discussed in Chapter 2. Intensity I can be estimated from the distribution of acoustic pressure, which can be calculated using Field II or FOCUS ultrasound simulation package based on the properties of the medium, geometry, and center frequency of the transducer. [82,83] However, in practice, absorption coefficient α cannot be accurately known and may be nonuniform. [8] In addition, reflection and nonlinear propagation of ultrasound also make the simulated ARF field inaccurate. In this study, ARF generated by a 3.25 MHz single-element focused transducer (F-number is 0.83) is mimicked by a 3D Gaussian function. The uncertainty of estimated ARF distribution is quantified by the modeled *-6 dB* focal region volume in the CFE model.

In order to estimate the time constant using the CFE model, the elasticity of the material should be known, while its absolute value cannot be estimated in ARF induced creep imaging. Mauldin et al. proposed a method to combine ARF induced creep imaging with shear wave elasticity imaging for elastic parameters estimation. [36] Alternatively, in concert with ROE Time-to-Peak (TTP) technique to quantify elasticity, [43] it's possible to develop a purely ROE-based method without shear wave measurements. This thesis will focus on the estimation of time constant with ARF induced creep imaging, and the elasticity is assumed to be known with uncertainty.

5.1.2 Design and Implementation

Three soft tissue material properties are studied here with shear modulus and time constant combinations (μ, τ): $(1.5kPa, 1.0ms), (3kPa, 0.5ms),$ and $(1.5kPa, 0.5ms)$. They are in the common range of soft tissue viscoelasticity with relatively low viscosity in which case the SDF model has poor performance. [29] For ARF, as is mentioned above, its uncertainty is modeled with the *-6 dB* focal region volume. Its value is scaled as a volume ratio V_θ, and $V_\theta = 1$ means the true value. Then, if there is an estimation of 20% larger than the true value, the input is set to $V_\theta = 1.2$.

For each ARF induced creep responses, 51 displacement data in 10 ms time step are obtained from the SFE model simulation with added noise. This is data $\boldsymbol{y}$ in Equation (4.12). In order to build a good GP metamodel for the CFE model, the set of input points at which the CFE model will run needs to have a good coverage of the input space of $\boldsymbol{x} = (t, \tau_\theta, \boldsymbol{\varphi})$. The values of the unknown τ_θ and uncertain model parameter $\boldsymbol{\varphi}$ are chosen through a Latin hypercube sampling (LHS) that maximizes the minimum distance between points. [112,113] Here, 30 LHS samples to cover the interested space of τ_θ and $\boldsymbol{\varphi}$ are chosen. The interested space for τ_θ can be decided based on the SDF model estimation and its prior, but set to a wide range to include the true value. The interested space for $\boldsymbol{\varphi}$ is decided based on the priors of the uncertain model parameters. Then for each sampled $(\tau_\theta, \boldsymbol{\varphi})$, the CFE model will run and output the displacement, i.e., 51 displacement data in 10 ms time step. If all the CFE model outputs are used to build the GP metamodel, then it has 30×51 points in $\boldsymbol{u}$, which will result in a large dimensional covariance matrix that is generally singular due to the small "distance" between points.

That means it's necessary to select part of the points to form the code output, and large distances between points are desired. A suboptimal but simple procedure is used to choose the points: 1) sort the 30 LHS samples with ascending order of τ_θ, which is the most dominate factor of the response; 2) then merge all the output data to one vector with the same order; 3) choose the points spaced by N_s points, where N_s cannot be a factor of 51. In this way, a good cover of the time input is guaranteed; meanwhile, successive parameter LHS samples do not have the same time input.

5.2 Characterization without Finite Element Model Parameters Uncertainty

In order to solve the inverse problem in ARF imaging with BAFEM, a finite element model of soft tissue needs to be built first. As it is mentioned in last section, this is the CFE model which is used in the inverse procedure. Since the ARF induced motion is highly localized, it is not necessary to build the CFE model with the exact global boundary conditions. It is desirable to reduce its complexity and dimension, at the same time, the CFE model should bring negligible uncertainty as an approximation of the true model. As is demonstrated in Fig. 5.2 comparison between responses of the SFE model and the CFE model illustrate good agreement (0.5% maximum deviation) for the soft material that is highlighted in this study, i.e., $\mu = 3kPa$. It also should be valid for material with similar or smaller shear modulus, but not for material with much larger shear modulus, i.e., $\mu = 15kPa$ in Fig. 5.2, due to a larger shear wave speed. If the inverse process is based on the response of the early stage (e.g., before 3ms), then this CFE model is also acceptable for $\mu = 15kPa$. That is, both the material property and the

interested time interval determine the CFE model dimension, which allows an inverse process without considering the uncertainty due to the model boundary conditions.

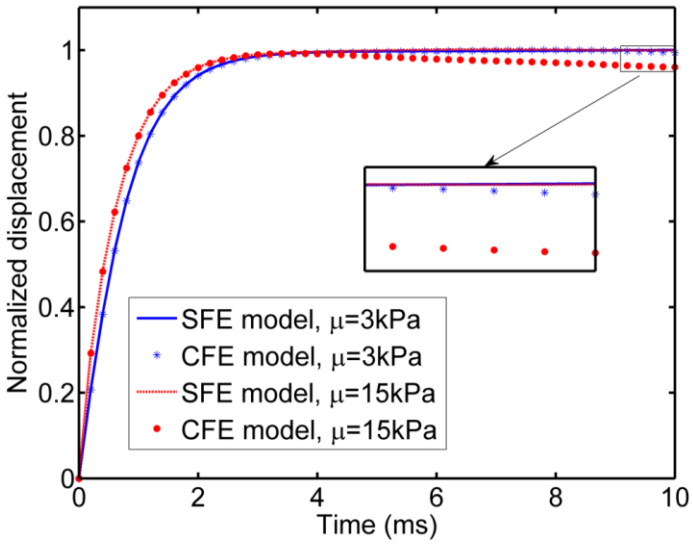

Figure 5.2. Comparison between responses of the SFE model and CFE model. All cases have the time constant 0.5ms.

Before applying the GP metamodel to BAFEM, its prediction accuracy is tested. The GP metamodel is trained with the CFE model output $\boldsymbol{u}$. The three materials in Fig. 5.3 are not included in the design points as described in Section 5.1, but they are within the interval to generate the design points with Latin hypercube sampling (LHS). The 95% confidence interval of the prediction is quite narrow, which indicates the GP metamodel brings small code uncertainty to the estimation. Then, if one wants to infer the output for a new material, the GP metamodel can be used to do the calculation instead of the computationally expensive CFE model.

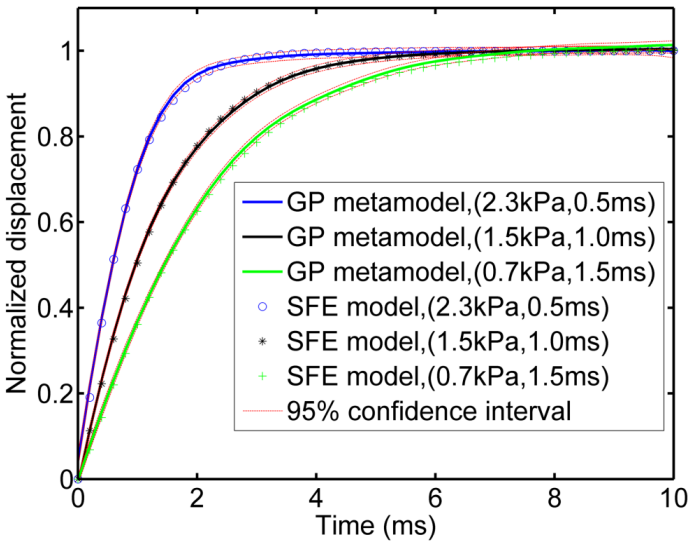

Figure 5.3. Validation of the GP metamodel for three viscoelastic materials (μ,τ). The three materials are not included in the design points, but within the interval to generate the LHS design points.

The simplest case with no model parameter uncertainty and known displacement jitter level is investigated first. The only source of uncertainty is the jitter of the displacement. It is assumed that the jitter has zero mean and standard deviation (SD) consisting of a constant part λ_c, and a displacement-dependent part λ_d, i.e., the jitter SD is $\lambda_c + \lambda_d$. The constant part is set to 1% of the steady state displacement, and the displacement-dependent part is set to 5% of the measured displacement, which is the similar level to the reported relation between jitter and maximum displacement. [109] Other forms of jitter due to different experimental setting and ultrasound tracking method can also be considered with this inverse procedure. Figure 5.4 shows the posterior distribution for both Bayesian approach with the FE model (BAFEM) and Bayesian approach with the SDF (BASDF). Since the SDF model is simple in computation, the BASDF does not need to use the GP metamodel as required for the BAFEM. Each

posterior distribution is calculated with 1000 MCMC samples, and its density is approximated with kernel smoothing bandwidth determined with Silverman's rule of thumb. [114] The results are compared with the true value and least square method with SDF (LSMSDF) estimation without noise added. The true value is the value that is set to the SFE model to generate the numerical experiment data. For all three materials, the BAFEM posterior distributed around the true value with a small SD, while the BASDF posterior is biased. As it is discussed above, this is due to the inadequacy of the SDF models, which are not able to model the three-dimensional true system. For LSMSDF, even without jitter, the estimation is highly biased in Fig. 5.4.

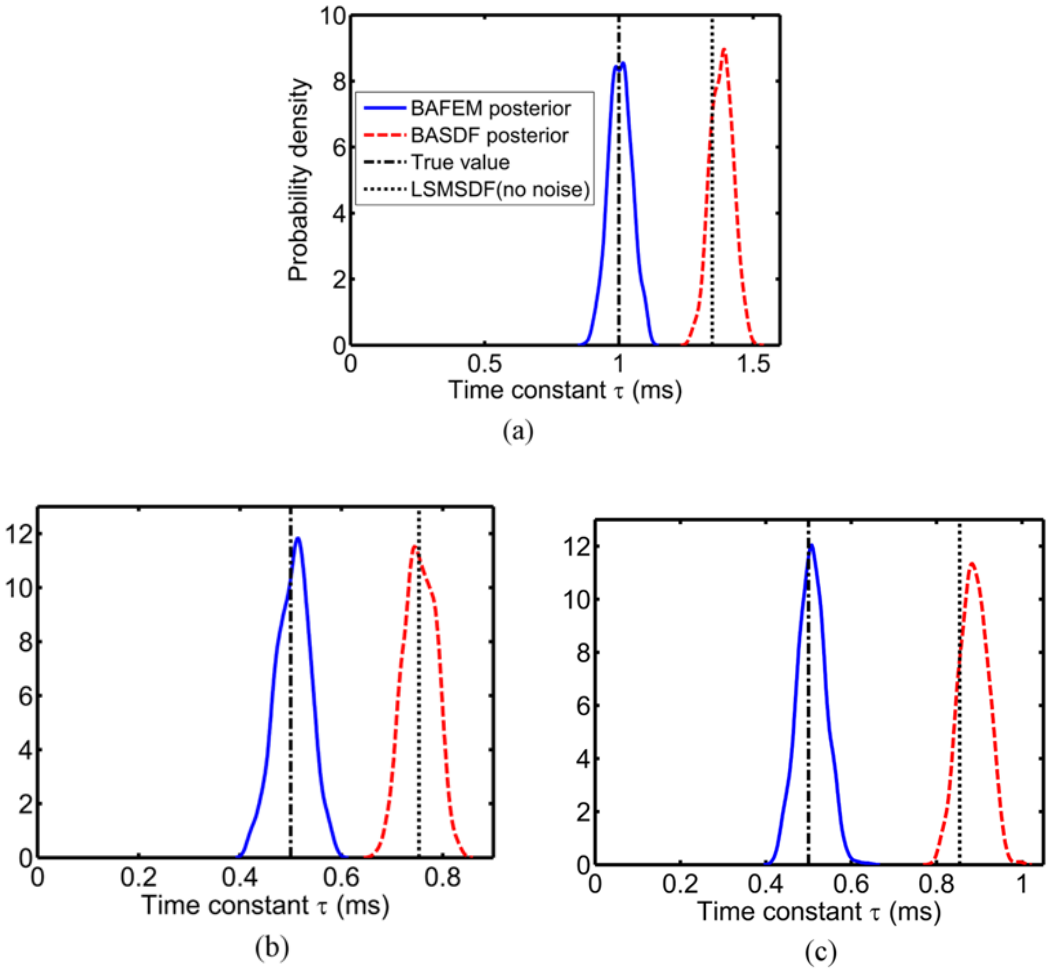

Figure 5.4. Posterior distribution of time constant for Bayesian approach with FE model (BAFEM) and Bayesian approach with SDF (BASDF). The results are compared with the true value and least square method estimation with the SDF. Three soft tissue material properties are studied with (μ,τ): (a) (1.5kPa,1.0ms), (b) (3kPa,0.5ms), and (c) (1.5kPa,0.5ms).

One issue in the inverse computation is to set a good prior for the time constant τ_θ. In this study, a normally distributed prior with the LSMSDF estimation as its mean is employed for τ_θ. This mean value is generally biased compared to the true value. As it is noted in Fig. 5.5, being too confident (with a small SD) on this mean value may lead to a biased posterior distribution, since the prior value is a dominant factor in the

estimation. Generally, accurate prior knowledge of τ_θ is absent. In such a case, a larger SD of τ_θ is preferred in order to have a good coverage of the true value, and Bayesian estimation can update the prior with data to converge to the true value as it is shown in Fig. 5.5.

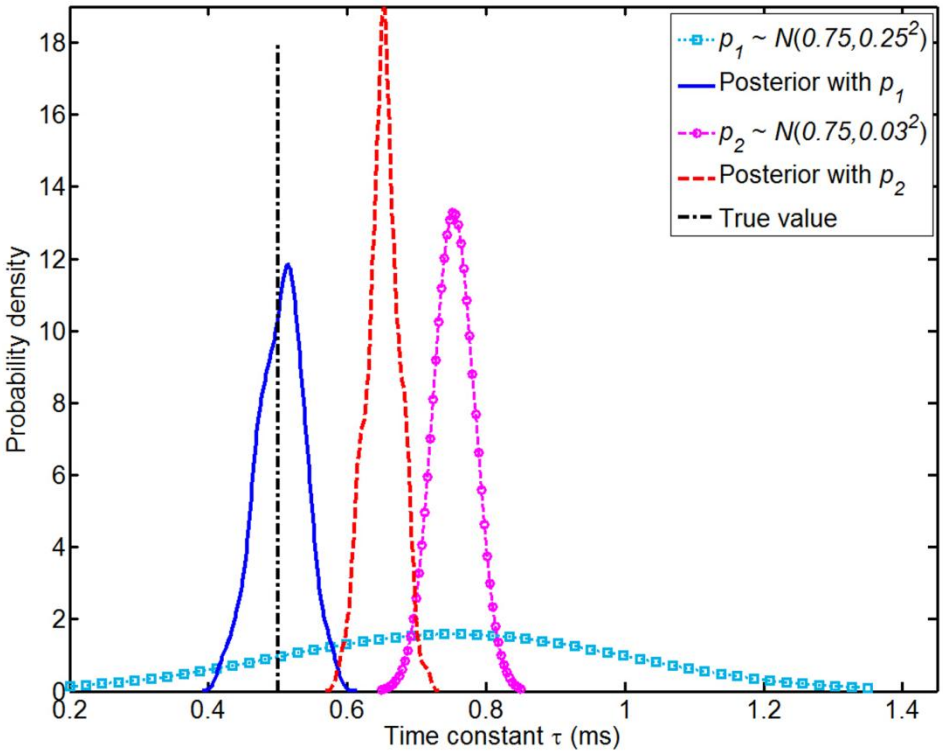

Figure 5.5. Effects of prior distribution on the predicted posterior for time constant. Both priors' mean are biased from the true value. p_2 has a much smaller SD than p_1. The true soft tissue material property is $\mu_T = 3kPa, \tau_T = 0.5ms$.

In practice, the displacement jitter level in ARF imaging also cannot be accurately obtained. One may estimate it from the experiment setting with uncertainty, and then integrate over its distribution as in Equation (4.3). In Table 5.1, the true displacement-dependent jitter level used to generate the measurement $\boldsymbol{y}$ is 5% of the measured displacement at each time, while when using BAFEM, the true jitter level is unknown. It

is reasonable to estimate a jitter level with uncertainty based on the imaging system configuration, [109] which means the jitter level is also a probability distribution. In modular Bayesian approach, Kennedy and O'Hagan proposed to calculate a plausible estimate of the measurement noise level from data. Then, they used the plausible value instead of its distribution in the inference. [89] However, the process to calculate this value needs to integrate over the prior distribution of all the model parameters and it's still an approximation due to the inaccurate prior information. In this study, the results with both distribution and point value are compared and recorded in Table 5.1. They all give consistent estimations on the mean value, nonetheless the predicted posterior SDs with distributed values are more consistent than that with the point values. It is a reasonable choice to use the distributed value of jitter level, and it will not bias the predicted mean or increase the SD.

Table 5.1. Effects of prior jitter level estimation on the predicted posterior of τ_θ (ms). The true value of λ_d is 5.0%. The true value of τ_θ is 0.5ms.

Displacement-dependent jitter level, λ_d	Distribution, $N(\lambda_d, 0.25^2\lambda_d^2)$		Point value (λ_d)	
	Posterior mean	Posterior SD	Posterior mean	Posterior SD
2.5%	0.50	0.028	0.50	0.024
5.0%	0.51	0.033	0.51	0.033
10%	0.50	0.027	0.52	0.060

5.3 Characterization with Finite Element Model Parameter Uncertainty

Before integrating all the sources of uncertainty together, the effect of uncertain shear modulus and ARF volume are first considered individually, while the displacement jitters are still included. A truncated normal distribution bounded by ±2SD around mean is considered. Of course, other forms of distribution can also be used based on our prior knowledge of the parameter. An 8-point Legendre-Gauss quadrature (LGQ) is employed to evaluate the integration in Equation (4.21). In Fig. 5.6, its accuracy is validated with a "Brute force" integration based on Trapezoidal Rule with 200 subintervals. For both the biased and unbiased mean, both the 8-point and 12-point LGQ provides accurate evaluation of the log-likelihood, while the 4-point LGQ results are not accurate enough. For computational efficiency, the 8-point LGQ is used in the implementation.

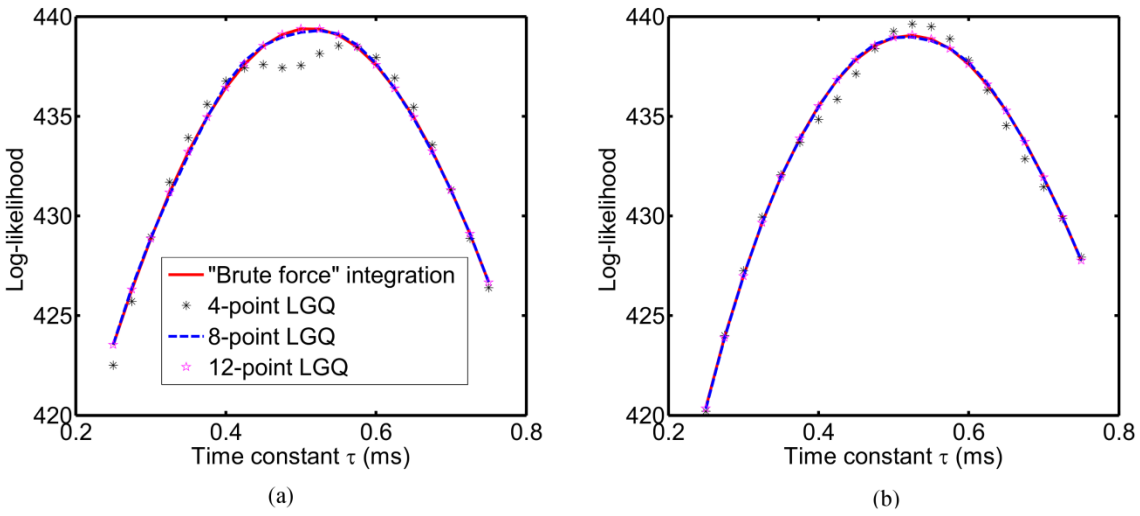

Figure 5.6. Log-likelihood for different τ values with different integration methods over the uncertain μ_θ distribution. The true soft tissue material property is $\mu_T = 3kPa, \tau_T = 0.5ms$. The uncertain μ_θ has distribution: (a) $\mu_\theta \sim N(\mu_T, (0.3\mu_T)^2)$, and (b) $\mu_\theta \sim N(1.3\mu_T, (0.3\mu_T)^2)$.

Figure 5.7 (a) shows the case with elasticity uncertainty but no ARF distribution uncertainty. For the unbiased mean cases, the shear modulus distribution with a smaller SD results in a predicted posterior with a smaller SD as expected. A $0.03\mu_T$ SD means that the prior information on shear modulus is very accurate compared to the one with $0.3\mu_T$ SD. In this case, the predicted posterior mean±SD is 0.51±0.035ms which is close to the case with no elasticity uncertainty as in Table 5.1. The predicted posterior with $0.3\mu_T$ SD is 0.51±0.048 ms, which does not increase the prediction SD significantly. Even the biased mean with $0.3\mu_T$ SD, a good prediction 0.52±0.047ms can still be obtained. This is because when both the elasticity and the time constant near the true values, they produce a much higher likelihood value which is more significant than the prior distribution value of the elasticity. However, if a biased mean with small SD is used

for the elasticity distribution, i.e., we are too confident on some inaccurate value, the predicted mean will be biased, i.e., 0.58±0.036ms for the fourth case in Fig. 5.7 (a). It also indicates that an overestimated shear modulus results in an overestimated time constant. But for similar case in Fig. 5.7(b), it shows an overestimated ARF volume results in an underestimated time constant. In addition, the unbiased mean of ARF volume with larger uncertainty leads to a biased posterior mean (the solid blue line), which means the underestimated part of ARF volume plays a more important role and leads to an overestimation of the predicted mean.

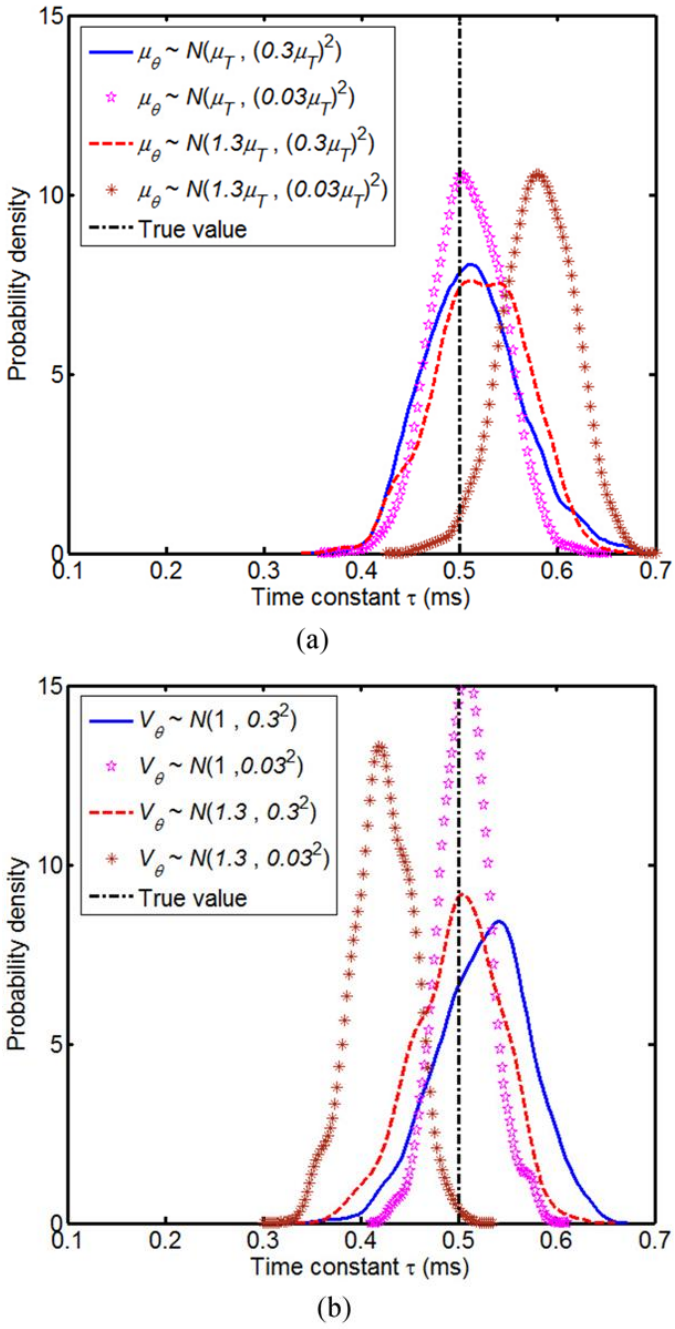

Figure 5.7. Posterior prediction for time constant with uncertain (a) elasticity and (b) ARF distribution. The true soft tissue material property is $\mu_T = 3kPa, \tau_T = 0.5ms$.

In ARF imaging, all sources of uncertainty will be present in the imaging process and they need to be integrated together to evaluate the performance of the BAFEM. In

Table 5.2, different uncertainty combinations and the corresponding posterior prediction for the time constant are listed. For each estimation of the time constant, 1000 MCMC samples are generated based on Equation (4.21), which can be done within an hour with Matlab code running on a PC. All BAFEM predictions have better estimation than the BASDF method. There is no model parameter uncertainty for BASDF in Table 5.2, since the SDF model cannot integrate this information into the computational procedure.

Table 5.2. Posterior prediction for τ (ms) with different model parameter uncertainty. The true soft tissue material property is $\mu_T = 3kPa, \tau_T = 0.5ms$.

	Model parameter distribution		Posterior prediction for τ (ms)	
	μ_θ	V_θ	mean	SD
Case 1	$N(\mu_T, (0.3\mu_T)^2)$	$N(1, 0.3^2)$	0.53	0.059
Case 2	$N(1.3\mu_T, (0.3\mu_T)^2)$	$N(1.3, 0.3^2)$	0.55	0.052
Case 3	$N(0.7\mu_T, (0.3\mu_T)^2)$	$N(1.3, 0.3^2)$	0.48	0.052
Case 4	$N(1.3\mu_T, (0.3\mu_T)^2)$	$N(0.7, 0.3^2)$	0.57	0.053
Case 5	$N(0.7\mu_T, (0.3\mu_T)^2)$	$N(0.7, 0.3^2)$	0.51	0.056
BASDF	-	-	0.75	0.03

Among all cases, Case 4 results in the worst estimation because both parameter distributions tend to overestimate the predicted mean as is discussed in last paragraph. Case 5 leads to the best prediction due to the fact that the two distributions induced bias is canceled out. All these cases indicate that the BAFEM can improve the prediction of time constant in the presence of displacement jitter and large model parameter uncertainty. Figure 5.8 illustrates that the BAFEM can be improved if we can reduce the displacement jitter level or have more accurate prior model parameter information. The

details of the mean and SD predictions are listed in Table 5.3. However, for BASDF, even with a reduced displacement jitter level, the estimated time constant is still highly biased due to the limitation of the SDF model that cannot represent the true three-dimensional dynamic system of the ARF induced motion.

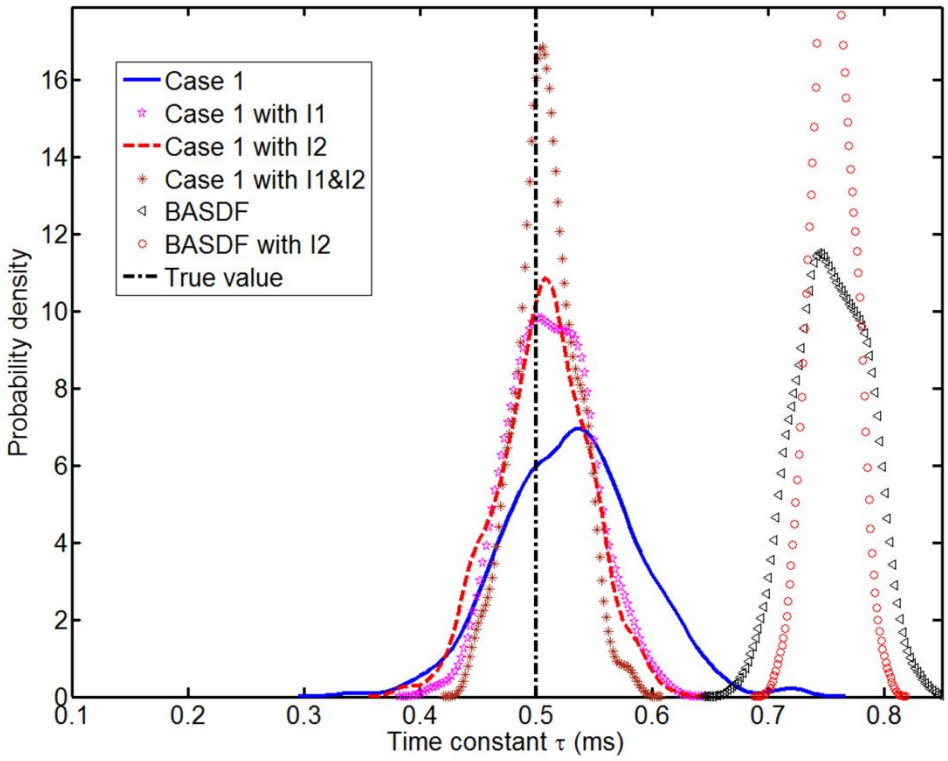

Figure 5.8. Posterior prediction for time constant with improved displacement data or prior information. The two improvements are: I1) reduced model parameter uncertainty with SD $0.1\mu_T$ for μ_θ and 0.1 for V_θ; I2) reduced displacement-dependent jitter level 2%. Case 1 is described in Table 5.2.

Table 5.3. Posterior prediction for τ (ms) with improvements in Fig. 5.8. The true soft tissue material property is $\mu_T = 3kPa, \tau_T = 0.5ms$.

	Posterior prediction for τ (ms)	
	mean	SD
Case 1	0.53	0.059
Case 1 with I1	0.51	0.036
Case 1 with I2	0.51	0.039
Case 1 with I1&I2	0.51	0.026
BASDF with I2	0.76	0.017

5.4 Characterization with Soft Tissue Heterogeneity

In ARF imaging, a quantitative imaging of soft tissue mechanical property becomes challenging in the presence of local heterogeneity. In shear wave imaging, the quantitative imaging quality can be highly reduced by the local boundary due to reflection, which, sometimes, leads to a poor spatial resolution that can be lower than a qualitative imaging method within the ROE. [37] In ARF imaging within the ROE, the dynamic responses of soft tissue are also altered by the local heterogeneity as is discussed in Section 3.3.4. In this section, the BAFEM inverse procedure is applied to estimate the time constant in the presence of local heterogeneity. Generally, in ARF imaging, a simplified model to mimic soft tissue heterogeneity would be a spherical tumorous inclusion inside normal soft tissue, and it is assumed that both the inclusion and background tissues are homogeneous. [44,61,115,116] In addition, a fully bonded interface is generally assumed, i.e., both displacement and stress are assumed to be continuous.

In order to build the FE model of the soft tissue with inclusion, the profile of the inclusion should be known beforehand, which can be realized by profile extraction in practice. [117] However, the profile of the inclusion boundary cannot be accurately obtained, or, it is possible that there is no actual boundary but region with large gradient of mechanical properties. In such a case, the uncertainty due to the inclusion profile should be considered. As is shown in Fig. 5.9, the inclusion diameter *d* is known with uncertainty in the characterization FE (CFE) model, which will be modeled as a prior distribution.

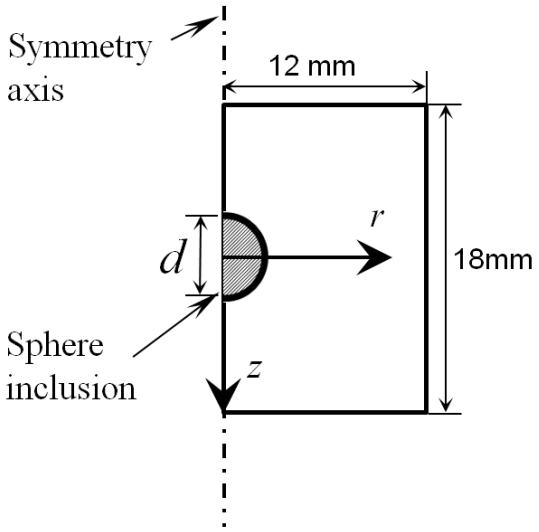

Figure 5.9. Diagram of the characterization FE (CFE) model with spherical inclusion of diameter *d*.

As is shown in Fig 5.10, even though the mechanical properties for both inclusions are the same, the temporal responses vary due to different local boundary conditions, which show that it's necessary to model the local boundary in order to obtain an accurate quantitative estimation.

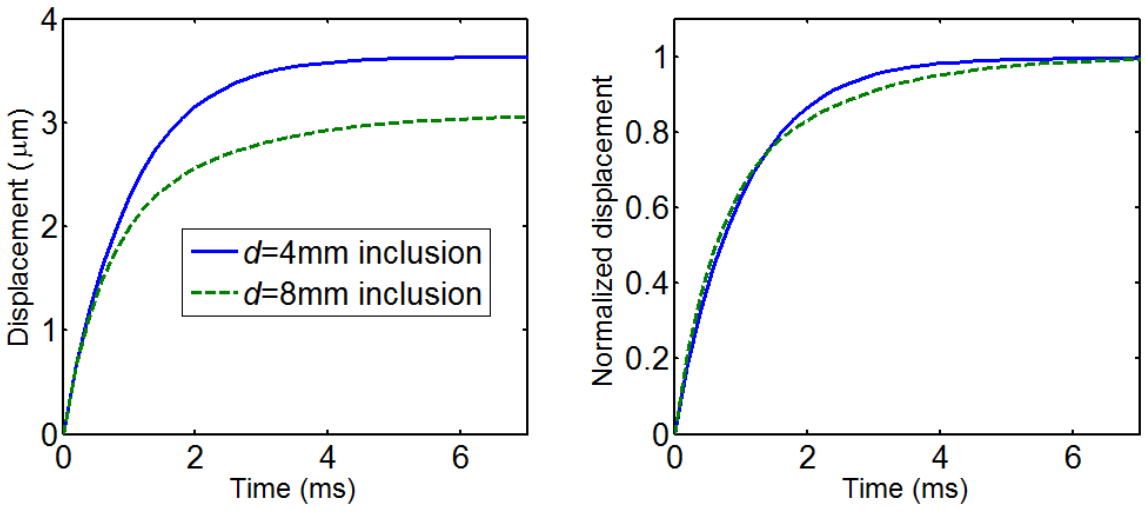

(a) (b)

Figure 5.10. Creep displacement responses inside the spherical inclusion. (a) is the original responses, and (b) is the normalized responses. τ=0.5ms for both the background and inclusion. Background shear modulus μ_B = 3kPa, and inclusion shear modulus μ_I = 9kPa.

In this thesis, two spherical inclusions are modeled: d = 4mm and d = 8mm that will be set in the Sythetic FE (SFE) model as the true value. In the inverse characterization process, the diameter d is known with uncertainty and assigned to the CFE model. The shear moduli of the background and inclusion are set to be μ_B = 3kPa and μ_I = 9kPa, respectively. The background and inclusion are assumed to have the same time constant, τ=0.5ms. In the characterization process, the inclusion time constant is unknown and needs to be inversely solved based on the creep displacement responses inside the inclusion.

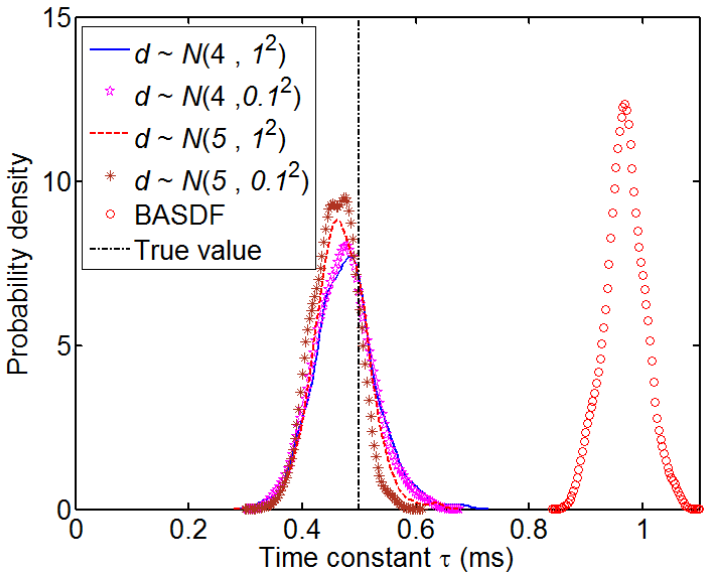

(a)

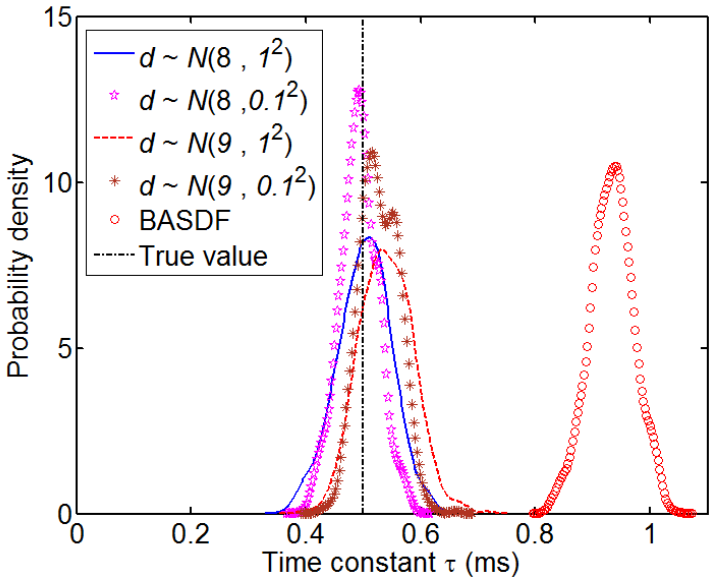

(b)

Figure 5.11. Posterior distribution of time constant for model with spherical inclusion of diameter (a) 4mm and (b) 8mm. Uncertin estimations of prior diameter, *d* (mm), are studied with different distribution. The Bayesian approach with SDF (BASDF) is also presented as a comparison.

Posterior distribution of time constant in the presence of uncertain inclusion diameter is shown in Fig. 5.11. The value of the diameter is modeled as a normal distribution with both unbiased and biased mean values as well as large and small standard deviations. The same BAFEM inverse procedure is applied to estimation the posterior distribution of the time constant. For both inclusions, the Bayesian approach with the SDF model gives very poor estimation, and the estimated mean values are highly biased from the true value. For BAFEM, even though the diameter is not accurately known, the estimated posterior distribution is around the true value of the time constant, which highly improved the accuracy of the inverse solution. In addition, in each case, the distribution of the diameter does not change the posterior distribution much, which means that the uncertainty is mainly contributed by the measurement noise. It also means that the bias set for the diameter is acceptable in practice, which will not affect the posterior prediction significantly.

The above results demonstrate the feasibility of the proposed BAFEM to improve the quantitative estimation in the presence of local heterogeneity. However, practical application of the proposed method in heterogeneous case is still subjected to several limitations and challenges. First, the inclusion itself may not be homogeneous for soft tissue. Second, the inclusion and the background may not be fully bonded (especially for benign inclusions), which means certain contact condition should be defined. [115] Finally, the heterogeneous structure will increase the uncertainty of prior estimation on ARF distribution due to the unknown properties inside the inclusion. [60]

5.5 Summary

An inverse finite element characterization procedure based on a Bayesian approach is applied to calculate the time constant in ARF induced creep imaging. It aims to improve the estimation accuracy when the SDF models have poor performance. The Bayesian approach with FE model (BAFEM) procedure provides a predicted distribution of the time constant in the present of displacement jitter, code uncertainty, and model parameter uncertainty. The major improvement of the proposed procedure is that it can make the best use of prior information on the ARF imaging system and soft tissues, which are discarded in the SDF models. By an integration of the uncertain prior information, prediction of BAFEM is more comprehensive and accurate than that of methods based on the SDF models for this problem. By GP metamodeling of the FE models, a MCMC procedure is made computationally feasible and efficient in Bayesian parameter estimation, and the associated code uncertainty is integrated in the calculation. It provides a potential to improve the ROE-response-based methods where the unknown stress limits an accurate characterization with FE methods.

Chapter 6: Conclusions and Future Work

6.1 Conclusions

This thesis provides an extensive analysis on both the forward problem and inverse problem in acoustic radiation force imaging of soft tissue within the ROE. In the forward problem, the finite element method is employed to study the dynamic behavior of soft tissue within the ROE, which investigates the assumptions that are made in ARF imaging within the ROE and analyze the factors that affect the accuracy of these assumptions. This thesis also suggests that these assumptions may lead to large estimation error in certain cases and an inverse FE analysis procedure is necessary to improve the imaging quality. In the inverse problem, an inverse FE characterization procedure based on a Bayesian approach is presented. By an integration of the uncertain prior information into FE model, numerical simulation results demonstrate that the Bayesian approach with FE model provides an efficient and practical estimation of the probability distributions of the mechanical property of soft tissue. The detailed conclusions are presented in the following subsections.

6.1.1 Forward Dynamic Simulation with FE models

As is discussed in Section 2.3, the unknown stress distribution within the ROE limits the accurate characterization with the ROE responses in ARF imaging, and assumptions have been made for both qualitative and quantitative imaging within the ROE. The forward

dynamic simulation aims to study these assumptions and decide what factors will affect the accuracy of these assumptions.

In the case of qualitative imaging, the effects of global boundary conditions on ROE responses are investigated via harmonic motion imaging (HMI). It is observed that the dynamic response of soft tissue with high viscosity is independent of the global boundary conditions for regions remote to the boundary; thus it can be subjected to local analysis to estimate the underlying mechanical properties. However, the dynamic response is sensitive to global boundary conditions for tissue with low viscosity or regions located near to the boundary. In a heterogeneous medium, the contrast transfer efficiency (CTE) of HMI is studied to evaluate the homogeneous assumption. The results illustrated that as the true inclusion-to-background contrast increases (i.e., the heterogeneity of the model increases), the observed contrast that is based on the measured displacement amplitude decreases.

In the case of quantitative imaging, the simplified single degree-of-freedom (SDF) model is evaluated for both homogeneous and heterogeneous cases. This theis investigates the fundamental limitations of the commonly used SDF and homogeneous assumptions in ARF induced creep imaging. Finite element models are developed to simulate the dynamic behavior of viscoelastic soft tissue subjected to step ARF. The results indicate that the SDF model can provide good estimations for homogeneous soft tissue with high viscosity, but exhibits poor performance for low viscosity soft tissue. In addition, a smaller focal region of the ARF is desirable to reduce the estimation error with the SDF models. For heterogeneous media, the ROE responses are highly affected

by the local heterogeneity, which results in deterioration of the effectiveness of the SDF and homogeneous simplifications.

6.1.2 Inverse FE Characterization based on A Bayesian Approach

The purpose of the inverse FE characterization is to improve the quantitative imaging within the ROE. The integration of Bayesian approach with the FE model solves a statistical inverse problem in ARF induced creep imaging, which estimates a viscoelasticity metric, time constant. Gaussian process metamodeling is applied to provide a fast statistical approximation based on a small number of computationally expensive FE-model runs, which makes the Bayesian estimation procedure computationally feasible.

The inverse FE characterization procedure can take full advantage of the prior information of model parameters and consider all the associated uncertainties, which make a more practical and comprehensive description of the estimation in the presence of measurement noise and model parameter uncertainty. In a comparison study with the simplified quantitative models, the Bayesian approach with FE model improves the estimation results even in the presence of large uncertainty levels of the model parameters. With reasonable prior information in ARF induced creep imaging, the estimated mean values of the time constant are generally unbiased or near unbiased, in contrast to the simplified SDF model which can lead to large estimated error as is discussed in Section 3.4. In addition, in this method, the estimation can further be improved if more accurate displacement data and prior model parameter information are available. However, for the simplified SDF model, even accurate prior model parameter

information is available; the estimated parameter is still highly biased due to the limitation of the SDF model that cannot integrate all the uncertain prior information into the estimation.

6.2 Novel Contributions

This thesis investigates the commonly used assumptions in ARF imaging within the ROE by exploring the dynamic behavior of soft tissue and analyzing the factors that affect the accuracy of these assumptions. This study demonstrates both the advantageous conditions and limitations of these assumptions, which points out when a more accurate inverse procedure is necessary to characterize the mechanical properties of soft tissue.

Instead of solving the inverse problem with best-fit values from an optimization procedure, this thesis proposes to formulate a statistical inverse problem to take full advantages of prior information to improve the quantitative imaging in the ROE where the unknown stress distribution limits an accurate estimation, which is a new perspective to formulate the inverse problem in the field of ARF imaging within the ROE. The Bayesian approach with the FE model highly improves the characterization accuracy in the presence of large uncertainty levels of the model parameters. This new perspective demonstrates how to integrate uncertain prior information with FE method efficiently to improve the estimation accuracy, which can be extended to other ROE-response-based imaging method where the uncertain prior information limits an elaborate modeling and characterization of soft tissue.

6.3 Future Work

For the inverse FE characterization part, this thesis mainly focuses on the estimation of time constant in ARF induced creep imaging. In future work, other ROE-response-based methods may implement the same inverse procedure to improve the estimation. In particular, if this method can be combined with the Time-to-Peak (TTP) method that is introduced in Chapter 2, then both the elasticity and viscosity of soft tissue can be characterized with a full ROE-response-based method.

For soft tissue with heterogeneity, models with more complex heterogeneous structure may be considered in future work, in which cases it is more challenging to obtain the necessary prior information to build the FE model. The advantage of the proposed method is the flexibility to integrate more uncertain prior information. As the model changes, additional uncertainty due to new model parameters can be easily added to the inverse procedure without increasing the computational cost significantly.

For computational efficiency, this problem can be parallel computed for both the training of the Gaussian process metamodel and the MCMC sampling for Bayesian inference. In future work, this method may be implemented with parallel computing. This will also allow more design points to be used to train the Gaussian process metamodel, which will reduce the uncertainty due to metamodeling.

Appendix: Abbreviations

ARF	Acoustic Radiation Force
ARFI	Acoustic Radiation Force Impulse
BAFEM	Bayesian Approach with Finite Element Model
CFE	Characterization Finite Element
CTE	Contrast-Transfer Efficiency
DSDA	Direct-solution Steady-state Dynamic Analysis
FE	Finite Element
GP	Gaussian Process
HIFU	High Intensity Focused Ultrasound
HMI	Harmonic Motion Imaging
MCMC	Markov Chain Monte Carlo
LGQ	Legendre-Gauss Quadrature
LHS	Latin Hypercube Sampling
LSM	Least Square Method
REE	Relative Estimation Error
ROE	Region of Excitation
SD	Standard Deviation
SDF	Single Degree-of-Freedom
SFE	Synthetic Finite Element
SNR	Signal-to-Noise Ratio
TTP	Time-to-Peak

References

[1] Sugimoto, T., Ueha, S., and Itoh, K., 1990, "Tissue hardness measurement using the radiation force of focused ultrasound," Ultrasonics Symposium, 1990. Proceedings., IEEE 1990, pp. 1377–1380 vol.3.

[2] Ophir, J., Céspedes, I., Ponnekanti, H., Yazdi, Y., and Li, X., 1991, "Elastography: a quantitative method for imaging the elasticity of biological tissues," Ultrason. Imaging, **13**(2), pp. 111–134.

[3] Fatemi, M., and Greenleaf, J. F., 2002, "Imaging the Viscoelastic Properties of Tissue," Imaging of Complex Media with Acoustic and Seismic Waves, P.M. Fink, P.W.A. Kuperman, P.J.-P. Montagner, and P.A. Tourin, eds., Springer Berlin Heidelberg, pp. 257–276.

[4] Greenleaf, J. F., Fatemi, M., and Insana, M., 2003, "Selected Methods for Imaging Elastic Properties of Biological Tissues," Annu. Rev. Biomed. Eng., **5**(1), pp. 57–78.

[5] Maleke, C., Pernot, M., and Konofagou, E. E., 2006, "Single-element focused ultrasound transducer method for harmonic motion imaging," Ultrason. Imaging, **28**(3), pp. 144–158.

[6] Wells, P. N. T., and Liang, H.-D., 2011, "Medical ultrasound: imaging of soft tissue strain and elasticity," J. R. Soc. Interface R. Soc., **8**(64), pp. 1521–1549.

[7] Krouskop, T. A., Dougherty, D. R., and Vinson, F. S., 1987, "A pulsed Doppler ultrasonic system for making noninvasive measurements of the mechanical properties of soft tissue," J. Rehabil. Res. Dev., **24**(2), pp. 1–8.

[8] Nightingale, K., 2011, "Acoustic Radiation Force Impulse (ARFI) Imaging: a Review," Curr. Med. Imaging Rev., **7**(4), pp. 328–339.

[9] Parker, K. J., Doyley, M. M., and Rubens, D. J., 2011, "Imaging the elastic properties of tissue: the 20 year perspective," Phys. Med. Biol., **56**(1), pp. R1–R29.

[10] Lerner, R. M., Parker, K. J., Holen, J., Gramiak, R., and Waag, R. C., 1988, "Sono-Elasticity: Medical Elasticity Images Derived from Ultrasound Signals in Mechanically Vibrated Targets," Acoustical Imaging, L.W. Kessler, ed., Springer US, pp. 317–327.

[11] Doyley, M. M., Van Houten, E. E., Weaver, J. B., Poplack, S., Duncan, L., Kennedy, F., and Paulsen, K. D., 2004, "Shear modulus estimation using parallelized partial volumetric reconstruction," IEEE Trans. Med. Imaging, **23**(11), pp. 1404–1416.

[12] Oberai, A. A., Gokhale, N. H., and Feijóo, G. R., 2003, "Solution of inverse problems in elasticity imaging using the adjoint method," Inverse Probl., **19**(2), p. 297.

[13] Kim, J., and Srinivasan, M. A., 2005, "Characterization of Viscoelastic Soft Tissue Properties from In Vivo Animal Experiments and Inverse FE Parameter Estimation," Medical Image Computing and Computer-Assisted Intervention – MICCAI 2005, J.S. Duncan, and G. Gerig, eds., Springer Berlin Heidelberg, pp. 599–606.

[14] Eskandari, H., Salcudean, S. E., Rohling, R., and Ohayon, J., 2008, "Viscoelastic characterization of soft tissue from dynamic finite element models," Phys. Med. Biol., **53**(22), pp. 6569–6590.

[15] Seshaiyer, P., and Humphrey, J. D., 2003, "A sub-domain inverse finite element characterization of hyperelastic membranes including soft tissues," J. Biomech. Eng., **125**(3), pp. 363–371.
[16] Shan, B., Pelegri, A. A., Maleke, C., and Konofagou, E. E., 2008, "A mechanical model to compute elastic modulus of tissues for harmonic motion imaging," J. Biomech., **41**(10), pp. 2150–2158.
[17] Barbone, P. E., and Bamber, J. C., 2002, "Quantitative elasticity imaging: what can and cannot be inferred from strain images," Phys. Med. Biol., **47**(12), pp. 2147–2164.
[18] Callé, S., Remenieras, J.-P., Matar, O. B., Hachemi, M. E., and Patat, F., 2005, "Temporal analysis of tissue displacement induced by a transient ultrasound radiation force," J. Acoust. Soc. Am., **118**(5), pp. 2829–2840.
[19] Palmeri, M. L., and Nightingale, K. R., 2011, "What challenges must be overcome before ultrasound elasticity imaging is ready for the clinic?," Imaging Med., **3**(4), pp. 433–444.
[20] Sarvazyan, A. P., Rudenko, O. V., Swanson, S. D., Fowlkes, J. B., and Emelianov, S. Y., 1998, "Shear wave elasticity imaging: a new ultrasonic technology of medical diagnostics," Ultrasound Med. Biol., **24**(9), pp. 1419–1435.
[21] Walker, W. F., Fernandez, F. J., and Negron, L. A., 2000, "A method of imaging viscoelastic parameters with acoustic radiation force," Phys. Med. Biol., **45**(6), p. 1437.
[22] Nightingale, K., Soo, M. S., Nightingale, R., and Trahey, G., 2002, "Acoustic radiation force impulse imaging: in vivo demonstration of clinical feasibility," Ultrasound Med. Biol., **28**(2), pp. 227–235.
[23] Konofagou, E. E., and Hynynen, K., 2003, "Localized harmonic motion imaging: theory, simulations and experiments," Ultrasound Med. Biol., **29**(10), pp. 1405–1413.
[24] Bower, A. F., 2011, Applied Mechanics of Solids, CRC Press.
[25] Liu, D., and Ebbini, E. S., 2008, "Viscoelastic Property Measurement in Thin Tissue Constructs Using Ultrasound," IEEE Trans. Ultrason. Ferroelectr. Freq. Control, **55**(2), pp. 368–383.
[26] Vappou, J., Maleke, C., and Konofagou, E. E., 2009, "Quantitative viscoelastic parameters measured by harmonic motion imaging," Phys. Med. Biol., **54**(11), pp. 3579–3594.
[27] Palmeri, M. L., and Nightingale, K. R., 2011, "Acoustic radiation force-based elasticity imaging methods," Interface Focus, p. rsfs20110023.
[28] Karpiouk, A. B., Aglyamov, S. R., Ilinskii, Y. A., Zabolotskaya, E. A., and Emelianov, S. Y., 2009, "Assessment of Shear Modulus of Tissue Using Ultrasound Radiation Force Acting on a Spherical Acoustic Inhomogeneity," IEEE Trans. Ultrason. Ferroelectr. Freq. Control, **56**(11), pp. 2380–2387.
[29] Zhao, X., and Pelegri, A. A., 2014, "Dynamic Simulation of Viscoelastic Soft Tissue in Acoustic Radiation Force Creep Imaging," J. Biomech. Eng., **136**(9), p. 094502.
[30] Achenbach, J. D., 1975, Wave Propagation in Elastic Solids, North-Holland Publishing Company.

[31] Bercoff, J., Tanter, M., and Fink, M., 2004, "Supersonic shear imaging: a new technique for soft tissue elasticity mapping," IEEE Trans. Ultrason. Ferroelectr. Freq. Control, **51**(4), pp. 396–409.

[32] Doyley, M. M., 2012, "Model-based elastography: a survey of approaches to the inverse elasticity problem," Phys. Med. Biol., **57**(3), pp. R35–73.

[33] Nightingale, K., McAleavey, S., and Trahey, G., 2003, "Shear-wave generation using acoustic radiation force: in vivo and ex vivo results," Ultrasound Med. Biol., **29**(12), pp. 1715–1723.

[34] Nightingale, K. R., Zhai, L., Dahl, J. J., Frinkley, K. D., and Palmeri, M. L., 2006, "4K-5 Shear Wave Velocity Estimation Using Acoustic Radiation Force Impulsive Excitation in Liver In Vivo," IEEE Ultrasonics Symposium, 2006, pp. 1156–1160.

[35] Palmeri, M. L., Wang, M. H., Dahl, J. J., Frinkley, K. D., and Nightingale, K. R., 2008, "Quantifying hepatic shear modulus in vivo using acoustic radiation force," Ultrasound Med. Biol., **34**(4), pp. 546–558.

[36] Mauldin, F. W., Haider, M. A., Loboa, E. G., Behler, R. H., Euliss, L. E., Pfeiler, T. W., and Gallippi, C. M., 2008, "Monitored steady-state excitation and recovery (MSSER) radiation force imaging using viscoelastic models," IEEE Trans. Ultrason. Ferroelectr. Freq. Control, **55**(7), pp. 1597–1610.

[37] Nightingale, K. R., Rouze, N. C., Wang, M. H., Zhai, L., and Palmeri, M. L., 2011, "Comparison of qualitative and quantitative acoustic radiation force based elasticity imaging methods," 2011 IEEE International Symposium on Biomedical Imaging: From Nano to Macro, pp. 1606–1609.

[38] Chen, S., Fatemi, M., and Greenleaf, J. F., 2004, "Quantifying elasticity and viscosity from measurement of shear wave speed dispersion," J. Acoust. Soc. Am., **115**(6), pp. 2781–2785.

[39] Zheng, Y., Chen, S., Tan, W., Kinnick, R., and Greenleaf, J. F., 2007, "Detection of tissue harmonic motion induced by ultrasonic radiation force using pulse-echo ultrasound and Kalman filter," IEEE Trans. Ultrason. Ferroelectr. Freq. Control, **54**(2), pp. 290–300.

[40] Chen, S., Urban, M. W., Pislaru, C., Kinnick, R., Zheng, Y., Yao, A., and Greenleaf, J. F., 2009, "Shearwave dispersion ultrasound vibrometry (SDUV) for measuring tissue elasticity and viscosity," IEEE Trans. Ultrason. Ferroelectr. Freq. Control, **56**(1), pp. 55–62.

[41] Zhao, H., Urban, M., Greenleaf, J., and Chen, S., 2010, "Elasticity and viscosity estimation from shear wave velocity and attenuation: A simulation study," 2010 IEEE Ultrasonics Symposium (IUS), pp. 1604–1607.

[42] McAleavey, S. A., Menon, M., and Orszulak, J., 2007, "Shear-Modulus Estimation by Application of Spatially-Modulated Impulsive Acoustic Radiation Force," Ultrason. Imaging, **29**(2), pp. 87–104.

[43] Palmeri, M. L., Xu, D., Zhai, L., and Nightingale, K. R., 2008, "Acoustic radiation force based quantification of tissue shear modulus within the region of excitation," IEEE Ultrasonics Symposium, 2008. IUS 2008, pp. 2009–2012.

[44] Palmeri, M. L., McAleavey, S. A., Fong, K. L., Trahey, G. E., and Nightingale, K. R., 2006, "Dynamic mechanical response of elastic spherical inclusions to impulsive

acoustic radiation force excitation," IEEE Trans. Ultrason. Ferroelectr. Freq. Control, **53**(11), pp. 2065–2079.

[45] Palmeri, M. L., Sharma, A. C., Bouchard, R. R., Nightingale, R. W., and Nightingale, K. R., 2005, "A Finite-Element Method Model of Soft Tissue Response to Impulsive Acoustic Radiation Force," IEEE Trans. Ultrason. Ferroelectr. Freq. Control, **52**(10), p. 1699.

[46] Trahey, G. E., Palmeri, M. L., Bentley, R. C., and Nightingale, K. R., 2004, "Acoustic radiation force impulse imaging of the mechanical properties of arteries: in vivo and ex vivo results," Ultrasound Med. Biol., **30**(9), pp. 1163–1171.

[47] Fahey, B. J., Nelson, R. C., Bradway, D. P., Hsu, S. J., Dumont, D. M., and Trahey, G. E., 2008, "In vivo visualization of abdominal malignancies with acoustic radiation force elastography," Phys. Med. Biol., **53**(1), pp. 279–293.

[48] Behler, R. H., Nichols, T. C., Zhu, H., Merricks, E. P., and Gallippi, C. M., 2009, "ARFI imaging for noninvasive material characterization of atherosclerosis. Part II: toward in vivo characterization," Ultrasound Med. Biol., **35**(2), pp. 278–295.

[49] Eyerly, S. A., Hsu, S. J., Agashe, S. H., Trahey, G. E., Li, Y., and Wolf, P. D., 2010, "An in vitro assessment of acoustic radiation force impulse imaging for visualizing cardiac radiofrequency ablation lesions," J. Cardiovasc. Electrophysiol., **21**(5), pp. 557–563.

[50] Hou, G. Y., Luo, J., Marquet, F., Maleke, C., Vappou, J., and Konofagou, E. E., 2011, "Performance assessment of HIFU lesion detection by harmonic motion imaging for focused ultrasound (HMIFU): a 3-D finite-element-based framework with experimental validation," Ultrasound Med. Biol., **37**(12), pp. 2013–2027.

[51] Konofagou, E. E., Maleke, C., and Vappou, J., 2012, "Harmonic Motion Imaging (HMI) for Tumor Imaging and Treatment Monitoring," Curr. Med. Imaging Rev., **8**(1), pp. 16–26.

[52] Foster, F. S., and Hunt, J. W., 1979, "Transmission of ultrasound beams through human tissue--focusing and attenuation studies," Ultrasound Med. Biol., **5**(3), pp. 257–268.

[53] Guzina, B. B., Tuleubekov, K., Liu, D., and Ebbini, E. S., 2009, "Viscoelastic characterization of thin tissues using acoustic radiation force and model-based inversion," Phys. Med. Biol., **54**(13), pp. 4089–4112.

[54] Wang, M. H., Palmeri, M. L., Rouze, N. C., Xu, D., and Nightingale, K. R., 2010, "Improving precision of tissue shear modulus quantification within the region of acoustic radiation force excitation with compounded displacement estimates," 2010 IEEE Ultrasonics Symposium (IUS), pp. 1600–1603.

[55] Viola, F., and Walker, W. F., 2003, "Radiation force imaging of viscoelastic properties with reduced artifacts," IEEE Trans. Ultrason. Ferroelectr. Freq. Control, **50**(6), pp. 736–742.

[56] Amador, C., Urban, M. W., Chen, S., and Greenleaf, J. F., 2012, "Loss tangent and complex modulus estimated by acoustic radiation force creep and shear wave dispersion," Phys. Med. Biol., **57**(5), pp. 1263–1282.

[57] Scola, M. R., Baggesen, L. M., and Gallippi, C. M., 2012, "Multi-Push (MP) Acoustic Radiation Force (ARF) Ultrasound for Assessing Tissue Viscoelasticity, In

Vivo*," Conf. Proc. Annu. Int. Conf. IEEE Eng. Med. Biol. Soc. IEEE Eng. Med. Biol. Soc. Conf., **2012**, pp. 2323–2326.

[58] Shan, B., Kogit, M. L., and Pelegri, A. A., 2008, "Dynamic simulation of viscoelastic soft tissues in harmonic motion imaging application," J. Biomech., **41**(14), pp. 3031–3037.

[59] Iorga, L. N., Shan, B., and Pelegri, A. A., 2009, "Finite element dynamic analysis of soft tissues using state-space model," Comput. Methods Biomech. Biomed. Engin., **12**(2), pp. 197–209.

[60] Nightingale, K. R., Nightingale, R. W., Palmeri, M. L., and Trahey, G. E., 2000, "A finite element model of remote palpation of breast lesions using radiation force: factors affecting tissue displacement," Ultrason. Imaging, **22**(1), pp. 35–54.

[61] Maleke, C., Luo, J., Gamarnik, V., Lu, X. L., and Konofagou, E. E., 2010, "Simulation study of amplitude-modulated (AM) harmonic motion imaging (HMI) for stiffness contrast quantification with experimental validation," Ultrason. Imaging, **32**(3), pp. 154–176.

[62] Lee, K. H., Szajewski, B. A., Hah, Z., Parker, K. J., and Maniatty, A. M., 2012, "Modeling shear waves through a viscoelastic medium induced by acoustic radiation force," Int. J. Numer. Methods Biomed. Eng., **28**(6-7), pp. 678–696.

[63] Dill, E. H., 2011, The Finite Element Method for Mechanics of Solids with ANSYS Applications, CRC Press.

[64] Gefen, A., and Dilmoney, B., 2007, "Mechanics of the normal woman's breast," Technol. Health Care Off. J. Eur. Soc. Eng. Med., **15**(4), pp. 259–271.

[65] Dahl, J. J., Pinton, G. F., Mark, L., Agrawal, V., Nightingale, K. R., and Trahey, G. E., 2007, "A Parallel Tracking Method for Acoustic Radiation Force Impulse Imaging," IEEE Trans. Ultrason. Ferroelectr. Freq. Control, **54**(2), pp. 301–312.

[66] Konofagou, E., Thierman, J., and Hynynen, K., 2001, "A focused ultrasound method for simultaneous diagnostic and therapeutic applications--a simulation study," Phys. Med. Biol., **46**(11), pp. 2967–2984.

[67] Catheline, S., Gennisson, J.-L., Delon, G., Fink, M., Sinkus, R., Abouelkaram, S., and Culioli, J., 2004, "Measurement of viscoelastic properties of homogeneous soft solid using transient elastography: An inverse problem approach," J. Acoust. Soc. Am., **116**(6), pp. 3734–3741.

[68] Qiang, B., Greenleaf, J., and Zhang, X., 2010, "Quantifying viscoelasticity of gelatin phantoms by measuring impulse response using compact optical sensors," IEEE Trans. Ultrason. Ferroelectr. Freq. Control, **57**(7), pp. 1696–1700.

[69] Mohr, M., Abrams, E., Engel, C., Long, W. B., and Bottlang, M., 2007, "Geometry of human ribs pertinent to orthopedic chest-wall reconstruction," J. Biomech., **40**(6), pp. 1310–1317.

[70] 2013, Abaqus Documentation, Dassault Systèmes, Waltham, MA, USA.

[71] Maleke, C., Pernot, M., and Konofagou, E., 2006, "Real-Time Monitoring Of Regional Tissue Elasticity During FUS Focused Ultrasound Therapy Using Harmonic Motion Imaging," pp. 171–175.

[72] Frigge, M., Hoaglin, D. C., and Iglewicz, B., 1989, "Some Implementations of the Boxplot," Am. Stat., **43**(1), pp. 50–54.

[73] Ponnekanti, H., Ophir, J., Huang, Y., and Céspedes, I., 1995, "Fundamental mechanical limitations on the visualization of elasticity contrast in elastography," Ultrasound Med. Biol., **21**(4), pp. 533–543.

[74] Kallel, F., Bertrand, M., and Ophir, J., 1996, "Fundamental limitations on the contrast-transfer efficiency in elastography: an analytic study," Ultrasound Med. Biol., **22**(4), pp. 463–470.

[75] Fung, Y., 1981, Biomechanics: mechanical properties of living tissues, Springer-Verlag.

[76] Walker, W. F., 1999, "Internal deformation of a uniform elastic solid by acoustic radiation force," J. Acoust. Soc. Am., **105**(4), pp. 2508–2518.

[77] Skovoroda, A. R., and Sarvazyan, A. P., 1999, "Determination of viscoelastic shear characteristics of a medium from its response to focused ultrasonic loading," Biophysics, **44**(2), pp. 325–329.

[78] Urban, M. W., Chen, S., and Greenleaf, J. F., 2008, "Harmonic Motion Detection in a Vibrating Scattering Medium," IEEE Trans. Ultrason. Ferroelectr. Freq. Control, **55**(9), pp. 1956–1974.

[79] Sarvazyan, A. P., Skovoroda, A. R., Emelianov, S. Y., Fowlkes, J. B., Pipe, J. G., Adler, R. S., Buxton, R. B., and Carson, P. L., 1995, "Biophysical Bases of Elasticity Imaging," Acoustical Imaging, P.J.P. Jones, ed., Springer US, pp. 223–240.

[80] Nelder, J. A., and Mead, R., 1965, "A Simplex Method for Function Minimization," Comput. J., **7**(4), pp. 308–313.

[81] Nightingale, K., Palmeri, M., and Trahey, G., 2006, "Analysis of contrast in images generated with transient acoustic radiation force," Ultrasound Med. Biol., **32**(1), pp. 61–72.

[82] Jensen, J. A., and Svendsen, N. B., 1992, "Calculation of pressure fields from arbitrarily shaped, apodized, and excited ultrasound transducers," IEEE Trans. Ultrason. Ferroelectr. Freq. Control, **39**(2), pp. 262–267.

[83] Kelly, J. F., and McGough, R. J., 2006, "A time-space decomposition method for calculating the nearfield pressure generated by a pulsed circular piston," IEEE Trans. Ultrason. Ferroelectr. Freq. Control, **53**(6), pp. 1150–1159.

[84] Eppstein, M. J., Dougherty, D. E., Hawrysz, D. J., and Sevick-Muraca, E. M., 2001, "Three-dimensional Bayesian optical image reconstruction with domain decomposition," IEEE Trans. Med. Imaging, **20**(3), pp. 147–163.

[85] Milstein, A. B., Stott, J. J., Oh, S., Boas, D. A., Millane, R. P., Bouman, C. A., and Webb, K. J., 2004, "Fluorescence optical diffusion tomography using multiple-frequency data," J. Opt. Soc. Am. A, **21**(6), p. 1035.

[86] Corso, J. J., Sharon, E., Dube, S., El-Saden, S., Sinha, U., and Yuille, A., 2008, "Efficient Multilevel Brain Tumor Segmentation With Integrated Bayesian Model Classification," IEEE Trans. Med. Imaging, **27**(5), pp. 629–640.

[87] Fouda, A. E., and Teixeira, F. L., 2014, "Ultra-wideband microwave imaging of breast cancer tumors via Bayesian inverse scattering," J. Appl. Phys., **115**(6), p. 064701.

[88] Oakley, J., and O'Hagan, A., 2002, "Bayesian inference for the uncertainty distribution of computer model outputs," Biometrika, **89**(4), pp. 769–784.

[89] Kennedy, M. C., and O'Hagan, A., 2001, "Bayesian calibration of computer models," J. R. Stat. Soc. Ser. B Stat. Methodol., **63**(3), pp. 425–464.
[90] Jin, R., Chen, W., and Simpson, T. W., 2001, "Comparative studies of metamodelling techniques under multiple modelling criteria," Struct. Multidiscip. Optim., **23**(1), pp. 1–13.
[91] Fricker, T. E., Oakley, J. E., Sims, N. D., and Worden, K., 2011, "Probabilistic uncertainty analysis of an FRF of a structure using a Gaussian process emulator," Mech. Syst. Signal Process., **25**(8), pp. 2962–2975.
[92] DiazDelaO, F. A., and Adhikari, S., 2011, "Gaussian process emulators for the stochastic finite element method," Int. J. Numer. Methods Eng., **87**(6), pp. 521–540.
[93] Arendt, P. D., Apley, D. W., and Chen, W., 2012, "Quantification of Model Uncertainty: Calibration, Model Discrepancy, and Identifiability," J. Mech. Des., **134**(10), pp. 100908–100908.
[94] Zhao, X., and Pelegri, A. A., 2015, "A Bayesian approach for characterization of soft tissue viscoelasticity in acoustic radiation force imaging," Int. J. Numer. Methods Biomed. Eng., p. n/a–n/a.
[95] Duda, R. O., Hart, P. E., and Stork, D. G., 2000, Pattern Classification (2Nd Edition), Wiley-Interscience.
[96] Qui ñonero-candela, J., Ramussen, C. E., and Williams, C. K. I., 2007, Approximation Methods for Gaussian Process Regression.
[97] Mchutchon, A., and Rasmussen, C. E., 2011, "Gaussian Process Training with Input Noise," Advances in Neural Information Processing Systems 24, J. Shawe-Taylor, R.S. Zemel, P.L. Bartlett, F. Pereira, and K.Q. Weinberger, eds., Curran Associates, Inc., pp. 1341–1349.
[98] Girard, A., Candela, J. Q., Murray-smith, R., and Rasmussen, C. E., 2003, Gaussian Process Priors with Uncertain Inputs - Application to Multiple-Step Ahead Time Series Forecasting.
[99] Rasmussen, C. E., and Williams, C. K. I., 2005, Gaussian Processes for Machine Learning (Adaptive Computation and Machine Learning), The MIT Press.
[100] Higdon, D., Gattiker, J., Williams, B., and Rightley, M., 2008, "Computer Model Calibration Using High-Dimensional Output," J. Am. Stat. Assoc., **103**(482), pp. 570–583.
[101] Gamerman, D., and Lopes, H. F., 2006, Markov Chain Monte Carlo: Stochastic Simulation for Bayesian Inference, Second Edition, CRC Press.
[102] Titsias, M. K., Rattray, M., and Lawrence, N. D., 2011, "Markov chain Monte Carlo algorithms for Gaussian processes," Bayesian Time Series Models, Cambridge University Press.
[103] Hastings, W. K., 1970, "Monte Carlo sampling methods using Markov chains and their applications," Biometrika, **57**(1), pp. 97–109.
[104] Andrieu, C., Freitas, N. de, Doucet, A., and Jordan, M. I., 2003, "An Introduction to MCMC for," Mach. Learn., **50**(1-2), pp. 5–43.
[105] Byrd, J. M. R., Jarvis, S. A., and Bhalerao, A. H., 2008, "Reducing the run-time of MCMC programs by multithreading on SMP architectures," IEEE International Symposium on Parallel and Distributed Processing, 2008. IPDPS 2008, pp. 1–8.

[106] Chen, S., Sanchez, W., Callstrom, M. R., Gorman, B., Lewis, J. T., Sanderson, S. O., Greenleaf, J. F., Xie, H., Shi, Y., Pashley, M., Shamdasani, V., Lachman, M., and Metz, S., 2013, "Assessment of liver viscoelasticity by using shear waves induced by ultrasound radiation force," Radiology, **266**(3), pp. 964–970.

[107] McAleavey, S. A., Nightingale, K. R., and Trahey, G. E., 2003, "Estimates of echo correlation and measurement bias in acoustic radiation force impulse imaging," IEEE Trans. Ultrason. Ferroelectr. Freq. Control, **50**(6), pp. 631–641.

[108] Zhang, Y., Hall, L. O., Goldgof, D. B., and Sarkar, S., 2006, "A constrained genetic approach for computing material property of elastic objects," IEEE Trans. Evol. Comput., **10**(3), pp. 341–357.

[109] Palmeri, M. L., McAleavey, S. A., Trahey, G. E., and Nightingale, K. R., 2006, "Ultrasonic Tracking of Acoustic Radiation Force-Induced Displacements in Homogeneous Media," IEEE Trans. Ultrason. Ferroelectr. Freq. Control, **53**(7), pp. 1300–1313.

[110] Doherty, J. R., Trahey, G. E., Nightingale, K. R., and Palmeri, M. L., 2013, "Acoustic radiation force elasticity imaging in diagnostic ultrasound," IEEE Trans. Ultrason. Ferroelectr. Freq. Control, **60**(4), pp. 685–701.

[111] Zhao, X., and Pelegri, A. A., 2014, "Modelling of global boundary effects on harmonic motion imaging of soft tissues," Comput. Methods Biomech. Biomed. Engin., **17**(9), pp. 1021–1031.

[112] McKay, M. D., Beckman, R. J., and Conover, W. J., 1979, "A Comparison of Three Methods for Selecting Values of Input Variables in the Analysis of Output from a Computer Code," Technometrics, **21**(2), pp. 239–245.

[113] Iman, R. L., and Helton, J. C., 1988, "An Investigation of Uncertainty and Sensitivity Analysis Techniques for Computer Models," Risk Anal., **8**(1), pp. 71–90.

[114] Silverman, B. W., 1986, Density Estimation for Statistics and Data Analysis, CRC Press.

[115] Konofagou, E. E., Harrigan, T., and Ophir, J., 2000, "Shear strain estimation and lesion mobility assessment in elastography," Ultrasonics, **38**(1-8), pp. 400–404.

[116] Bilgen, M., and Insana, M. F., 1998, "Elastostatics of a spherical inclusion in homogeneous biological media," Phys. Med. Biol., **43**(1), p. 1.

[117] Kauer, M., Vuskovic, V., Dual, J., Szekely, G., and Bajka, M., 2002, "Inverse finite element characterization of soft tissues," Med. Image Anal., **6**(3), pp. 275–287.